Investigations on mixed valent manganites

THESIS

Submitted to

Saurashtra University, Rajkot, India

For the Degree of

Doctor of Philosophy

in Science

in the subject of Physics

By

Prashant Shantilal Vachhani

Under the supervision of

Dr. D. G. Kuberkar
Professor
Department of Physics
Saurashtra University
Rajkot, India

July 2008

STATEMENT UNDER O. Ph.D. 7 OF THE SAURASHTRA UNIVERSITY

*This is certified that the work presented in the thesis is my own work, carried out under the supervision of **Dr. D. G. Kuberkar** and leads to some important contributions in Physics supported by necessary references.*

Prashant S. Vachhani
(Research Scholar)

*This is to certify that the work submitted for Ph.D. degree in Physics to Saurashtra University, Rajkot by **Mr. Prashant S. Vachhani** has been the result of more than three years of work under my supervision and is a good contribution in the field of Solid State Physics and Materials Science.*

Dr. D. G. Kuberkar
(Research Guide)
Professor
Department of Physics
Saurashtra University
Rajkot

This thesis is dedicated to

My beloved Parents and Family

Acknowledgements

"It is always better to take a spontaneous decision rather to think about it & the secret of success always lies in the implementation of that decision"

First of all, I wish to thank my Ph.D. supervisor Prof. Deelip G. Kuberkar, for giving me the opportunity to work under his guidance on interesting and fascinating subject of manganites and for making me to understand that, research is a privilege, which deserves passion and devotion. My intellectual debt to him goes beyond the physics, I have learned from him.

I am deeply grateful to Dr. D.M. Phase & Dr. R.J. Choudhary, UGC-DAE CSR, Indore for their precious guidance for explaining to me about the thin film deposition and related aspects of work. I fall short of words to express my gratitude to them. I also acknowledge the help extended by other colleagues, Mr. Ramprakash, Mrs. Shailja Tiwari and Mr. Manoj at Indore during the course of this work.

I am thankful to Dr. Rajeev Rawat, UGC-DAE CSR, Indore for providing continuous support to use the resistivity & MR setup in his low temperature laboratory. I also extend my heartfelt thanks to Miss. Pallavi Kushwaha, Mr. Sachin for their help in taking resistivity measurements.

I am thankful to Dr. V. Ganesan, UGC-DAE CSR, Indore for providing PPMS & AFM measurements in his Lab. I also acknowledge the help by other lab members, Miss. Swati Pandya, Miss. Deepti Jain and Mr. Mohan Gangrade.

I would like to specially thank Prof. P. Chaddah, Prof. Ajay Gupta & Dr. V.R. Reddy for their help in using HR-XRD facility at UGC-DAE CSR, Indore.

I would also like to thank Dr. L. M. Kukreja, RRCAT, Indore for his interest in my initial PLD work and encouragement. Many thanks to Dr. B.N. Singh and Mr. Pankaj Misra, RRCAT, for helping me in the thin film deposition.

I express my thanks to Dr. Ravi Kumar, IUAC, New Delhi for extending the SHI facility at IUAC, New Delhi.

I would like to thank, Dr. J. A. Bhalodia and Dr. Nikesh Shah for the moral support during this work. I express my deep sense of thankfulness to Dr. J.H. Markna for helping me in the analysis work & his elderly friendly advice during my Ph.D. work.

I thank Mr. Rajesh Desai, Mr. M.J. Meghpara and Mr. M.S. Suthar for the administrative and technical help during the course of my doctoral work.

I am thankful to the Prof. & Head of Physics Department and teaching faculty members of the department who have helped me in learning Physics.

My sincere thanks are due for senior colleagues and friends Dr. Chetan M. Thaker, Dr. R.N. Parmar for their help during the course of this work. I also thank my group friends Mr. Piyush Solanki, Ms. Rujuta Doshi, Mr. Dalsania, Mr. Dhiren Pandya, Ms. Pooja Chhelavda, Ms. Jesika Chocha for their friendly cooperation and help in this endeavor. I would like to acknowledge my new labmates Mr. Tulshi Shiyani, Mr. Ravi Mansuriya and Ms. Umaba Khachar.

It is a moment to remember my friends Mr. Vinay, Mr. Chetan, Mr. Tejas, Mr. Atul, Mr. Nilesh, for providing a friendly and relaxing environment during my stay at Rajkot.

Thanks to Mrs. Preeti D. Kuberkar and Ms. Madhura D. Kuberkar for a kind hospitality during the course of this work.

It is a great moment to remember my family for their persistent efforts for developing my educational career and personality since my childhood. My father Shri. Shantilal K. Vachhani and Mother Smt. Hansaben S. Vachhani have always supported eternally for my higher education. I am indebted to my parents for their unquestioning support and love. It is time to acknowledge my family members Miss Hemaxi, Mr. Kishan, Mrs. Kashmira.

I sincerely acknowledge all my well-wishers who directly or indirectly helped me during the course of this work.

Finally, I would like to thank my fiancée, Milan for her endless love and support.

I thankfully acknowledge Gujarat Council on Science & Technology (GUJCOST), Gandhinagar, India for providing me financial assistance as Junior Research Fellow (JRF) during Feb 2006 – October 2008 under the Major Research Project (MRP) No. GUJCOST/CE/200816/2005-2006/12122 dtd: 17/09/05 (2005) of Dr. D.G. Kuberkar.

July, 2008 **Prashant S. Vachhani**

Preface

The discovery of divalent alkali metal doped rare earth manganites has attracted the attention of researchers due to its novel properties such as insulator to metal transition and large Magnetoresistance (MR). Novel properties exhibited by manganites depends on tolerance factor, A-site cation disorder, grain boundary, external or internal pressure, ion irradiation etc. which create catch the attention of scientific community for fundamental research. Likewise, the practical applications of CMR effect in manganites demand the exhibition of significant MR in low applied magnetic fields at or around room temperature which can be possibly found in thin film and device form. These thin films and devices can be useful for technological applications such as advanced magnetic recording systems, magnetic solid state memories, field and temperature sensors and magnetic microwave devices etc. In the current research work, the studies on manganite thin films and devices suggest that, these materials have potential to make use of its in the field and temperature sensing applications as well as they also useful as elementary research point of view. Various types of structural, transport and magnetotransport experiments and analysis have been made on the thin film and devices in order to understand various mechanisms and properties. The distinctive part of this work is devoted to the thickness and carrier density dependent I-V and magneto I-V property studies of unconventional bi-layered p-n junction device, to understand the properties of such devices, like non-linear field dependent I-V characteristics, temperature dependent crossover in MR and change in diffusion voltage. Bulk pellets using solid state reaction route and thin films using CSD technique in the present work were synthesized at Department of Physics, Saurashtra University, Rajkot, India. Fabrication of thin films and devices using PLD technique have been performed in collaboration with UGC-DAE CSR, Indore and RRCAT, Indore and while irradiation of thin films have been done at IUAC, New Delhi, India.

SCOPE OF FUTUTE RESEARCH ON MANGANITES

There are several problems and issues relevant to the field and temperature sensitivity studies on manganite based thin film and devices which requires further deep consciousness of the research community. The few of them are

- The study on layer dependent modifications in field and temperature sensitivity of manganite heterostructure is needed.
- Detailed investigations on manganite based p-n junction diodes with varying thicknesses and carrier concentration of p-type manganite layer should be undertaken.
- It will be interesting to carry out the comparative study of bi-layered p-n junction device grown using different techniques such as Pulsed Laser Deposition (PLD), Chemical Solution Deposition (CSD) etc.
- There is need to understand the effect of applied field and temperature on the MR and rectifying properties of various manganite diodes grown at or around RT.
- The fabrication and characterization of trilayered FET structures using p-type manganite and n-type Nb-doped STO layers can be explored.
- The effect of variation in the growth and physical parameters of p-n junction diodes on its microstructure using AFM and MFM should yield interesting results.
- The role of interface of p-type layer and substrate should be justified using structural studies.
- The main reason behind the phenomena such as rectification, field dependent V_C, crossover of MR exhibited by bi-layered manganite p-n junction devices should be explored by carrying out detailed investigations.
- It will be also interesting to study the SHI irradiation effect on I-V and magneto I-V properties of manganite p-n junction diodes.
- The in-depth study is required to understand the increase in T_P of manganite film irradiated with particular ion dose 5×10^{11} ions/cm^2.

List of Publications in national/international Journals

1. I-V studies on $La_{0.7}(Ca/Sr)_{0.3}MnO_3$ manganite thin films grown by Chemical Solution Deposition (CSD) method

   P.S. Vachhani, R.N. Parmar, P.S. Solanki, J. Raval, J.H. Markna, N.A. Shah, J.A. Bhalodia, D.S. Rana and D.G. Kuberkar

   Solid State Physics (INDIA) **50**, 517 (2005)

2. Enhancement in TCR of $La_{0.5}Pr_{0.2}Ba_{0.3}MnO_3$ manganite thin film by swift heavy ion irradiation

   P.S. Vachhani, R.R. Doshi, R.N. Parmar, J.H. Markna, J.A. Bhalodia, Ravi kumar and D.G. Kuberkar

   Solid State Physics (INDIA) **51**, 485 (2006)

3. Investigations on the magneto I-V properties of epitaxially grown manganite based p-n junction device

   P.S. Vachhani, J.H. Markna, R.J. Choudhary, D.M. Phase, V.R. Reddy and D.G. Kuberkar

   Solid State Physics (INDIA) 52, (2007)

4. Enhancement of electronic transport and magnetoresistance of Al_2O_3-impregnated $(La_{0.5}Pr_{0.2})Sr_{0.3}MnO_3$ thin films

   J.H. Markna, **P.S. Vachhani**, R.N. Parmar, P. Misra, B.N. Singh, L.M. Kukreja, D.S. Rana, S.K. Malik and D.G. Kuberkar

   Euro. Phys. Lett. **79**, 17005 (2007)

5. Strain induced non-linear conduction in epitaxial $La_{0.7}A_{0.3}MnO_3$ manganite thin films

   P.S. Vachhani, P.S. Solanki, J.H. Markna, R.N. Parmar, J.A. Bhalodia and D.G. Kuberkar

   Indian J. Eng. Mater. Sci. **14**, 163 (2007)

6. Grain size dependent transport and magnetoresistance behavior of CSD grown nanostructured LSMO manganite thin films

   R.N. Parmar, J.H. Markna, P.S. Solanki, **P.S. Vachhani** and D.G. Kuberkar

   J. Nanosci. Nanotechnol. **8**, 4146-4151 (2008)

7. High field sensitivity at room temperature in p-n junction based bi-layered manganite devices

   P.S. Vachhani, J.H. Markna, R.J. Choudhary, D.M. Phase and D.G. Kuberkar

   Appl. Phys. Lett. **92**, 043506 (2008)

8. Nano - Engineering by implanting Al_2O_3 nano particle as sandwiched scattering centers in between the $La_{0.5}Pr_{0.2}Sr_{0.3}MnO_3$ thin film layers

   J.H. Markna, **P.S. Vachhani**, N.A Shah, P. Misra, B.N. Singh, L.M. Kukreja, D.S. Rana and D.G. Kuberkar

   J. Nanosci. Nanotechnol. In press (2008)

9. Size dependent modifications in the physical properties of CSD and PLD grown $La_{0.7}Ca_{0.3}MnO_3$ manganite thin films: a comparative study

   J.H. Markna, **P.S. Vachhani**, N.A. Shah, J. John, D.S. Rana, S.K. Malik and D.G. Kuberkar

   Indian J. Eng. Mater. Sci. In press (2008)

10. Improvement in field sensitivity of manganite based multilayered device

    P.S. Vachhani, J.H. Markna, P. Misra, B.N. Singh, L.M. Kukreja and D.G. Kuberkar

    Physica B (2008), Communicated

List of Publications in National and International Conferences

1. Studies on $La_{0.5}Pr_{0.2}Sr_{0.3}MnO_3$ epitaxial thin films: an application point of view

   J.H. Markna, R.N. Parmar, C.M. Thaker, **P.S. Vachhani**, J.A. Bhalodia, P. Misra, L.M. Kukreja and D.G. Kuberkar

   Presented in 3rd National symposium on Pulsed Laser Deposition of Thin Films and Nano-structured materials (PLD-2005) organized by DAE BRNS held at DOP, Srivenkateswara University, Tirupati, October 7-9, 2005

2. Non-linear I-V characteristic of $La_{0.7}A_{0.3}MnO_3$ (A = Sr, Ba) thin films grown using Chemical Solution Deposition

   P.S. Vachhani, P.S. Solanki, R.N. Parmar, J.H. Markna, N.A. Shah, D.S. Rana, J.A. Bhalodia, S.K. Malik and D.G. Kuberkar

   Presented in the 8th International Conference on Nanostructured Materials NANO-2006 held at IISc, Bangalore, August 20-25, 2006

3. Effect of cation size mismatch on electrical and magnetotransport in $La_{0.5}Pr_{0.2}Ba_{0.3}MnO_3$ manganite

   C.M. Thaker, D.S. Rana, **P.S. Vachhani**, R.N. Parmar, J.H. Markna, J.A. Bhalodia, S.K. Malik and D.G. Kuberkar

   Presented in National Conference on Advances in Materials Science (AMS-06) held at Gulbarga University, 2006

4. Grain size dependent transport and magnetoresistance behavior of CSD grown nanostructured LSMO manganite thin films

   R.N. Parmar, J.H. Markna, P.S. Solanki, **P.S. Vachhani** and D.G. Kuberkar

   Presented in the International Conference on Advanced Nano Materials (ANM-07) held at IIT, Mumbai during January 3-5, 2007

5. Comparative study on structural, electrical and magnetoresistive properties of $La_{0.5}Pr_{0.2}Ba_{0.3}MnO_3$ and $La_{0.7}Ca_{0.3}MnO_3$ thin films

   P.S. Vachhani, J.H. Markna, R.N. Parmar, R.R. Doshi, P.S. Solanki, J.A. Bhalodia, P. Misra, L.M. Kukreja, D.S. Rana, S.K. Malik and D.G. Kuberkar

   Presented in National Conference on Advances in Materials Science (AMS-07) held at Gulbarga University, Gulbarga, during January 18^{th} – 19^{th}, 2007

6. Improvement in field sensitivity of La-based manganite multilayered structure

   P.S. Vachhani, J.H. Markna, A.D. Joshi, J.A. Bhalodia, P. Misra, L.M. Kukreja, B.N. Singh, V. Ganesan, R. Rawat and D.G. Kuberkar

   Presented in 4th National symposium on Pulsed Laser Deposition of Thin Films and Nano-structured materials (PLD-2007) organized by DAE BRNS held at Saurashtra University, Rajkot during October 3-5, 2007

7. Improvement in the field sensing properties of layered manganite systems

   D.G. Kuberkar, **P.S. Vachhani**, P.S. Solanki, J.H. Markna, P. Misra, B.N. Singh, L.M. Kukreja and D.S. Rana

   Presented in International conference on the power of Nano and how it will impact your business Bangalore Nano held at Hotel the Grand Ashoka, Bangalore during December 6-7, 2007

8. Substrate dependent transport and magnetotransport in nanostructured manganite multilayer

   P.S. Vachhani, J.H. Markna, J.A. Bhalodia, P. Misra, B.N. Singh, L.M. Kukreja, V. Ganesan and D.G. Kuberkar

   Presented in International Conference on Nano science and Technology ICONSAT-2008 organized by DST held at Chennai during February 27-29, 2008

9. Nano-Engineering by implanting Al_2O_3 nanoparticle as sandwiched scattering centers in between the $La_{0.5}Pr_{0.2}Sr_{0.3}MnO_3$ thin film layers

   J.H. Markna, **P.S. Vachhani**, N.A. Shah, D.S. Rana, P. Misra, B.N. Singh, L.M. Kukreja and D.G. Kuberkar

   Presented in International Conference on Nano science and Technology ICONSAT-2008 organized by DST held at Chennai during February 27-29, 2008

Oral Presentation

1. Studies on PLD grown manganite based p-n junction devices

   P.S. Vachhani, J.H. Markna, J.A. Bhalodia, R.J. Choudhary, D.M. Phase and D.G. Kuberkar,

   Presented in IVth UGC-SAP Seminar on Advances in Materials Research (AMR-2008) held at Department of Physics, Saurashtra University, RAJKOT on 15th February, 2008.

2. Field sensitivity studies of PLD grown manganite based nanostructured p-n junction devices

   P.S. Vachhani, J.H. Markna, R.J. Choudhary, D.M. Phase and D.G. Kuberkar,

   Presented in One day workshop on Structural characterization of Nanomaterials (SCNM-08) held at M.S. University, Baroda on 30th March, 2008.

1.1 Introduction to manganites

After long attention to the field of superconductivity, the flow of research interest switched towards the studies on manganite materials owing to their potential applicability for various purposes. Manganites exhibit variety of interesting novel properties like, insulator to metal (I-M) transition, paramagnetic to ferromagnetic transition, Colossal Magnetoresistance (CMR) effect etc. Recent trend is towards the fabrication of thin films and devices based on manganite materials which can be useful as advanced magnetic recording systems, magnetic solid state memories, field and temperature sensors and magnetic microwave devices [1-3]. Though, extensive research work has been already carried out, the state-of-art facility with novel and easier synthesis technique is what one requires for successive growth and application of manganite thin films and multilayers for application in advanced technological fields. Already reported and lucratively fabricated multilayer devices of manganite system contain large number of layers [4]. The fabrication of these multilayer systems require atomic-level control of layers, defect free or either less defective interface between two layers, reproducibility of desired properties, higher operating temperature etc.

The mixed valent manganites possess a general stoichiometric formula, $Ln_{1-X}A_XMnO_3$ (Ln = rare-earth; A = divalent ion) and are antiferromagnetic at X = 0.0 [5-7]. At or above certain value of X (or Mn^{+4} content) they become ferromagnetic and metallic at temperature below the curie temperature, T_C. This behavior is commonly due to Zener double exchange (ZDE) [8], which cannot alone explain the various properties of manganites. The Jahn-Teller (JT) distortion should be also considered along with the ZDE which suggest that, the lattice distortion caused by Mn^{+3} ion (bond stretching in the MnO_6 octahedra) also plays a crucial role in attributing various properties to manganites [9]. Moreover, these manganites exhibit large magnetoresistance (MR) under the application of magnetic field.

Magnetoresistance (MR) is the relative change in resistance by the application of a magnetic field. It is generally defined as,

$$MR\% = \frac{\rho_H - \rho_0}{\rho_0} \times 100$$

where ρ_0 and ρ_H are the resistances or resistivities at a given temperature in the absence and presence of a magnetic field, respectively. MR can be negative or positive. Most metals show a small MR. Large MR, referred to as giant magnetoresistance (GMR), was first observed in magnetic superlattice Fe/Cr [10]. GMR is a result of the reduction of the extra resistance due to the scattering of electrons by the non-aligned ferromagnetic component in zero magnetic field. MR can be further classified into four categories:

a) Anisotropic magnetoresistance (AMR)

Magnetic field induced anisotropy in resistivity gives rise to anisotropic magnetoresistance.

b) Granular and tunneling magnetoresistance (TMR)

It arises in the granular systems due to the spin dependant scattering of carriers at either grain boundary or at insulating barrier.

c) Giant magnetoresistance (GMR)

GMR is mostly observed in metallic multilayers such as Fe/Cr, Co/Cu and is of the order of 40 to 50%. Owing to large amount of MR, name Giant magnetoresistance was given to emphasize the strength of MR in these materials.

d) Colossal magnetoresistance (CMR)

MR as large as ~ 100% was observed in manganites, so in order to describe such a gigantic amount of MR new term 'CMR' was coined.

1.1.1 Structure

$Ln_{1-X}A_XMnO_3$ manganite possesses ABO_3 type perovskite structure [A is rare earth element, B is transition metal, Mn in case of manganite]. Without hole doping, parent compounds such as $LaMnO_3$, $PrMnO_3$ and $NdMnO_3$ are insulators at all temperature which on hole doping [partial substitution of divalent ion at Ln-site] becomes ferromagnetic metallic below curie temperature (T_C) due to the creation of Mn^{+4} ions.

The two characteristic distortions which influence the perovskite structure of manganates are

i) Cooperative tilting of MnO_6 octahedra, is a consequence of the mismatch of the ionic radii which can be quantified as,

$$\sigma^2 = \sum x_i r_i^2 - < r_A >^2$$

where, x_i and r_i are fractional occupancy and ionic radius of i^{th} cation at A-site. $<r_A>$ is the average A-site cation radius and σ^2 is the A-site cationic size-variance. The effect of size-variance on the magnetoresistive properties of manganites has been first investigated by L.M. Rodriguez and Martinez et al [11]. It is reported that, at 1.23 Å average A-site cation radius one can get maximum insulator-metal (I-M) transition temperature and further modifications in $<r_A>$ results in decrease in I-M transition temperature [12-14]. In addition, effect of simultaneous size-disorder and carrier density on transport and magnetotransport properties of manganites have been studied by D.S. Rana et al [15].

ii) The other distortion, arising from the Jahn-Teller effect due to Mn^{+3}, distorts the MnO_6 octahedra in such a way that there are long and short Mn-O bonds. The mismatch of the ionic radii,

$$t = \frac{< r_A > + r_O}{\sqrt{2}(< r_B > + r_O)}$$

where 't' known as tolerance factor is a measure of deviation from a perfect cubic crystal structure (for cubic t = 1) [16]. The other parameters $<r_A>$, $<r_B>$ and r_O are the average radii of the A cation, B cation and oxygen ion, respectively. The cubic structure transforms to rhombohedral when the value of t approaches in the range $0.96 < t < 1$ and for $t < 0.96$ orthorhombic structure is present in which Mn-O-Mn bond angle θ is deviated from 180º.

Among these structural transformations, the parent $LaMnO_3$ possesses orthorhombic distortions. With the substitution of La by a divalent ion, orthorhombic distortion decreases and structure becomes either rhombohedral or pseudo-cubic depending on tolerance factor value, as described above. Besides the distortion due to mismatch of ionic radii at A-site, the distortion due to Mn^{+3} ions, called as Jahn-Teller distortion also plays a major role in modifying the structural, transport and magnetotransport properties of manganites.

Fig. 1.1 shows the effect of average A-site cation radius $<r_A>$ and tolerance factor 't' on I-M transition temperature of manganites. The value of T_P becomes maximum when the value of $<r_A>$ and t becomes 1.23 Å and 0.93 Å, respectively.

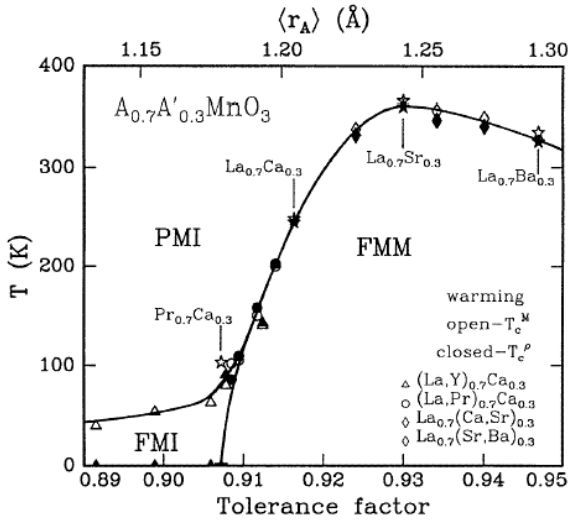

Figure 1.1 : The effect of average A-site cation radius $<r_A>$ and tolerance factor "t" on I-M transition temperature [17].

- **Zener double exchange (ZDE)**

The ZDE is responsible for the transformation from paramagnetic insulating (PI) state to ferromagnetic metallic (FMM) state.

In $LaMnO_3$, the Mn ions are octahedrally surrounded by oxygen ions. Mn^{+3} ions have an outer orbital electronic configuration as $3d^4$ which further splits the five degenerate d orbitals into triply degenerate t_{2g} and doubly degenerate e_g orbitals as shown in fig. 1.2. The three electrons of $3d^4$ orbitals in the Mn^{+3} ions are arranged in the t_{2g} levels, while remaining one electron occupy the e_g level due to strong Hund's rule coupling which favors high-spin configuration. The divalent cation doped at La-site converts Mn^{+3} to the Mn^{+4} state, with proportion equal to the amount of divalent doping at La-site. Thus, the conduction takes place between these adjacent Mn^{+3} and Mn^{+4} ions. The e_g electrons of Mn^{+3} (d^4, $t_{2g}^3 e_g^1$, s = 2) experiences a net potential difference with respect to vacant site of Mn^{+4} (d^3, t_{2g}^3, s = 3/2) and hence possess a tendency to hop to the vacant site. This hopping process is possible through the ligand oxygen, which has two 2P (spin ↑ and spin ↓) electrons in outermost orbital. The e_g electron of Mn^{+3} hops to spin up

orbital of oxygen ion. According to Hund's rule, an orbital can occupy only one electron, the oxygen ion accepts the e_g electron of Mn^{+3} ion by giving its own spin up electron to Mn^{+4} ion.

$$Mn^{+3}\ O^{-2}\ Mn^{+4} \longrightarrow Mn^{+4}\ O^{-2}\ Mn^{+3}$$

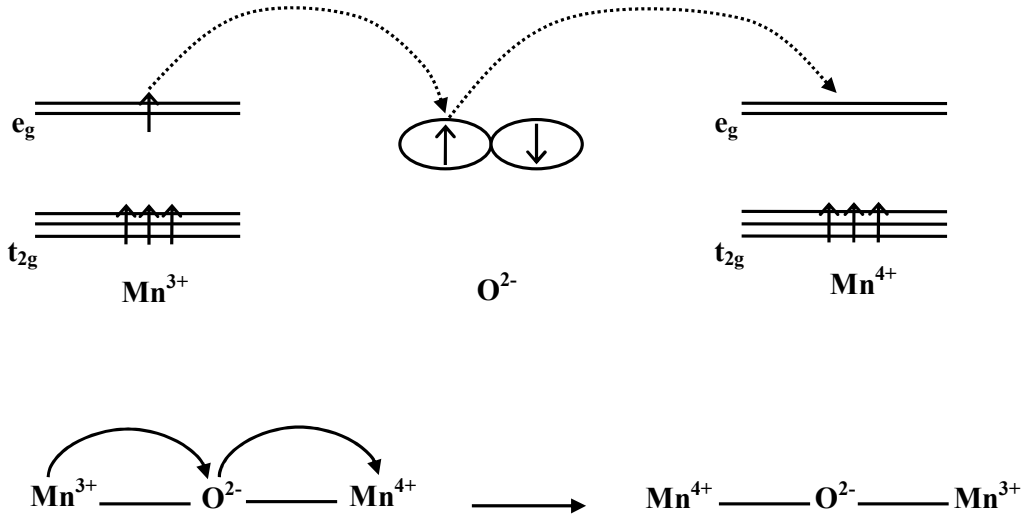

Figure 1.2: Schematic representation of Zener-Double exchange. The e_g electron of Mn^{3+} transfers to intermediate ligand oxygen which in turn transfers its electron to e_g level of Mn^{4+} ion.

The t_{2g}^3 electrons of the Mn^{+3} ions are localized on the Mn site giving rise to a local spin of 3/2, but the e_g state, which is hybridized with the oxygen 2P state, can be localized or itinerant and only those electrons which have their spins parallel alignment give rise to conductivity in the hopping process. Goodenough pointed out that ferromagnetism is governed not only by double exchange, but also by the nature of the superexchange interaction. Mn^{+3}-O-Mn^{+4} superexchange interaction is ferromagnetic while the Mn^{+3}-O-Mn^{+3} and Mn^{+4}-O-Mn^{+4} interactions are antiferromagnetic [18].

In general, the X = 0.0 and X = 1.0 members of the $L_{1-X}A_XMnO_3$ systems are AFM insulators at low temperatures while ferromagnetic behavior starts to manifest itself at X ~ 0.1 and the compositions up to X ~ 0.3 have both AFM and FM characteristics. The X = 0.3 composition is clearly ferromagnetic, while the X > 0.5 compositions are antiferromagnetic. $LaMnO_3$ has three characteristics Mn-O distances (1.91 Å, 1.96 Å and 2.19 Å) and Mn-O-Mn angle of ~ 150º. The creation of Mn^{+4} ions removes the distortion leading to more cubic structures.

- **Jahn-Teller (JT) Distortion**

JT distortion is a parameter that largely influences the electrical and magnetic properties of manganites. According to JT theorem, "Any nonlinear molecular system in a degenerate electronic state will be unstable and will undergo distortion to form a system of lower symmetry and energy thereby removing the degeneracy". Therefore, in case of Mn^{+3} ion having one electron in the e_g level, degeneracy is lifted and its energy is lowered, which results in distortion of MnO_6 octahedra. This distortion, compresses the MnO_6 octahedra along ab-plane and elongates along c-plane, thus, resulting in reduced overlap of Mn 3d-orbitals and oxygen p-orbitals. While in Mn^{+4} ion, there are no electrons in the e_g level, hence MnO_6 octahedra is not distorted. The compression of MnO_6 octahedra along ab-plane and elongation along c-plane is schematically illustrated in fig. 1.3.

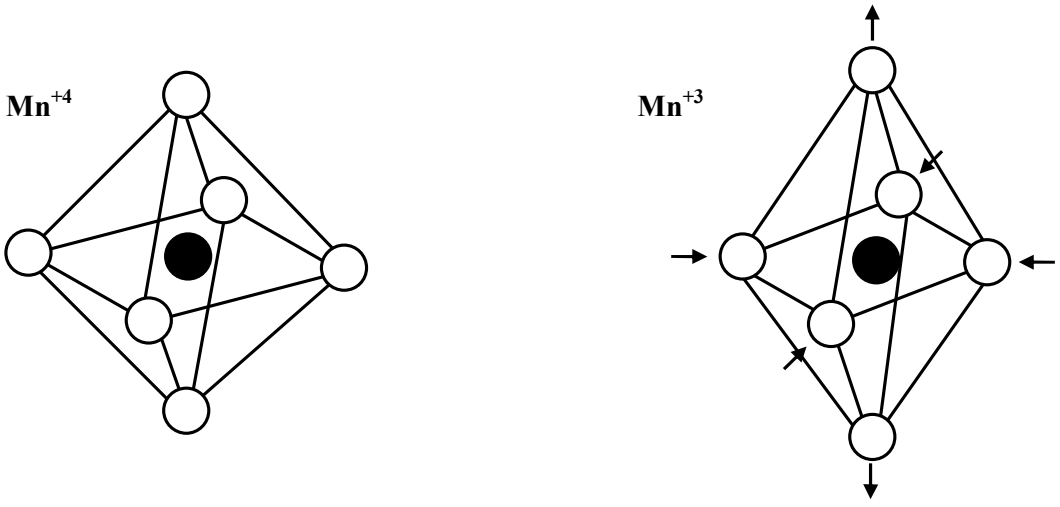

Figure 1.3 : Schematic diagram of distortion of MnO_6 octahedra in JT distortion.

1.1.2 Transport properties

Mixed valent manganites exhibit two kinds of transitions, one is insulator to metal transition (T_P) and another is paramagnetic to ferromagnetic transition (T_C). Most of the $La_{1-X}A_XMnO_3$ compositions are paramagnetic insulators at ordinary temperatures and exhibit an increase in electrical resistivity with a decrease in temperature but when they are cooled below T_C, insulator-metal (I-M) transition occurs in the vicinity of paramagnetic to ferromagnetic transition.

1) Transport in the paramagnetic insulating (PI) phase ($T > T_C$)

The manganites doped with larger cations such as Sr, Ba and Pb have a larger bandwidth means resulting I-M transition is broad. For, manganites doped with relatively smaller cations like Ca, the bandwidth would be small and have sharp I-M transition.

In order to understand, why the paramagnetic phase at $T > T_C$ is insulating the researchers tried to find out the theory which can be applied to the conduction in this region. Some investigations indicate that, a Variable Range Hopping (VRH) type of expression $\rho = \rho_{oh} \exp (T_0/T)^{1/4}$ holds good above T_C [19]. However, the problem is that one obtains unrealistic value of T_0. Some authors argue in favour of lattice polaron formation and have fitted the resistivity to expressions of the type $(\rho/T) \sim \rho_{op} \exp (E_a/K_BT)$ [20]. Here, E_a is the small polaron hopping energy. But, it is difficult to distinguish between VRH, Small polaron hopping and the simple semiconductor form; $\rho \sim \exp (E/K_BT)$.

2) The ferromagnetic metallic state ($T < T_C$)

In the ferromagnetic metallic state, manganites, in general, follow electron scattering power law of the form $\rho (T) = \rho_0 + BT^n$ where, $\rho (T)$ is the resistivity at temperature T, B is electron-magnon co-efficient and ρ_0 is residual resistivity. The value of parameter "n" quantifies which scattering mechanism is dominant. The value of $n \sim 2$ leads to electron-electron scattering [21], $n \sim 2.5$ leads to one-magnon scattering law [22] while $n \sim 3$ leads to unconventional one-magnon scattering law [23].

Various parameters affecting transport and magnetotransport properties of manganites are discussed in brief in the following pages.

The effect of magnetic field

Application of a magnetic field causes a significant decrease in the resistivity of the $L_{1-X}A_XMnO_3$ samples. The magnitude of the decrease in resistivity (i.e. MR) is highest in the vicinity of T_C or T_P. La-deficient, $La_{1-\delta}MnO_3$ compositions also exhibit CMR, but Mn-deficient $LaMn_{1-\delta'}O_3$ samples do not when $\delta' > 0.05$ [24]. Mn deficiency affecting the magnetotransport properties of CMR, can be understood since the active electrical and magnetic network is made up of Mn-O-Mn bonds. Thus, it results in lowering of the T_C and enhancement in the resistivity. In addition, oxygen content is the major parameter affecting transport and magnetotransport properties. Nearly stoichiometric manganites can be prepared by firing pellet in a low oxygen pressure, in nitrogen [25, 26], or in argon [27].

Role of electron lattice coupling

When $X \sim 0.2$, in manganites, local structural distortions occur due to the formation of lattice polarons which arises from the strong electron-lattice coupling. EXAFS studies revealed that the formation of small polarons due to the Jahn-Teller distortion takes place when $T > T_C$ [28, 29].

Effect of external and internal pressure

Hydrostatic pressure stabilizes the ferromagnetic metallic state of $La_{1-X}A_xMnO_3$. The effect of hydrostatic pressure is to enhance the Mn-O-Mn transfer integral through a change in the Mn-O-Mn angle [30]. A similar effect can be brought about by increasing the radius of the A-site cation. This hydrostatic pressure can be considered as external pressure where as pressure by modifying the $\langle r_A \rangle$ is known as internal pressure.

MR generally decreases with increase in average A-site cationic radius ($\langle r_A \rangle$). MR is therefore favored by low T_C and high peak resistivity [31].

Effect of grain boundaries

The T_C decreases with decreasing particle size while I-M transition becomes broader when the particle size is smaller. The effect of grain boundary on MR is quite

different in single crystalline thin film as compared to polycrystalline bulk sample. To understand this, let us see, the causes for observation of MR in the manganites i) The magnetic field induced reduction in magnetic spin disorder at Mn-O-Mn bonds i.e. intrinsic MR ii) The magnetic field induced reduction in spin dependent scattering at grain boundaries i.e. extrinsic MR. At low temperature, the contribution from intrinsic MR is negligible since all the spins are aligned. However, polycrystalline bulk sample exhibits quite good MR which can be attributed to the extrinsic MR. In polycrystalline bulk large number of grain boundary exists. However the spin in two different grains are not aligned, so on the application of magnetic field, spin-polarized carriers can easily tunnel through the grain boundaries resulting large low temperature MR. While in thin film, since there are ideally no grain boundaries, MR is almost zero [32].

Effect of strain

Strain is the one parameter which differentiates thin film from their bulk counterpart. In order to study the strain effect, one could use different substrates and thicknesses of films and compare the results. Strain can either be compressive or tensile depending on which kind of substrate and material is used for deposition [33].

1.2 Manganite thin films

The current trend in the development in manganite research is towards the fabrication of novel type of devices, monolithic hybrid circuits, field effect transistors (FET), metal oxide semiconductor transistor (MOST), sensors for different applications (for example, field and temperature sensing), switching devices, cryogenic applications, high density memory systems for computers, etc. In-depth investigations are in progress not only in the field of basic thin film physics but also in materials science, thin film circuit design, etc. to cope up the demand of industries. Film properties are sensitive not only to their structure but also to many other parameters including thickness especially in the thin film regime. Hence the control over the parameters, other than structure, is crucial for reproducible electronic, magnetoelectronic, magnetic, dielectric, optical and other properties.

- **Thin Films & their Growth**

The proper knowledge about the basic concepts of thin films, the synthesis of good quality films having atomically smooth surface and epitaxy, strain and defect free interface with substrates helps in understanding the film growth and their properties [34]. These desirable physical properties can be achieved by optimizing thin film growth parameters. The ideal condition of the film synthesis involves the deposition of the material atom by atom (or molecule by molecule) and layer by layer with an ample time interval between the two consecutive depositions of atoms and also layers so that they can occupy the minimum potential energy configuration with respect to the substrate and subsequently on previously deposited layers. Hence, resultant films have a lesser amount of strain between two subsequent layers. The following properties illustrate various mechanisms occurring at different stages of film growth.

There are several stages in the growth process, from the initial nucleation of the deposits to the final continuous three dimensional film formation state.

1) Nucleation (including condensation of vapours, adsorption of atoms, migration of ad-atoms, formation of critical nuclei, stable clusters etc.
2) Island structure
3) Coalescence of island with gaps in between
4) Joining of larger islands with the formation of channels
5) Continuous film stage

These sequences are discussed in brief and schematically illustrated in fig. 1.4.

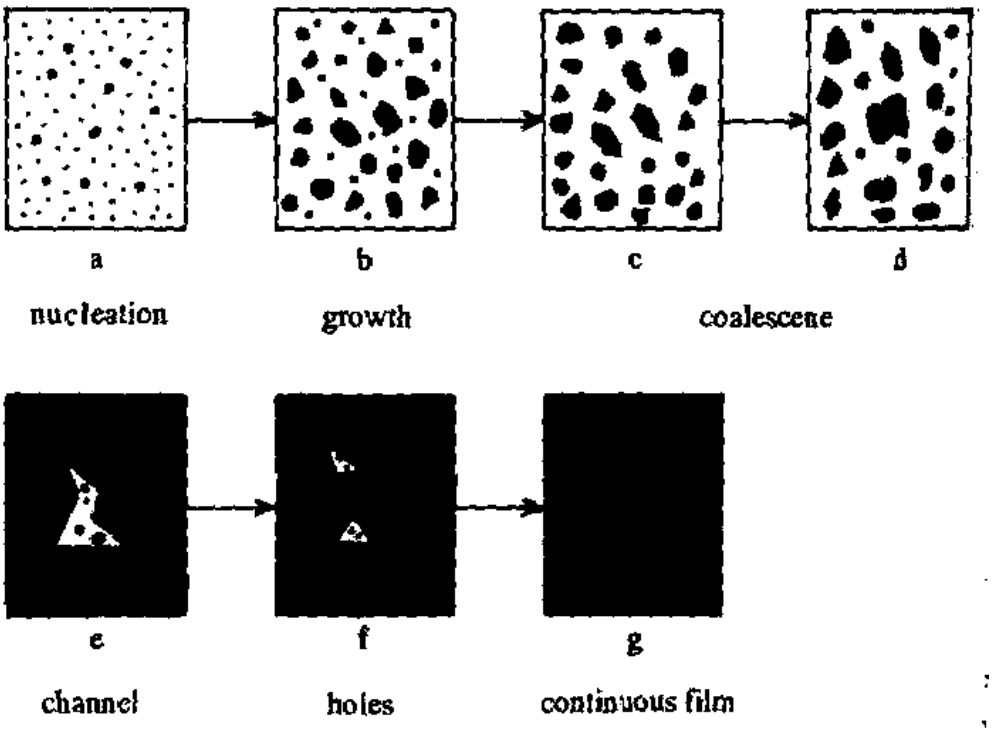

Figure 1.4 : Schematic representation of thin film growth mechanism having different stages like, nucleation, growth, coalescene, channel, holes and continuous film.

1) Nucleation stage

Nucleation or small cluster formation is the primary process for all deposition. The common process of addition, adsorption, desorption, migrations, etc. of atoms is called nucleation or small cluster formation which is schematically shown in fig. 1.4 (a).

In the prenucleation stage, several phenomena occur either simultaneously or step by step 1) the physical condensation of vapour atoms 2) these are then adsorbed on the substrate surface 3) adsorbed species (monomer) may then move over the substrate surface (hoping or migration or diffusion) 4) these monomers have certain time of residence over the substrate surface 5) monomers after migration collide to form clusters 6) impinging atoms can be reflected back to vapour state without condensation. The same sequence repeats after each impingement of atoms [35, 36].

2) Island structure stage

The schematic representation of island structure is illustrated in fig. 1.4 (b). These islands consist of comparatively larger nuclei (> 10 Å) and generally of three dimensional nature with their height, however, much less then their lateral dimensions. Electron microscopic observations by various workers show that the smallest stable nuclei are of radii ~ 5 Å. Since the nucleus of about 5 Å size is made up of about 20 atoms or so, an island will be made up about 50-100 atoms or more.

3) Coalescence stage

As mentioned in the second stage, as islands are grown they hold some typical profile and then with further growth, coalesce with the neighboring ones by rounding of their boundaries near the amalgamation region (narrow part). Small islands disappear rapidly. The process is similar to the sintering of bulk powder where the individual particle coalescence of two islands occurs at their narrow regions. Recrystallization as well as annealing takes place leading to some definite shapes of bigger islands [figs. 1.4 (c) & (d)].

4) Channel stage and Holes

As the coalescence continues with deposition, there will be a resultant network of the film with channels in between [fig. 1.4 (e)]. Some times, with increasing film thickness in these channels some holes or gaps in the aggregate mass are left [fig. 1.4 (f)].

5) Continuous film stage

When these gaps are completely bridged by the secondary nuclei, films will be continuous. However, it often happens that some void space may still remain unbriged. In an ideal continuous film there should not be any gap in the aggregate mass. Such a stage in the film can be attained at certain average film thickness [fig. 1.4 (g)].

1.3 Manganite based devices

The technological application of manganites demand the material in the thin film form. A large amount of work has been devoted to develop and fabricate the manganite based devices applicable as field and temperature sensors etc.

First serious attempt towards development of manganite based devices lead to the fabrication of trilayered device consisting of one insulating layer sandwiched between two manganite layers. The epitaxial trilayer junction device in the form of [(top electrode) $La_{0.67}Sr_{0.33}MnO_3$] / (insulating layer) $SrTiO_3$ / [(bottom electrode) $La_{0.67}Sr_{0.33}MnO_3$] was fabricated which showed a large MR ~ 83% at 4.2 K under small applied field [37]. The sandwiched layer was composed of insulating material that caused detrimental interface states which reduced tunneling magnetoresistance through insulating layer and hence MR at higher temperature. In order to suppress this detrimental effect on TMR, H.Q. Lin et al used similar material having different stoichiometry as a sandwiched layer [$La_{0.67}Sr_{0.33}MnO_3$/ $La_{0.85}Sr_{0.15}MnO_3$/ $La_{0.67}Sr_{0.33}MnO_3$]and had observed ~ 5% MR around 230 K in 1000 Oe field [38].

Moreover, recently some researchers have grown p-n type bilayered junction devices in which manganite layer serve as p-type material and either Nb- or La doped $LaAlO_3/SrTiO_3$ serve as n-type substrate. These bilayered junction device exhibit novel properties such as, diode like behavior, crossover in MR from positive to negative as a function of temperature, high field sensitivity and also modulation of all these distinct behaviors with the application of either electric of magnetic field.

1.4 Applications of manganite thin films and multilayers

By virtue of variety of interesting transport and magnetic properties of mixed valent manganites, these materials are highly useful in several applications which are mentioned below -

1. Magnetic memory read heads and spin valves

The first step towards using the spin degree of freedom as a spin valve is magnetic multilayer composed of alternative ferromagnetic and nonmagnetic layers. The resistance

of such a combined layer becomes lowest when magnetic moment of both ferromagnetic layers is aligned and is highest when they are antiparallel. This causes large magnetoresistance called as Giant MR (GMR). In spin valves, the magnetic configuration can be switched by a very low field, so that under low field, a large change in resistance is observed. Today, all computers & laptops use spin-valves for read heads of the hard disc. The density of stored data has reached the saturation with conventional spin-valves. For further increase in the density of stored data, the magnetic tunnel junctions (MTJs) have been explored where current passes in current perpendicular to plane (CPP) mode [39, 40].

MTJs and MRAM

MTJ is a trilayer junction in which two ferromagnetic layers (electrodes) are separated by a thin insulating layer, normally aluminium oxide (Fig. 1.5). The electrons can tunnel through the insulating layer. Moreover, the probability for electron tunnel through the insulating barrier depends on spin direction, either parallel or antiparallel configuration [41, 42]. The MTJs of very tiny dimension (in the micron range) can be fabricated by lithographic techniques and can be applicable for a novel type of computer memory, known as Magnetic Random Access Memory (MRAM) as shown in fig. 1.6. Every single junction can store one bit of data say "0" for the parallel configuration and "1" for the antiparallel configuration.

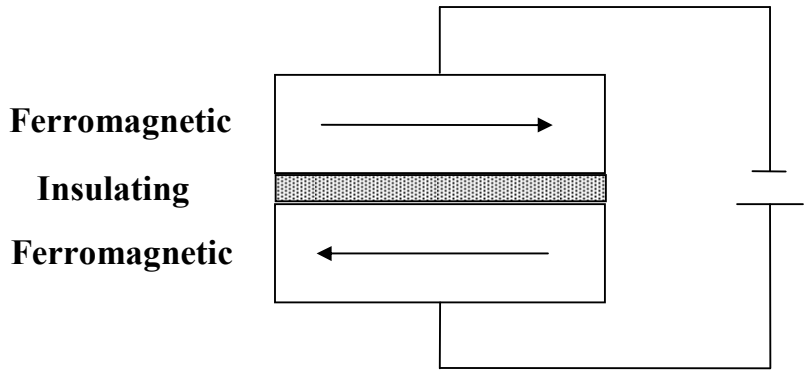

Figure 1.5 : Schematic diagram representing a MTJ.

In future, the MRAMs are expected to reach similar capacity of storing data and access time as the current DRAM and SRAM. The key advantage of MRAMs over the conventional semiconductor based memories is that, they retain data even after the power is turned off. Moreover, the MRAMs have also an important advantage in terms of speed over the permanent memories of flash type used for mobile electronics. A record TMR ratio of 1800% has been found with electrode of the manganite $La_{0.67}Sr_{0.33}MnO_3$, however at low temperature [43].

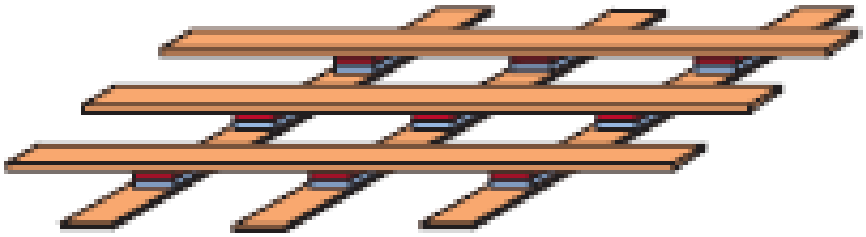

Figure 1.6 : Schematic representation of RAM that is constructed of magnetic tunnel junction connected together in a point contact array.

MTJs can also be considered as excellent candidates to be used as magnetoresistive materials in all above mentioned applications. Moreover, due to their greater field sensitivity they can also be used for aeronautical and space industry.

2. Bolometer IR sensors

Another striking application of manganite thin films is, in IR sensors (Bolometer). The properties of material to be used in IR sensors are, higher operating temperature, large temperature coefficient of resistance (TCR) and low noise ratio. The manganite thin films exhibit large TCR value at reasonably higher temperatures which makes them suitable for application in bolometer. The TCR defined as $1/R(dR/dT)\times100$ % is measure of change in resistance per unit temperature. A conventional superconductor bolometer or bolometer based on V_2O_3 possesses TCR of ~ 3-4% while in $La_{0.7}Ca_{0.3}MnO_3$, TCR as high as 10-18% has been obtained in bulk form which can be increased up to ~ 35% in thin films.

Moreover, further attempts have been made by researchers in order to improve TCR and its operating temperature having low noise ratio by growing composites (manganite-metals), by substituting smaller size cation at A-site, by irradiating thin film of manganite by energetic Ag^{+15} Swift heavy ion (SHI).

3. Hybrid HTSC-CMR devices

One more use of CMR materials is as HTSC-CMR hybrid devices. From the double exchange, the degree of polarization of the charge carriers is very close to 100% unlike classical ferromagnets [44, 45]. This means CMR materials could be used as a source of spin-polarized charges for carrier injection studies. Furthermore, the CMR materials possess perovskite crystal structure, and hence can be grown epitaxially on high-T_C superconductors. Keeping all these things in mind, researchers had grown hybrid HTSC-CMR devices. In these kind of devices, current flows in the ferromagnetic CMR layer which decreases the critical current of superconducting layer due to the pair breaking phenomenon by spin-polarized carriers while crossing boundary between the ferromagnet and superconductors [46-48]. This device can be used as FET. So, I-V characteristics as a function of gate current is well studied in these type of hybrid HTSC-CMR devices.

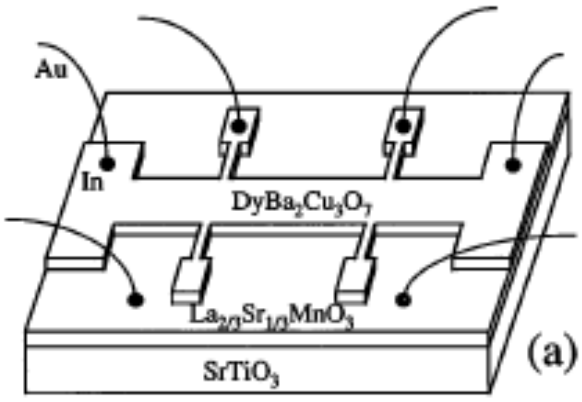

Figure 1.7 : Reproduced diagram of HTSC-CMR device [49].

4. Electric field effect devices

One more application of CMR materials is in the form of FETs having CMR layer combined with either dielectric layer or ferroelectric layer [50]. In these devices, one can observe electric field induced modulation in the resistance. In case of STO (dielectric) based device, polarity of electric field has no effect on the response of device but T_P shifts to lower temperature while in PZT (ferroelectric) large change in resistance has been observed [51].

1.5 Motivation of the present work

The manganites having general formula $R_{1-X}A_XMnO_3$ (R = rare earth trivalent cation, A = divalent cation) exhibit dual novel properties such as negative colossal MR and the metal-insulator (M-I) transition in the vicinity of magnetic transition (paramagnetic to ferromagnetic) which have been explained in terms of correlation between spin, charge and orbital degrees of freedom. The physical properties of these compounds depend on two main factors: divalent doping at R site, cooperative tilting of MnO_6 octahedra either due to mismatch of the ionic radii or due to the Mn^{+3} ion.

The motivation and aim for the present work is to develop advanced devices based on manganite thin films for the application as a data storage device, memory device, temperature and field sensing device etc. Also, it is planned to explore the unknown physics behind the working principle of these devices. Moreover, with an aim to develop the new route for manganite thin film deposition (Chemical Solution Deposition) having advantages like faster, easier, low reaction and annealing temperature, cost-effectiveness, I have grown various manganite thin films. In addition, manganite multilayers consisting alternate five layers of $La_{0.5}Pr_{0.2}Sr_{0.3}MnO_3$ and $La_{0.5}Pr_{0.2}Ba_{0.3}MnO_3$ on different substrates have been fabricated with an aim to improve the field and temperature sensitivity and operating temperature of multilayer device. Also, the effect of different substrate induced strain on multilayer has been studied. The most interesting part of this thesis work comprisie of, the development of bi-layered P-N junction device based on manganite thin films and the detailed study of its structural, surface morphological and magneto I-V properties. Moreover, a systematic attempt has been made to study the effect of thickness and carrier density on the various physical properties of this bi-layered P-N junction

device. In the end, Swift Heavy Ion (SHI) irradiation effect on the transport properties of $La_{0.5}Pr_{0.2}Ba_{0.3}MnO_3$ (LPBMO) manganite thin film, grown using Chemical Solution Deposition (CSD) technique, have been studied. It is found that the T_P of LPBMO film reduces in films subjected to all irradiation doses except 5 X 10^{11} ions/cm^2 dose. The reason has been explained on the basis of modifications in the strain, enhancement in amorphous parts and pressure induced by irradiation.

Details of all the subsequent chapters comprising thesis are given below

Chapter I

This chapter contains the introductory part of manganite and various physical properties exhibited by them. Also, the several stages in the thin film growth process involving the initial nucleation of the deposits to the final continuous three dimensional film formation in the ideal condition has been illustrated. In addition, the review of various devices based on manganites have been given in this chapter. At the end of this chapter, the information about the advanced technological applications of manganite thin films and multilayered devices such as spin-valve, data storage, read write head, sensors have been given.

Chapter II

Chapter II comprise of the details about various synthesis techniques used such as, Solid State method for synthesis of bulk while, CSD and Pulsed Laser Deposition (PLD) techniques for synthesis of thin film and multilayers. A variety of experimental techniques used for characterization of bulk, film and multilayers. This chaper also explain the use of XRD & HRXRD techniques for checking the phase purity, impurity and the epitaxial growth of thin films. The working principle and other aspects of characterization technique like Atomic Force Microscopy (AFM), d.c. four probe resistivity has been discussed.

Chapter III

Chapter III deals with the studies on electronic transport and magnetotransport properties of manganite based multilayers of $La_{0.5}Pr_{0.2}Sr_{0.3}MnO_3$ (5 layers) / $La_{0.5}Pr_{0.2}Ba_{0.3}MnO_3$ (4 layers) grown by PLD technique on different substrates. It has been shown that sandwiched $La_{0.5}Pr_{0.2}Ba_{0.3}MnO_3$ layer between two $La_{0.5}Pr_{0.2}Sr_{0.3}MnO_3$ layers acts as source of scattering center and due to this the multilayer exhibit large MR in the vicinity of room temperature. Owing to existence of large MR at higher temperature, the multilayer studied can prove to be a promising candidate for use as field sensing device.

Chapter IV

This chapter is completely devoted to the newly developed p-n junction devices based on manganites, grown with an aim to study and understand the effect of carrier

density and thickness of p-type manganite layer on magneto I-V behaviour of device. In this study, $La_{0.8-X}Pr_{0.2}Sr_XMnO_3$ (X = 0.2 and 0.3) (p-type)/$SrNb_{0.20}Ti_{0.80}O3$ (n-type) p-n device has been grown to study its field dependant I-V characteristics.

Chapter V

Chapter 5 contains two parts, among which first one contain the studies of the effect of SHI irradiation on the $La_{0.5}Pr_{0.2}Ba_{0.3}MnO_3$ (LPBMO) manganite thin films grown using Chemical Solution Deposition (CSD) technique. It is observed that the, T_P of LPBMO film is suppressed except the film subjected to all irradiation dose except 5 X 10^{11} ions/cm^2 dose. It is explained using different factors affecting T_P of LPBMO films such as i) Strain release at the interface ii) defects & pressure induced due to irradiation. In the second part, the effect of doping of smaller Lu ion at A-site in $La_{0.7}Sr_{0.3}MnO_3$ (LSMO) has been studied. In addition, thin films of Lu-doped LSMO have been grown on different substrates using Pulsed Laser Deposition (PLD) technique to study the effect of microstructure on the magnetotransport properties of Lu-doped LSMO films.

References

1. S. A. Wolf, D. D. Awschalom, R. A. Buhrman, J. M. Daughton, S. von Molnar, M. L. Roukes, A. Y. Chtchelkanova, D. M. Treger, Science **294**, 1488 (2001).
2. M. Tondra et al., J. Appl. Phys. **83**, 6688 (1998).
3. G.A. Prinz, Science **282**, 1660 (1998).
4. C. Kwon, K.-C. Kim, M.C. Robson, J.Y. Gu, M. Rajeswari, T. Venkatesan and R. Ramesh, J. Appl. Phys. **81**, 4950 (1997)
5. "Colossal Magnetoresistance, charge ordering and other related properties of rare earth manganates", ed. by C. N. R. Rao and B. Raveau, World Scientifics Publishing Company (1998).
6. E. Dagotto, T. Hotta, A. Moreo, Physics Report **344**, 1-153 (2001).
7. J.M.D. Coey and M. Viret, Advances in Physics, **48**, 2, 167 (1999).
8. C. Zener, Phys. Rev. **82**, 403 (1951).
9. A.J. Millis, P.B. Littlewood and B.I. Shraiman, Phys. Rev. Lett. **75**, 5144 (1995).
10. M.N. Baibich, J.M. Baroto, A. Fert, F.N. Vandau, F. Petroff, P. Etienne, G. Creuget, A. Freiderich, J. Chagelas, Phys. Rev. Lett. **61**, 2472 (1988).
11. L.M. Rodriguez-Martinez and J.P. Attfield, Phys. Rev. B **54**, R15622 (1996).
12. L.M. Rodriguez-Martinez and J.P. Attfield, Phys. Rev. B **58**, 2426 (1998).
13. A. Sundaresan, A. Maignan and B. Raveau, Phys. Rev. B **56**, 5092 (1997).
14. F. Damay, A. Maignan, C. Martin and B. Raveau, J. Appl. Phys. **81**, 1372 (1997).
15. D.S. Rana, C.M. Thaker, K.R. Mavani, D.G. Kuberkar, Darshan C. Kundaliya and S.K. Malik, J. Appl. Phys. **95**, 4934 (2004).
16. "Geochemistry", ed. by V. Goldschmidt, Oxford University Press (1958).
17. H.Y. Hwang, S.W. Cheong, P.G. Radaelli, M. Marezio and B. Batlogg Phys. Rev. Lett. 75, 914 (1995)
18. J.B. Goodenough, Phys. Rev. **100,** 564 (1955).

19. Y.X. Jia, L. Lu, K. Khazeni, V.H. Crespi, A. Zettl and M.L. Cohen, Phys. Rev. B **52**, 9147 (1995).

20. G. J. Snyder, R. Hiskes, S. Di Cariolis, M. R. Beesley and T. H. Geballe, Phy. Rev. B **53**, 14434 (1996).

21. P. Schiffer, A. P. Ramirez, W. Bao, and S-W. Cheong, Phys. Rev. Lett. **75**, 3336 (1995).

22. Li Pi, Lei Zheng, and Yuheng Zhang, Phys. Rev. B **61**, 8917 (2002)

23. E. Berkowitz, J. R. Mitchell, M. J. Carey, A. P. Young, S. Zhang, F. E. Spada, F. T. Parker, A. Hutten, and G. Thomas, Phys. Rev. Lett. **68**, 3745 (1992)

24. A. Arulraj et al, J. Solid State Chem. **127**, 87 (1996).

25. G. Jonker and J. Van Santen, Physica **16**, 337 (1950).

26. Q.A. Huang, A. Santoro, J.W. Lynn, R.W. Erwin, J.A. Borchers, J.L. Peng and R.L. Greene, Phys. Rev. B **55**, 14987 (1997).

27. A. Urushibara, Y. Moritomo, T. Arima, A. Asamitsu, G. Kido and Y. Tokura, Phys. Rev. B **51**, 14103 (1995).

28. S.J.L. Brillinge, R.G. DiFrancesco, G.H. Kwei, J.J. Neumeier and J.D. Thompson, Phys. Rev. Lett. **77**, 715 (1996).

29. T.A. Tyson, J. Mustre de Leon, S.D. Conradson, A.R. Bishop, J.J. Neumeier, H. Roder and Jun Zang, Phys. Rev. B **53**, 13985 (1996).

30. Y. Moritomo, A. Asamitsu and Y. Tokura, Phys. Rev. B **51**, 16491 (1995).

31. R. Mahesh, R. Mahendiran, A.K. Raichaudhury and C.N.R. Rao, J. Solid State Chem. **120**, 204 (1995).

32. R. Mahesh, R. Mahendiran, A.K. Raichaudhury and C.N.R. Rao, Appl. Phys. Lett. **68**, 2291 (1996).

33. C.S. Nelson, J.P. Hill, Doon Gibbs, M. Rajeswari, A. Biswas, S. Shinde, R.L. Greene, T. Venkatesan, A.J. Millis, F. Yokaichiya, C. Giles, D. Casa, C.T. Venkataraman and T. Gog, J. Phys.: Condens. Matter. **16**, 13 (2004).

34. Neugebauer C. , (1970) Handbook of thin film technology (ed. Maisse L. and Glang R. , McGraw-Hill Co., New York) chapter 8.

35. D.W. Pashley, M.J. Stowell, M.H. Jacobs and T.J. Law, Phil. Mag. **10**, 127 (1964).

36. D.W. Pashley, Adv. Phys. **14**, 61 (1965).

37. Yu Lu, X.W. Li, G.Q. Gong, Gang Xiao, A. Gupta, P. Lecoeur, J.Z. Sun, Y.Y. Wang and V. P. Dravid, Phys. Rev. B **54**, R8357 (1996).

38. H. Q. Yin, J.-S. Zhou, and J. B. Goodenough, Appl. Phys. Lett. 77, 714 (2000).

39. M.N. Baibich, J.M. Broto, A. Fert, F. Nguyen Van Deu, F. Petroff, P. Eitenne, G. Creuzet, A. Friederich and J. Chazelas, Phys. Rev. Lett. **61**, 2472 (1988).

40. G. Binasch, P. Grunberg, F. Saurenbach and W. Zinn, Phys. Rev. B **39**, 4828 (1989).

41. M. Julliere, Phys. Lett. **54A**, 225 (1975).

42. J.S. Moodera, Lisa R. Kinder, Terrilyn M. Wong and R. Meseryey, Phys. Rev. Lett. **74**, 3273 (1995).

43. M. Bowen, M. Bibes, A. Barthelemy, J.-P. Contour, A. Anane, Y. Lemaitre and A. Fert, Appl. Phys. Lett. **82**, 233 (2003).

44. P.M. Tedrow and R. Meservey, Phys. Rev. B **7**, 318 (1973).

45. G.A. Prinz, Phys. Today **48**, No.4, 58 (1995).

46. Z.W. Dong, R. Ramesh, T. Venkatesan, Mark Johnson, Z.Y. Chen, S.P. Pai, V. Talyansky, R.P. Sharma, R. Shreekala, C.J. Lobb and R.L. Greene, Appl. Phys. Lett. **71**, 1718 (1997).

47. Z.W. Dong, T. Boettcher, C-H. Chen, I. Takeuchi, M. Rajeswari, R.P. Sharma and T. Venkatesan, Appl. Phys. Lett. **69**, 3432 (1996).

48. T. Kimura, Y. Tomioka, H. Kuwahara, A. Asamitsu, M. Tamura and Y. Tokura, Science **274**, 1698 (1996).

49. V. A. Vas'ko, V. A. Larkin, P. A. Kraus, K. R. Nikolaev, D. E. Grupp, C. A. Nordman, and A. M. Goldman, Phys. Rev. Lett. **78**, 1134 (1997)

50. S.B. Ogale, V. Talyansky, C.H. Chen, R. Ramesh, R.L. Greene and T. Venkatesan, Phys. Rev. Lett. 77, 1159 (1996).

51. T. Zhao, S.B. Ogale, S.R. Shinde, R. Ramesh, R. Droopad, J. Yu, K. Eisenbeiser and J. Misewich, Appl. Phys. Lett. **84**, 750 (2004).

2.1 Synthesis methods

Various synthesis methods have been reported to synthesize good quality single phase compounds having desired physical properties. To synthesize polycrystalline bulk manganites, two main techniques are widely used namely, a) Solid State Reaction method and b) Chemical method. Solid State Reaction method involves the synthesis of bulk manganites at elevated temperatures while chemical method comprise of Sol-gel technique having different routes like nitrate and acetate, Co-precipitation, Citrate-gel method etc [1-3]. In the present course of work, Solid State Reaction method was used to synthesize all the polycrystalline single phase bulk manganites. The synthesis parameters such as sintering temperature & time, pressure applied at the time of palletizing the sample, grinding time etc were optimized to obtain single phase sample. Amongst all these parameters, final sintering can be considered as the most important parameter for good crystallization of sample.

Moreover, for the synthesis of manganite thin films several techniques have been used by researchers such as Pulsed Laser Deposition (PLD) technique, Chemical Solution Deposition (CSD) technique, Metal Oxide Chemical Vapour Deposition (MOCVD) technique, RF Sputtering, Spray Pyrolysis, Molecular beam epitaxy (MBE) and Atomic Layer Deposition (ALD). In the present work, PLD and CSD techniques have been used to synthesize single crystalline thin films of manganites.

2.1.1 Solid state method

Owing to the simplicity and easiness in its use all the bulk polycrystalline samples studied during the course of present work were synthesized using the solid state reaction method. The fig. 2.1 illustrates the consecutive steps involved in the solid state method for synthesizing various manganites.

The starting chemicals used to prepare manganites consist of high purity (> 99.9%) oxides and carbonates. They were pre-heated for proper time and temperature in order to remove moisture from them. Pre-heated powders were then weighed according to the required stoichiometry. After mixing of pre-heated powders, it is important to grind the powders thoroughly for an enough time to obtain homogeneous distribution of all the constituents. First heating known as calcinations is required to achieve phase formation

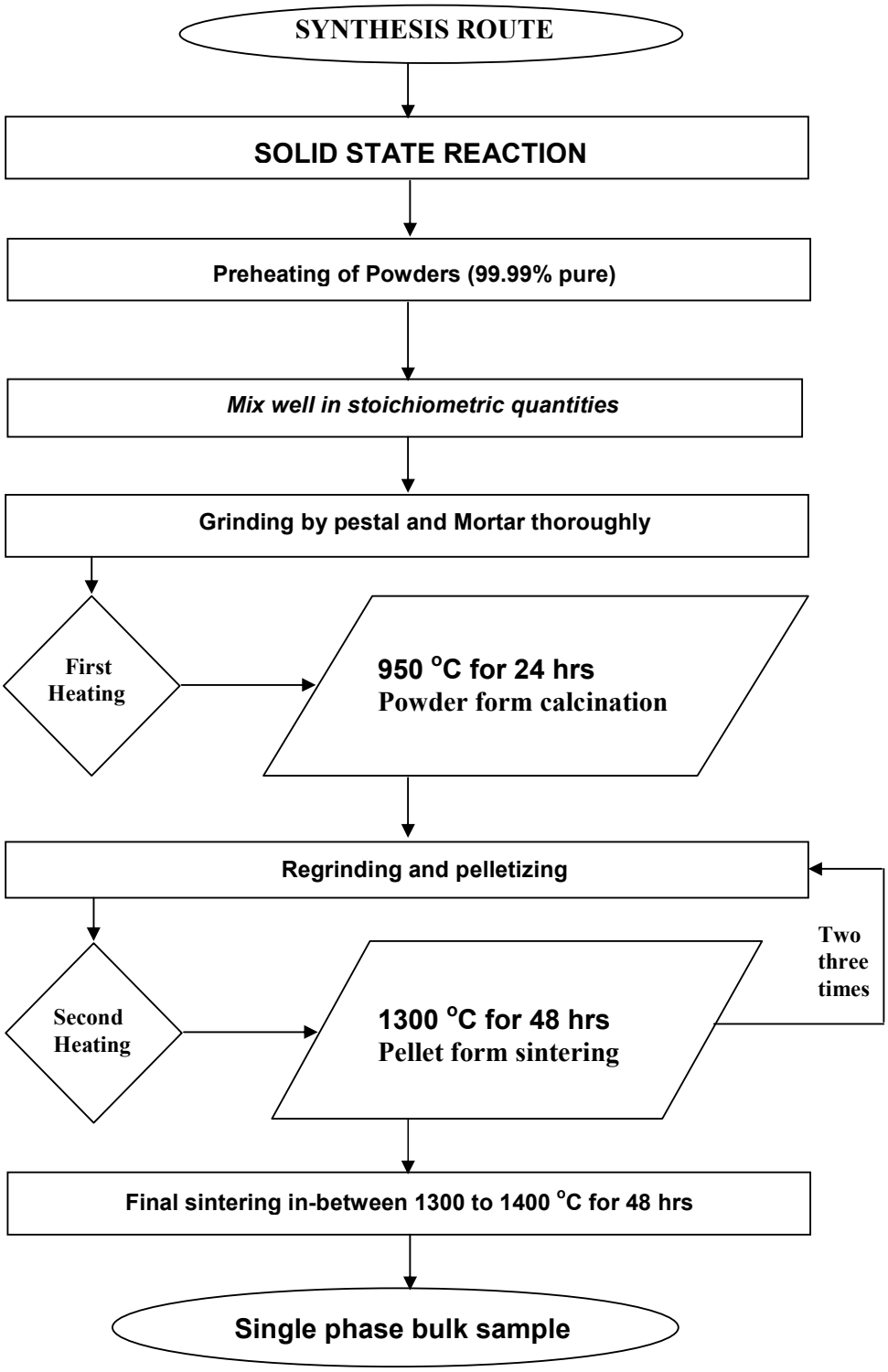

Figure 2.1 : Flow chart of Solid State method used.

and to remove CO_2 present in the sample. Moreover, before the final sintering of the sample, the number of intermediate heatings (sintering) are required in order to obtain a good structural phase formation and the crystalline nature of sample. For every intermediate sintering of the sample, fine black powder obtained after successive grinding was pressed into a cylindrical pellet by applying high pressure which infact improves the better inter-grain connectivity in the resultant bulk sample. After the final sintering, samples were allowed to natural cool down to room temperature.

The solid state reaction method is the simplest and most commonly used technique for synthesizing high-quality manganite polycrystalline bulk samples.

2.1.2 Chemical Solution Deposition (CSD) technique

The CSD method has a number of advantages over conventional methods of thin film deposition as it is a cost-effective, easier method which requires low reaction temperature and yields high quality thin films of desired thickness [4]. The use of CSD method requires a good knowledge of chemistry and chemical properties of various acetates and nitrates. The flow chart (Fig. 2.2) and general steps involved in CSD method for synthesizing thin films of CMR materials are described below -

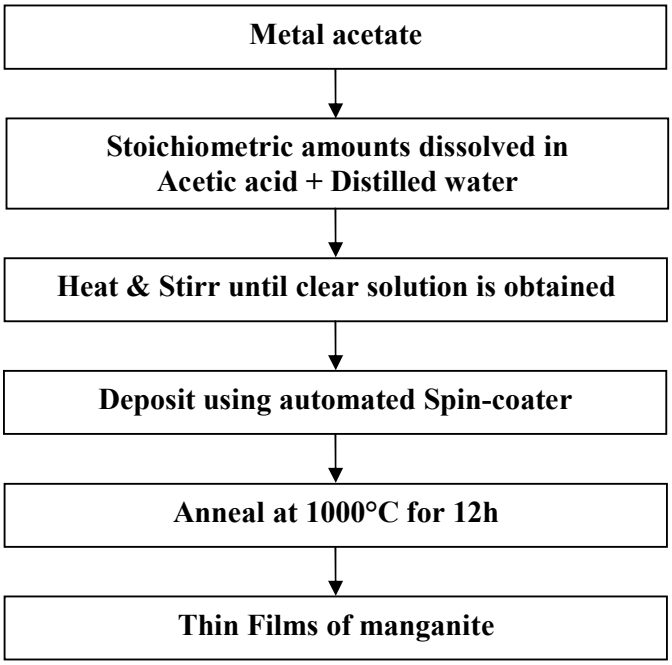

Figure 2.2 : Flow chart of CSD technique used.

In the CSD technique, the first step involved the preparation of precursor solutions which was utilized for depositing thin films on substrate using Spin-coating unit. For making precursor solution, stoichiometric powders of all constituents were taken, which were dissolved in an homogeneous mixture of acetic acid and distilled water at 80 °C. Precursor solution was then deposited on suitable substrates using Spin-coater unit at 6000 rpm for 25 secs. Films were kept at 120 °C for 20 min & then slow cooled to RT. The films were then heated at 350 °C for 30 min in the furnace to obtain more thicker films and the same process was repeated for 2-3 times. At the end, thin films were finally annealed at 1000 °C for 24 hours in the oxygen environment and finally cooled @ 2°C/min to RT.

2.1.3 Pulsed Laser Deposition (PLD) technique

The use of PLD technique for the deposition of thin films has its own advantages over other techniques such as RF Sputtering, Metal Oxide Chemical Vapor Deposition (MOCVD) or spray pyrolysis etc. The main advantage is the laser possesses narrow frequency bandwidth, coherence & high power density. Moreover the laser beam also has high energy density which in fact helps to vaporize even hardest materials [5, 6]. With the use of PLD technique, one can deposit very high quality thin films with precise control over the thickness of the film. But, the main disadvantage of the PLD techniques is small deposition area as well as higher operating cost.

The manganite thin films studied in the present course of work were synthesized by PLD method employing KrF excimer gas laser as well as Nd^{+3}:YAG solid state laser. The details of optimized conditions and parameters used for PLD method are given in the relevant chapters.

The mechanism of pulsed laser deposition for synthesis of thin films includes:

a) Interaction of the Laser beam with the target surface
b) Kinematics of the plasma plume ablated from the target
c) Deposition of plasma plume on the heated substrate
d) Growth of the thin film on the substrate

In the process of deposition, focused laser beam enters in the vacuum chamber via the quartz window. This focused laser beam strikes onto the surface of the target materials with short pulses and necessary high energy. Because of such a high energy, material is ejected out in the form of plasma plume from the target surface. In the last, ejected plasma plume is deposited onto the heated substrate. In general, ultraviolet laser radiation affects the target to the depth of ~ 100 nm. The composition of the deposited films is identical to that of the target materials.

In this process a pulsed laser beam vaporizes the surface of the target in an ultra high vacuum (UHV) and the vapor condenses on a substrate. Generally, such a process coats the surface with a pure film of the correct composition. Fig. 2.3 shows the schematic diagram of PLD chamber along with target carrousel, substrate holder, vacuum chamber, Quartz window etc.

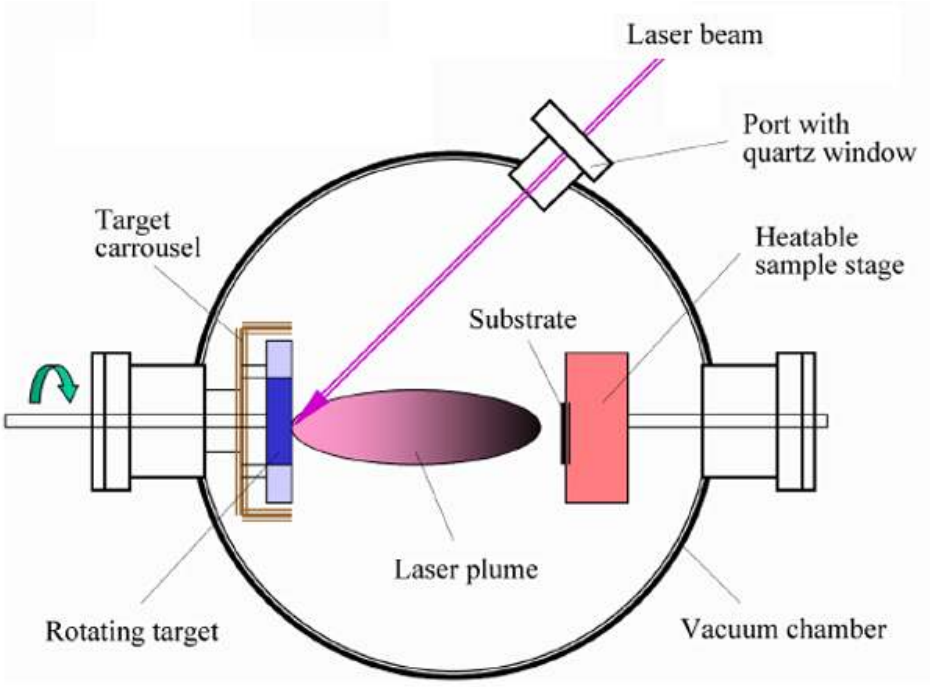

Figure 2.3 : A schematic representation of PLD apparatus.

Deposition Parameters

The Physical properties of the films deposited by PLD technique depends on the properties of target material and deposition parameters used at the time of deposition. Among which, for the target material, the density and the surface roughness are the crucial parameters which affect the quality of the film. Generally, the target should be dense enough and the surface roughness should be visually negligible. The deposition parameters that highly affect physical properties of thin films are -

a) Laser Energy

b) Substrate temperature

c) Substrate to target distance

d) Oxygen partial pressure (in case of manganites)

Laser energy density required to ablate target material is known as threshold energy. As the energy increases greater than threshold energy, the amount of ablated material will increase and also the kinetic energy of the ablated material. Ablated material with higher energy has its own advantage as well as disadvantage. Sometimes, this higher energy hits the already deposited material thus causing rearrangement of deposited material and also may have possibility of causing defects in the deposited films. The laser energy density can be calculated by measuring the Laser energy (E_{Laser}) and area of the Laser spot (A_{spot}):

Laser energy Density = E_{Laser} / A_{spot}

Substrate temperature is another important parameter. The energy of the heated substrate is transferred to the deposited atoms and thus provides enough energy for the deposited atom to find the best site for them on the substrate. This effect is just similar to the increasing energy of the ablated material. But, too high substrate temperature also results in diffusion between substrate and thin films while appropriate substrate temperature is most crucial in order to synthesize epitaxial thin films. The large substrate to target distance gives enough time for ablated material to collide with each other and form large particulates which results in poor quality of the deposited films. The impact of increase in oxygen pressure has the same effect as increase in substrate to target distance since it also increases time to reach the ablated material to substrate. The deposition of oxide (manganites) films in vacuum, results in oxygen deficient films which means

oxygen pressure is required to maintain the stoichiometry of the thin films, particularly oxide films.

Advantages and disadvantages of PLD

PLD technique has its own indistinguishable advantages over other methods for deposition of thin films such as -

a) The main advantage is that, the resultant film has same stoichiomtry as of the target material even for complicated materials.

b) The wide range of materials can be ablated.

c) The wide range of gas pressures can be used.

d) During deposition, target can easily be changed which helps to fabricate multilayers.

e) One laser can be used for more than one chamber.

In spite of such a good advantages of PLD technique, there are also some disadvantages of this technique such as -

a) Formation of large particulates during the deposition

b) Can be used for only small area deposition.

To overcome these problems, such as formation of large particulates during the deposition and limitation of deposition area, the efforts are underway and it is expected that problem will be overcome soon.

2.2 Structural and morphological studies

During the course of present work, for the structural characterization, X-ray diffraction (XRD) method has been used while to understand surface morphology of the thin films, Atomic Force Microscopy (AFM) technique have been used. XRD is a non-destructive technique which reveals information about the crystallographic structure, chemical composition and physical properties of materials either in the form of polycrystalline bulk or thin film. Thus, XRD characterization is necessary since it gives knowledge about the phase purity and single phasic nature of the sample. Moreover, in

case of thin films, it is necessary to observe the growth of film, surface roughness and the film continuity for which AFM technique has been used.

2.2.1 X-ray diffraction (XRD)

X-rays are electromagnetic radiation with typical energies in the range of 100 eV - 100 keV. For the purpose of XRD, only short wavelength X-rays ~ 1Å i.e. comparable with the size of inter-atomic distance are used. Since the wavelength of X-rays is of the order of 1Å, they are most ideal for probing the crystalline arrangement of atoms in the polycrystalline bulk as well as in the thin film forms. Generally, in the XRD facility, the Cu target is used, which emits 8 KeV X-rays with wavelength of 1.54Å. X-rays primarily interact with electrons in atoms. When X-ray photons collide with electrons, some photons from the incident beam will be deflected away from their original direction just like billiard ball. These are the X-rays that we measure in diffraction experiments, as the scattered X-rays carry information about the electron distribution in materials. Diffracted X-rays from different atoms can interfere with each other and the resultant intensity distribution is strongly modulated by this interaction. If the atoms are arranged in a periodic array, the diffracted waves will consist of sharp interference maxima (peaks) with the same symmetry as in the distribution of atoms. Measuring the diffraction pattern, therefore, allows us to deduce the distribution of atoms in a material [7].

The peaks in the XRD pattern are directly related to the inter-atomic distances i.e. cell parameter though other parameters will also affect the peak position. Let us consider an incident X-ray beam interacting with the atoms arranged in a periodic manner in the material as illustrated in fig. 2.4.

The horizontal line can be viewed as a set of planes in the crystalline material resulting from the periodic arrangement of atoms. For a given set of lattice planes with an inter-plane distance ‘d’, the condition for the occurrence of the diffraction (peak) can be written as,

$$2d \sin\theta = n\lambda$$

which is known as the Bragg's law.

In this equation, λ is the wavelength of the X-ray, θ is the scattering angle and n an integer representing the order of the diffraction peak. Mostly, the XRD data is

interpreted using the Bragg's Law. It is important to note that, we have assumed atoms in the crystal behaving as scattering points for the derivation of Bragg's law. This law can be applied to scattering centers consisting of any periodic distribution of electron density. In other words, the law holds true, if the atoms are replaced by molecules or collections of molecules, such as colloids, polymers, proteins and virus particles.

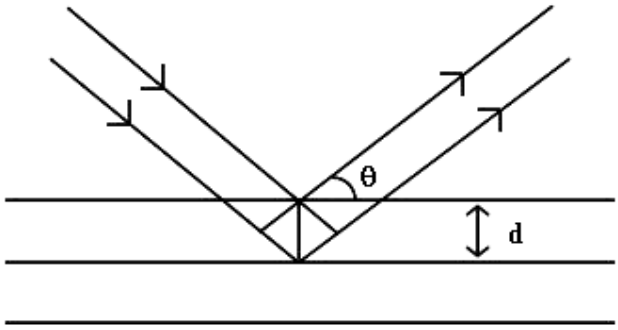

Figure 2.4 : A schematic diagram depicting the Bragg's law of X-ray diffraction.

Powder XRD is the most widely used X-ray diffraction technique for characterizing polycrystalline bulk materials [8, 9]. The term 'powder' really means that, the crystalline grains are randomly oriented in the material and the material is in the powder form, consisting of fine grains of single crystalline material to be studied. When the 2-D diffraction pattern is recorded, it shows concentric rings of scattering peaks corresponding to the various d spacings in the crystal lattice. The positions and the intensities of the peaks are used for identifying the structure of the material. The PowderX software is generally used to determine the value of the lattice parameters. The structural studies on the samples under present study were performed by XRD and data was analyzed using PowderX software. For more in-depth analysis of X-ray diffraction patterns, the Rietveld analysis was used.

2.2.2 High-resolution X-ray diffraction (HRXRD)

For the structural studies of thin film, High-resolution X-ray diffraction techniques is commonly used. HRXRD is not a specific technique but is rather a collection of XRD techniques used to characterize the thin film samples grown on different substrates. The high quality epitaxial thin films (nearly-perfect material) are necessary which are synthesized for the specific advanced device applications. Thus, to confirm the high quality and epitaxial nature of thin film, HRXRD is used.

Common HRXRD measurements performed on thin film samples include -

- Precise lattice constants

  These measurements derived from θ - 2θ scans, provide information about lattice mismatch between the film and the substrate from which one can calculate the strain and stress in the thin film emerging out due to difference in the lattice parameter of thin film and the substrate used.

- Rocking curve

  These measurements carried out by taking θ scan at a fixed 2θ angle, the width of which is inversely proportionally to the dislocation density in the film structure, are used as a measure of the quality of films.

- X-ray reflectivity

  Using this techniques, one can determine the thickness, roughness and density of the film. Generally, this technique has been used to characterize multilayer structures. Furthermore, this technique does not require crystalline film and also works with even amoprphous materials.

- Texture measurements

  Texture measurements are used to determine the orientation distribution of crystalline grains in the polycrystalline sample. One can see textured state of a material (generally in the form of thin films). A material is called as textured, if the grains are aligned in a preferred orientation along certain lattice planes. The texture measurements have

been performed on thin films at a fixed scattering angle and consists of a series of ϕ– scans (in-plane rotation around the center of the sample) at different chi-angle (ψ), as illustrated in the Fig. 2.5.

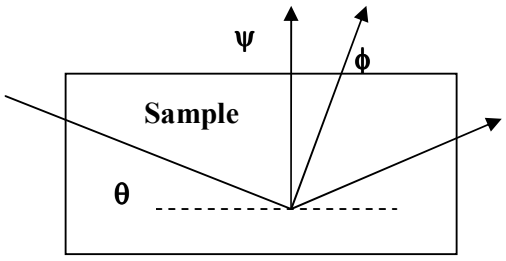

Figure 2.5 : A schematic diagram depicting the θ,ψ & ϕ angle for the XRD of thin films.

2.2.3 Atomic Force Microscopy (AFM)

Atomic Force Microscopy (AFM) is a characterization technique used to study the surface morphology of conducting or non-conducting materials either in the form of solid or liquid. AFM is a very high-resolution type of scanning probe microscope with resolution ~ fraction of nanometer. The AFM was invented by Binnig, Quate and Gerber in 1986 and is one of the advanced tools for carrying out surface morphology at the nanoscale. The AFM consists of a cantilever with a sharp tip (probe) at its end point that is used to scan the surface of the sample (generally, in thin film forms). The cantilever is commonly Silicon or Aluminium tip. When the tip end point is brought into proximity of a sample surface, forces between the tip and the sample lead to a deflection of the cantilever. Typical forces measured in AFM include mechanical contact force, Van der Waals forces, Capillary forces, chemical bonding, electrostatic forces, magnetic forces (in case of magnetic force microscopy), etc. The deflection is measured using laser spot reflected from the top of the cantilever into the position sensitive detector (PSD). These cantilevers are fabricated with piezoresistive elements that gauge the strain on the cantilever. If the tip were scanned at a constant height, there would be a risk that the tip would collide with the surface, causing damage. Hence, in most cases, a feedback

mechanism is employed to adjust the tip to sample distance to maintain a constant force between the tip and the surface of the sample.

The image recorded showing the presence of humps and valleys on the surface, resembles a surface topographic map. Also, it should be kept in mind that, image recorded is only the representation of surface and not an optical image of surface of sample. Basically, there are three modes used for AFM: (a) Contact mode (b) Non-contact mode and (c) Tapping mode. Fig. 2.6 shows the schematic representation of all the three modes of AFM operation.

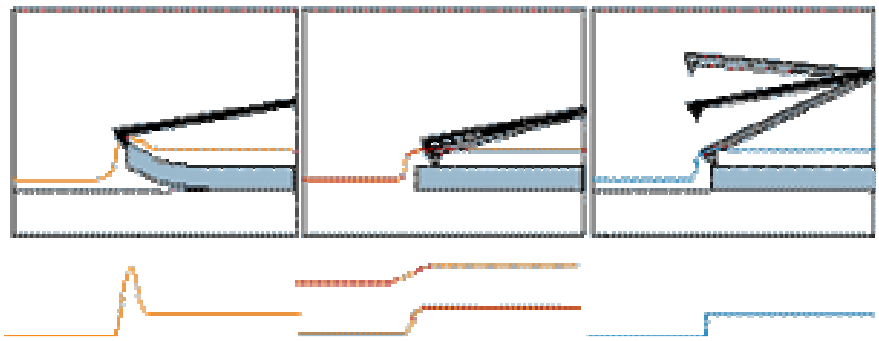

Figure 2.6 : Schematic diagram of tip-sample in Contact mode (left), Non-contact (NC) mode (middle) and Tapping mode (right) AFM.

Contact mode

In the contact mode, the tip scaning the sample is in close contact with the surface. The force on the tip is repulsive. This force is set by pushing the cantilever against the sample surface with a piezoelectric positioning element. In contact mode AFM, the deflection of the cantilever is sensed and compared to some desired value of deflection. If the measured deflection is different from the desired value then, the voltage applied by the piezo to raise or lower the sample relative to the cantilever is sufficient to maintain the desire value of deflection. The voltage applied to the piezo is a measure of the height on the sample surface. There are also some drawbacks of this mode. At the time of scanning, the continuous contact of the cantilever on the surface of the sample ultimately damage the surface and also can modify the resulting image as well as property of the material.

Non-contact mode

To overcome the drawbacks of the contact mode, the non-contact (NC) mode AFM was developed by Martin et al in 1987 [10]. In NC-AFM mode, the cantilever is intentionally vibrated by a piezo-electric modulator with small amplitude at a fixed frequency that is near the intrinsic resonant frequency of the cantilever. As the tip approaches the sample, the van der Waals attractive force between the tip and the sample acts upon the cantilever and causes changes in both the amplitude and phase of the cantilever vibration. These changes are used by the z-servo system to control the tip-sample distance (typically few nm). It is important to maintain the tip-sample distance. Therefore, a very high performing z-servo system is required for NC-AFM.

Tapping mode

In NC-AFM, if the z-servo performance is not sufficiently good, the tip will regularly stick to the sample, which generates glitches on the AFM image. In order to solve this problem, Zhong et al introduced a tapping mode in which the tip makes contact with the sample at every vibration cycle but detaches from the sample surface by using a large vibration amplitude [11]. The tapping mode eliminates the lateral friction force but the tip-sample impact force is greater than that used in typical contact mode AFM. This will result in significant tip and sample wear.

But, now-a-days new advances in AFM technology (such as high performance z-servo system) have made NC-AFM superior to tapping mode in every way. Fig. 2.7 shows the steep contour of a polymer sphere that has a diameter of about 5 μm. This image is not possible using tapping mode but NC-AFM mode makes it possible.

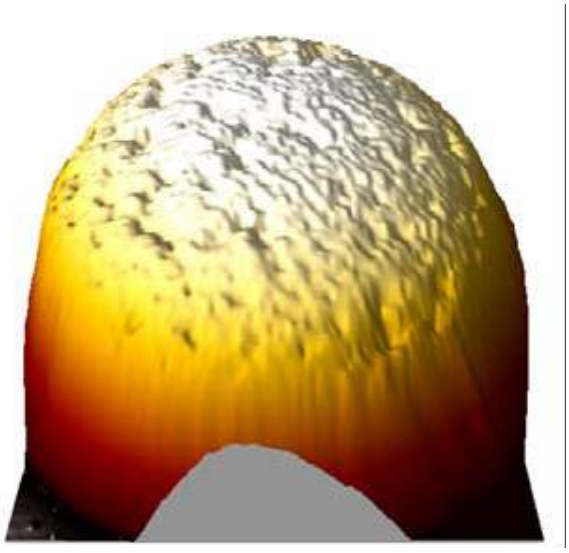

Figure 2.7 : NC-AFM image of a polymer sphere (6×6μm).

2.3 Electrical and magnetotransport studies

The knowledge about the electrical properties of the bulk materials, thin films and artificial devices is essential in determining their applicability and usefulness. The resistivity must be measured accurately since its value is critical from application point of view. The samples in the present thesis work were characterized for their electrical and magneto transport properties by the D.C. four-probe resistivity technique as described below.

2.3.1 D.C. four-probe resistivity

D.C. four-probe resistivity method is the standard and accurate technique to measure the transport properties. The schematic diagram for the technique used is as shown in fig. 2.8. This geometry is used for the measurement of resistivity of specimens having wide verities of shapes. In it usual form, the four probes are collinear. Current flows between the outer pair contacts and the potential across the inner pair is measured.

A low contact resistance is one of the necessary things to measure the transport properties since the sample possesses very low resistance. Standard four-probe method is the technique which provides low contact resistance at the time of measurement [12]. For

the transport and magnetotransport measurement purpose, the samples were cut in a rectangular bar shape using a diamond cutter. In order to make the ohmic contacts between electrical probe and the sample surface, silver epoxy paint was used. Very fine paste of the silver paint was made by dissolving it in the appropriate amount of n-butyl acetate (thinner). This very fine paste of silver was applied on the ends of four leads and the sample surface. The advantage of using four wires to attach the sample is, it reduces the contribution of the leads and joints to the resistance measurements. The sample and four leads were kept onto a sample holder and the wires were connected with leads to the measuring instruments. This sample holder is known as resistivity puck (fig. 2.9) while resistivity was measured using a Physical Property Measurement System (PPMS). The samples were cooled down to the lowest temperature (~ 1.4K) by using liquefied He^3. The samples were heated by using a heater and the resistance was measured as a function of temperature in the wide temperature range.

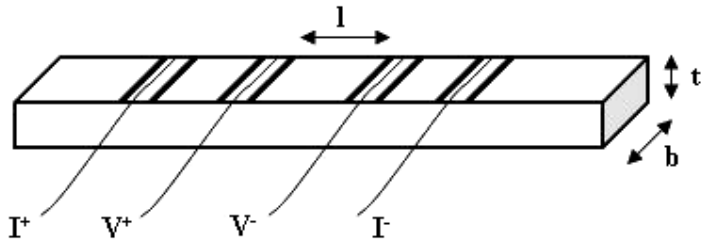

Figure 2.8 : Four probe contacts on the sample for current and voltage leads.

In the course of present work, the ρ - T measurements on manganite bulk and thin films, having very low resistance, have been carried out which requires very precise current source and sensitive voltmeter. A fully automatic resistivity measurement set up with multiple sample facility available at UGC-DAE CSR, Indore, operable in the temperature range 4.2K – 300K was used. Fig. 2.9 shows the diagram of resistivity sample holder having current and voltage probe contacts on each sample. The sample specimen resistivity can be calculated using formula

$$\rho = R\frac{A}{l}$$

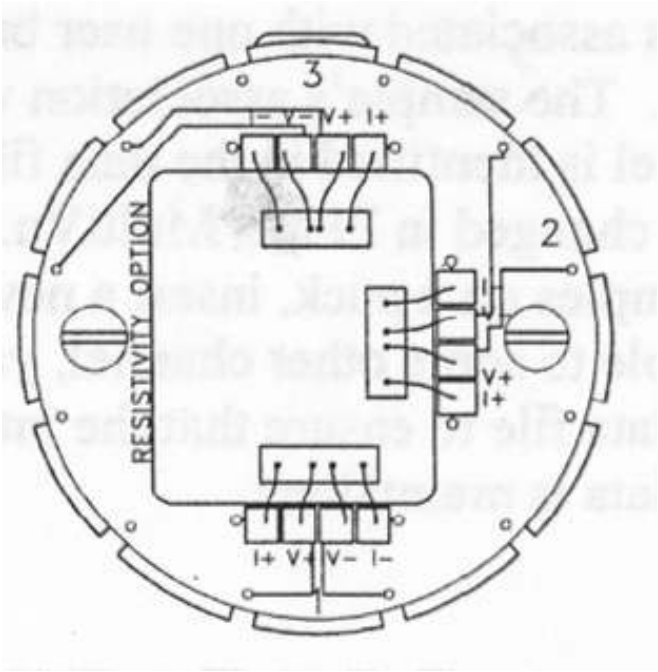

Figure 2.9 : Diagram of resistivity puck with three samples.

where A is the cross-sectional area of the sample (b x t) and l is the shortest distance between the two voltage leads.

In order to study the magnetoresistive properties of the samples, d.c. four probe resistivity measurements were carried out without and with the magnetic field applied either parallel or perpendicular to the sample surface. In general, for the purpose of magneto R-T, the full resistivity data as a function of temperature were collected in the temperature range of 5K - RT with and without applied magnetic field. While for obtaining MR vs H isotherm, resistivity was measured as a function of applied magnetic field till the resistivity becomes almost constant at a particular constant temperature.

2.3.2 I-V characteristics

Since last few years the efforts have been made on the fabrication of devices based on manganite thin films and multilayers, having potential applications. To understand the transport behavior of such single crystalline and polycrystalline thin film and devices, I-V characteristics emerge as a most comprehensive tool. In manganite materials, it is interesting to study the temperature dependent I-V behaviour to know the

temperature dependent modifications in band gap. Some reports on I-V characteristics i.e. the creation of an artificial grain boundaries on the thin film structures by depositing the manganite films on the bi-crystal substrates suggest that, the transport properties of the film can not be fully explained by tunnelling across grain boundary [13]. R.Gunnarsson et al [14] have demonstrated the model for spin-polarized transport through artificial grain boundary created by bi-crystal substrates which correlates the magnetoresistance value with the potential barrier at the grain boundary. Neeraj Khare et al [15] have investigated the conduction through an artificial grain boundary junction made in LBMO thin film with optimal doping. In all the above mentioned reports, researchers have fitted the I-V characteristics curves in two different laws 1) Simple power law and 2) Simmon's model. Simple power law can be described as $I \alpha V^n$ where n is depends on temperature and field and from the value of n one can predict which kind of transport mechanism is responsible for conduction. $n \sim 0.5$ is expected in a disordered metal with e-e interaction [16], $n \sim 1.0$ is expected for strongly correlated metallic oxide systems [17] while, $n \sim 2.33$ indicates quasiparticle tunneling via pairs of localized states [18]. Further, the Simmon's model is given by $G \alpha a + b*V^n$, where a is the zero-bias conductance at a particular temperature, b is the co-efficient which depends on potential barrier and n is the constant whose value can predict the kind of electrical transport mechanism. The values of $n \geq 0.6$, indicates tunnelling through disordered metallic oxides [19], while $n = 4/3$ indicates quasiparticle tunnelling via pairs of localized states [20]. If $n > 1.4$, it indicates for Spin-flip Scattering at the grain boundary [21] and $n = 2$ predicts the direct tunnelling of charge carriers [16].

During the present work, the I-V behaviour of the manganite thin film heterostructures & p-n junction diodes was studied using the d.c. four probe method by varying the applied current and observing the variation in voltage generated at various temperatures. The I-V curves of bi-layered p-n junctions studied show good rectifying behavior and also exhibit large positive MR near to RT. The effect of thickness & carrier density of p-type layer on magneto I-V characteristics has been also studied. In all the p-n junction devices studied, at particular temperature the value of MR changes from positive to negative. There is possibility that the new results obtained will help to understand the strongly correlated electron engineering which includes switching of rich functionality such as ferromagnetism, superconductivity and more and will lead to new

control methods for electric/magnetic phases in the transition metal oxides and in novel functional optical, magnetic, and electrical devices.

REFERENCES

1. E. M. Engler, Chem. Technol. **17** (1987) 542.
2. S.X. Dou, H.K. Liu, A.J. Bourdillon, J.P. Zhou, N.X. Tan, X.Y. Sun, C.C. Sorrell, J. Am. Ceram. Soc., **71C**, 329 (1998).
3. C.J. Brinkered and G.W. Scherer, "Sol-Gel Science" Academic Press Inc, Boston (1990).
4. Ulrich Hasenkox, Carsten Mitze and Rainer Waser, J. Am. Ceram. Soc. **80(10)**, 2709 (1997).
5. S.P. Gapanov, B.M. Luskin, N.N. Salaschenko, Sov. Tech. Phys. Lett. **5**, 210 (1979).
6. S.P. Gapanov, A. Gudkov, A.A. Fraerman, Sov. Tech. Phys. Lett. **27**, 1130 (1982).
7. B.D. Culity, "X-Ray Diffraction", Addison-Wesly Pub. Co. Inc. (1978).
8. A.R. West, Solid State Chemistry and its Applications, John Wiley & Sons, Chichester (1984).
9. http://www.mrl.ucsb.edu/mrl/centralfacilities/xray/xray-basics/index.html
10. Y. Martin, C.C. Williams, H.K. Wick-ramasinghe, J. Appl. Phys. **61**, 4723 (1987).
11. Q. Zhong, D. Innis, K. Kjoller, V.B. Elings, Surf. Sci. Lett. **290**, 1688 (1993).
12. L. J. Vanderpauw, Philips Res. Repts. **16**, 187 (1961).
13. M.G. Blamire, C.W. Schneider, G. Hammerl & J. Mannhart, Appl. Phys. Lett. **82**, 2670 (2003).
14. R. Gunnarsson, A. Kadigrobov & Z. Ivanov, Phys. Rev. B **66**, 024404 (2002).
15. Neeraj Khare, U.P. Moharil, A.K. Gupta, A.K. Raychaudhury, S.P. Pai and R. Pinto, Appl. Phys. Lett. **81**, 325 (2002).
16. L. Bokacheva, W. Teizer, F. Hellman & R.C. Dynes, Phys. Rev. B **69**, 235111 (2004).
17. A.K. Raychaudhuri, K.P. Rajeev, H. Srikanth and N. Gayathri, Phys. Rev. B **51**, 7421 (1995).

18. M. Ziese, S. Sena, C. Shearwood, H.J. Blythe, M.R.J. Gibbs and G.A. Gehring, Phys. Rev. B **57**, 2963 (1997).

19. J.G. Simmons, J. Appl. Phys. **34**, 1793 (1963).

20. A.K. Raychaudhury, Adv. Phys. **44**, 21 (1995).

21. L.I. Glazman & A.K. Matveev, Sov. Phys. JEPT 67, 1276 (1998) ; Zh. Eksp. Teo. Fiz, **94**, 332 (1988).

After the discovery of MR in manganites, a large MR had been observed at RT in $La_{0.67}Ba_{0.33}MnO_3$ (LBMO) manganite thin films while in the annealed films of $La_{0.67}Ca_{0.33}MnO_3$ (LCMO), the three orders of magnitude increase in MR was reported at 77K [1, 2].

After achieving appreciable field sensitivity in manganite thin films, the attention is now focused on observing large tunneling magnetoresistance (TMR) in the multilayered thin film devices for suitable applications such as read/write heads, magnetic random access memories (MRAM) etc. For the use of any TMR device, it should possess high field sensitivity as well as higher operating temperature. The TMR device usually contains a multilayer structure with non-magnetic layer sandwiched between the top and bottom magnetic electrodes [manganites]. Such device exhibit high field sensitivity useful for device application but due to existence of non-magnetic barrier between two ferromagnetic layers, its operating temperature becomes lower. There are several reports on the improvement of MR by selecting different materials for multilayered structure [3-5]. First serious attempt towards fabrication of manganite based devices lead to the fabrication of trilayered device consisting of one insulating layer sandwiched between two manganite layers. The epitaxial trilayer junction device in the form of [(top electrode) $La_{0.67}Sr_{0.33}MnO_3$] / (insulating layer) $SrTiO_3$ / [(bottom electrode) $La_{0.67}Sr_{0.33}MnO_3$] was fabricated which showed a large MR ~ 83% at 4.2 K under small applied field [3]. In order to fabricate TMR device, Markna et al had deposited thin Al_2O_3 in the form of islands instead of layer which was sandwiched between two ferromagnetic $La_{0.5}Pr_{0.2}Sr_{0.3}MnO_3$ (LPSMO) layers [4]. Although this device exhibit MR ~ 77% at ~ 220K, its operating temperature is quite low as compared to LPSMO thin film (297K). This may be due to insulating nature of sandwiched layer, which causes detrimental interface states reducing TMR through insulating layer and hence MR at higher temperature.

Keeping in mind the above mentioned interesting results and constraints on the use of manganite based devices, in this chapter, the results on the studies on manganite based multilayered structure have been given. Using the well studied bulk targets of $La_{0.5}Pr_{0.2}Ba_{0.3}MnO_3$ (LPBMO) and $La_{0.5}Pr_{0.2}Sr_{0.3}MnO_3$ (LPSMO) synthesized using Solid State Reaction method, nine layered multilayered device with the combination of LPSMO {5} / LPBMO {4} thin film layers on single crystalline $LaAlO_3$ (LAO), $SrTiO_3$ (STO) and

$NdGaO_3$ (NGO) substrates, were grown using PLD technique. Our earlier studies suggest that, LPSMO is ferromagnetic metallic at RT while LPBMO is paramagnetic insulator at room temperature (RT) [6, 7]. Therefore, instead of using insulating non-magnetic layer between two ferromagnetic layers [6], we have used LPBMO magnetic layer sandwiched between two LPSMO layers to avoid large lattice mismatch and defects at the interface. This was done with an aim to enhance the MR at RT.

In addition, in this chapter, the results of the studies on the transport and magnetotransport measurements in current in plane (CIP) and current perpendicular to plane (CPP) modes on the multilayer device grown on LAO substrates have been given. These studies were carried out to study the effect of different geometry on transport behavior of multilayer.

3.1 Synthesis of LPS-LPB manganite multilayer

The well characterized LPSMO and LPBMO targets (10 mm dia.) were used for the deposition of consecutive layers of LPSMO and LPBMO to fabricate nine layered nanostructured manganite multilayer device. Third harmonic (355 nm) of a Q-switched Nd-YAG laser was used for the fabrication of multilayered device using Pulsed Laser Deposition (PLD) technique. The parameters used for the deposition are given in the table below

Table 3.1 : Thin film deposition parameters

Laser used	Nd - YAG
Targets	LPSMO & LPBMO; Polycrystalline bulk
Substrates	$LaAlO_3$, $SrTiO_3$ & $NdGaO_3$; Single crystalline (1 0 0)
Laser energy	~ 2 J/cm^2
Repetition rate	10 Hz
Substrate temperature	650 – 700 °C
Oxygen partial pressure	400 mTorr

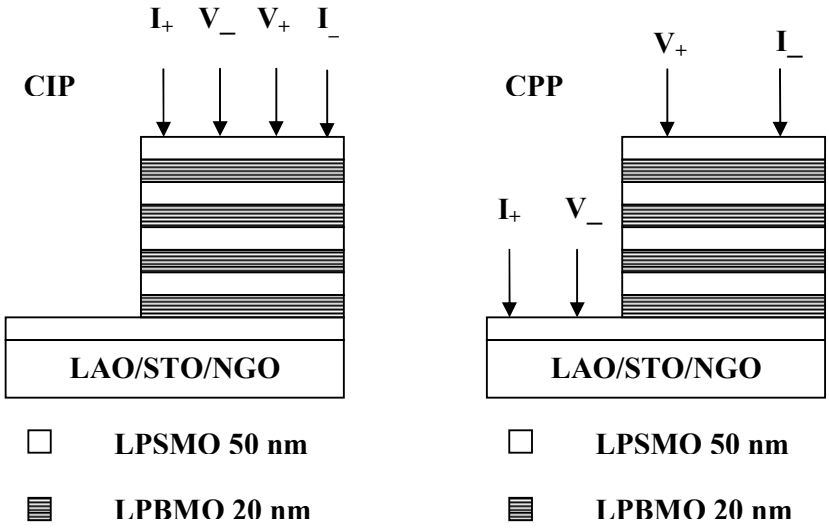

Figure 3.1 : Schematic diagram of multilayer device.

Fig.1 shows the schematic diagrams of multilayer devices grown on different substrate and CIP and CPP modes used for the transport measurements. The estimated thickness of the deposited LPSMO & LPBMO layer were 50 nm & 20 nm, respectively. The lateral dimensions of the device under study are 10 mm^2 X 2.4 mm^2. The transport and magnetotransport measurements have been carried out in both CIP & CPP mode.

3.2 Structural studies

Figs. 3.2 & 3.3 show rietveld fitted XRD patterns of bulk LPSMO and LPBMO samples respectively, used for the deposition of multilayer devices on various substrates. The XRD patterns of the bulk LPBMO & LPSMO samples reveal their single phasic nature crystallizing in distorted orthorhombic structure (Space group P_{nma}, No. 62). The lattice parameter values determined from rietveld fitted XRD are; a = 5.512(2) Å, b = 7.791(2) Å and c = 5.548(2) Å and a = 5.552(2) Å, b = 7.752(2) Å and c = 5.481(2) Å for LPBMO & LPSMO bulk samples, respectively.

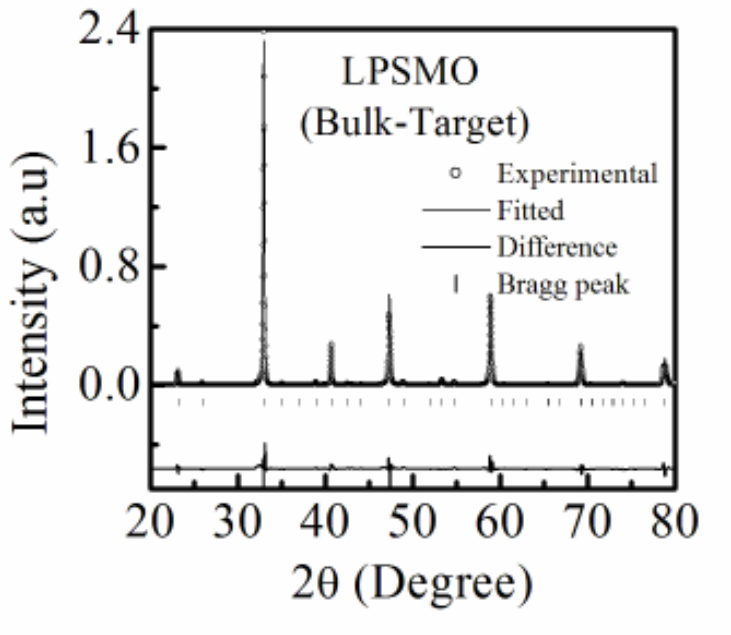

Figure 3.2 : Rietveld fitted XRD pattern of LPSMO bulk sample.

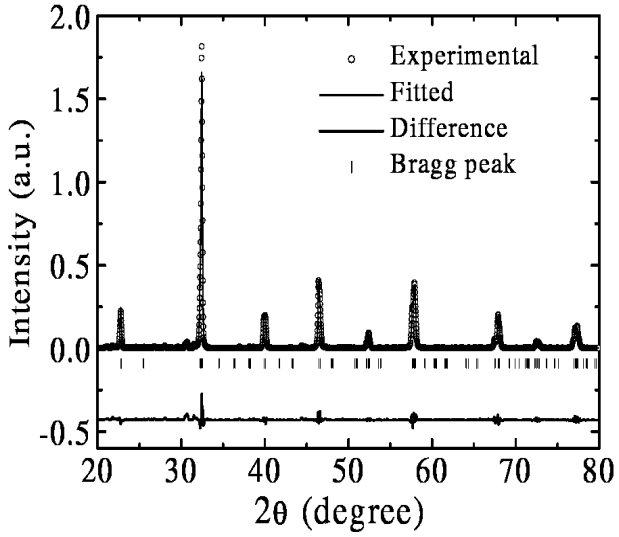

Figure 3.3 : Rietveld fitted XRD pattern of LPBMO bulk sample.

Structural characterization was carried out on all the multilayer device by analyzing the XRD patterns obtained. X-ray diffraction patterns of multilayer device grown on LAO, STO and NGO substrates are shown in figs 3.4 (a), (b) & (c), respectively. It can be seen from the figures that, all the three multilayers exhibit only the *(0 0 l)*

reflections, suggesting the heteroepitaxial growth of the multilayer. The influence of substrate strain (heteroepitaxial) is the main factor distinguishing manganite multilayer from bulk manganite samples.

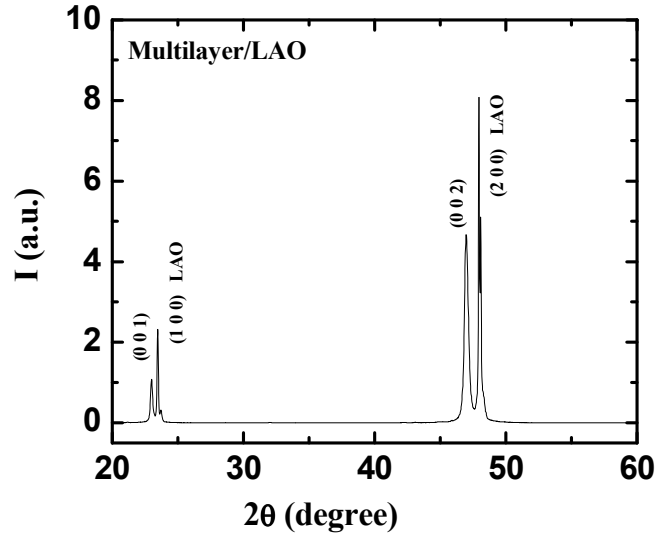

Figure 3.4 a) : XRD pattern of multilayer grown on LAO substrate.

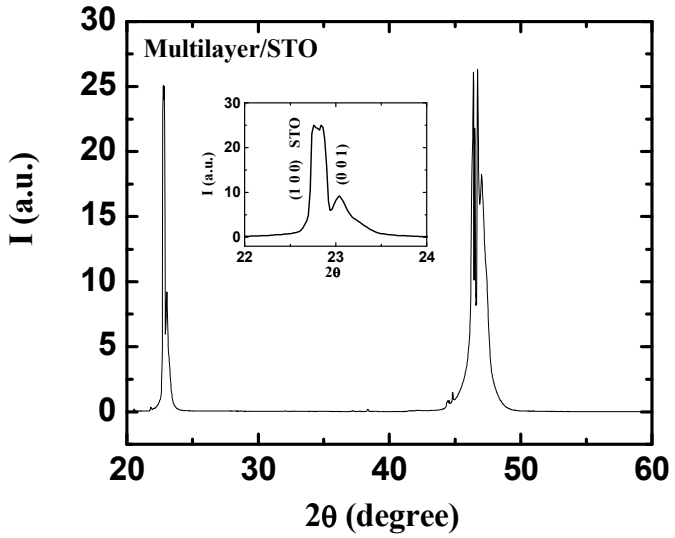

Figure 3.4 b) : XRD pattern of multilayer grown on STO substrate. Inset of the figure shows the enlarged view of (0 0 1) peak.

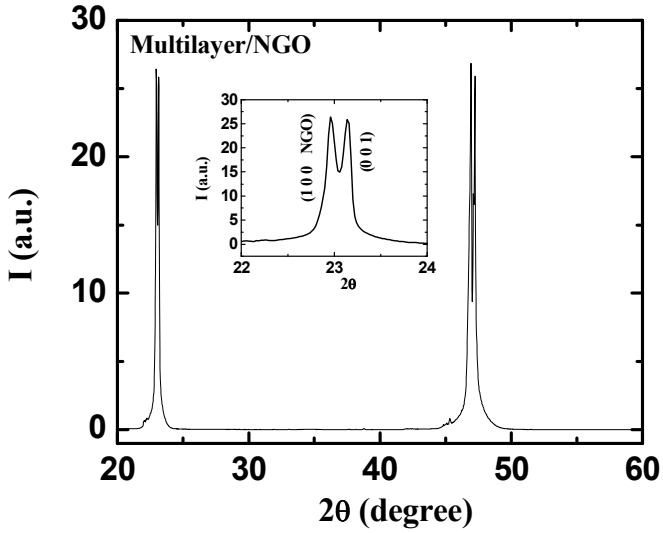

Figure 3.4 c) : XRD pattern of multilayer grown on NGO substrate. Inset of the figure shows the enlarged view of (0 0 1) peak.

3.3 Surface morphological studies

The surface morphology of all the multilayer device was studied using the AFM measurements. Fig. 3.5 a) shows the 2D AFM image of bottom LPSMO layer of multilayer on LAO substrate while Fig. 3.5 b) shows 3D image of the same. Fig. 3.6 a) shows the 2D AFM image of top LPSMO layer of multilayer on LAO substrates while fig. 3.6 b) shows 3D image of the same. It can be seen from these figures that, bottom LPSMO layer possess more island like growth as compared to upper LPSMO layer of multilayer. Fig. 3.7 a) & Fig. 3.8 a) shows 2D AFM pictures of multilayer grown on STO and NGO substrates while the fig. 3.7 b) & fig. 3.8 b) shows 3D AFM pictures of both the multilayers. The average grain size calculated are ~ 85 nm and ~ 40 nm for the multilayer grown on STO and NGO, respectively. It is also seen that, out of the two multilayers, multilayer on NGO possess pronounced island growth in the grain structure as compared to STO. It is reported that, island growth leads to highly non-uniform distribution of strain in the structure which may be responsible for the enhanced resistance and hence MR at RT [8].

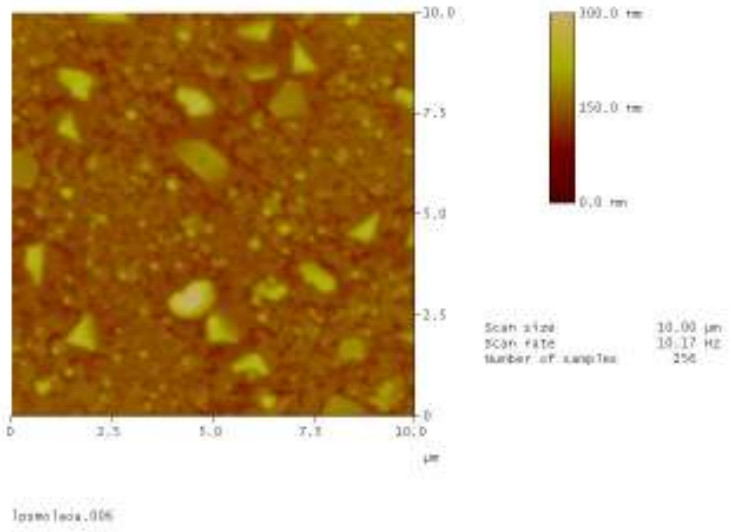

Figure 3.5 a) : 2D AFM image of bottom LPSMO layer for the multilayer grown on LAO substrate

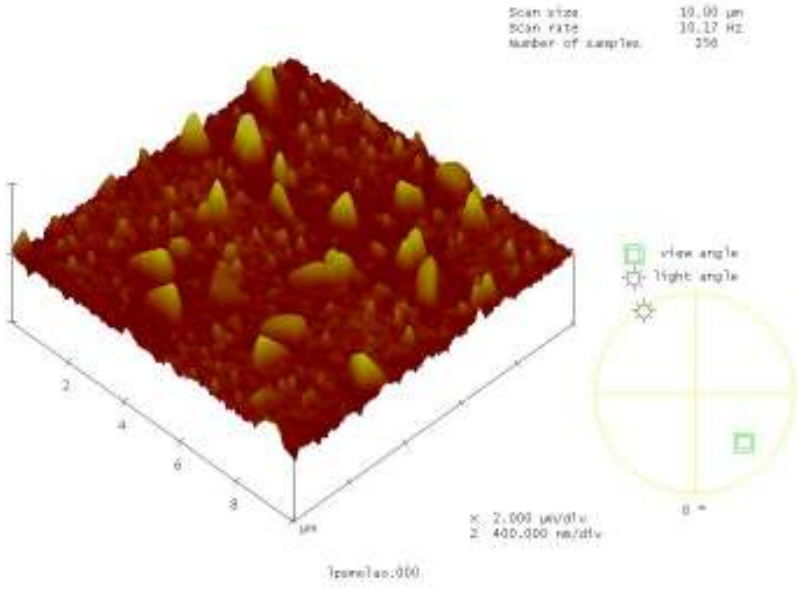

Figure 3.5 b) : 3D AFM image of bottom LPSMO layer for the multilayer grown on LAO substrate

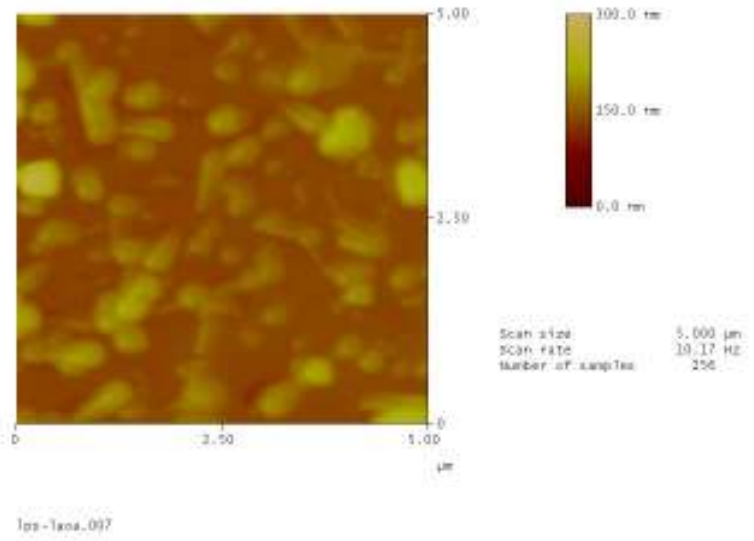

Figure 3.6 a) : 2D AFM image of top LPSMO layer for the multilayer grown on LAO substrate

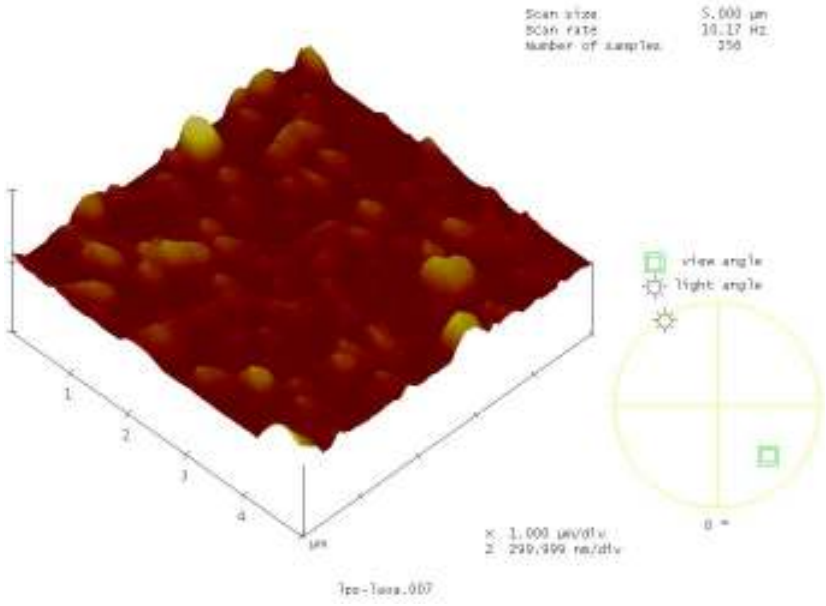

Figure 3.6 b) : 3D AFM image of top LPSMO layer for the multilayer grown on LAO substrate

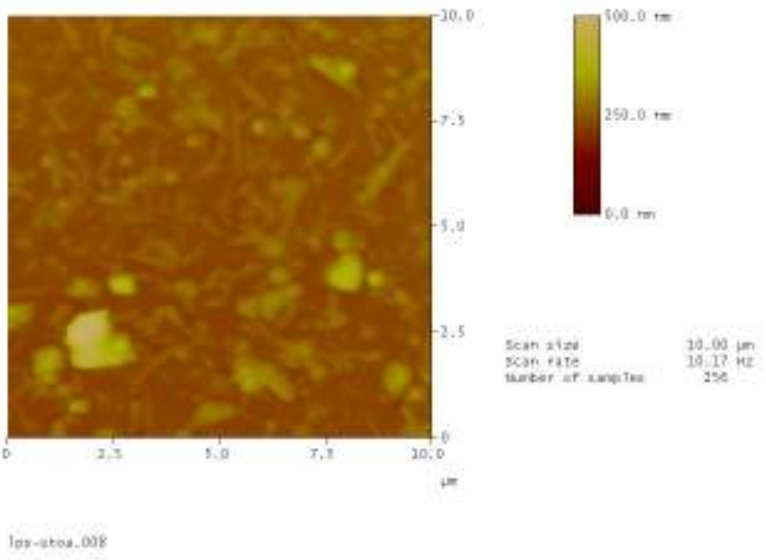

Figure 3.7 a) : 2D AFM image of the multilayer grown on STO substrate

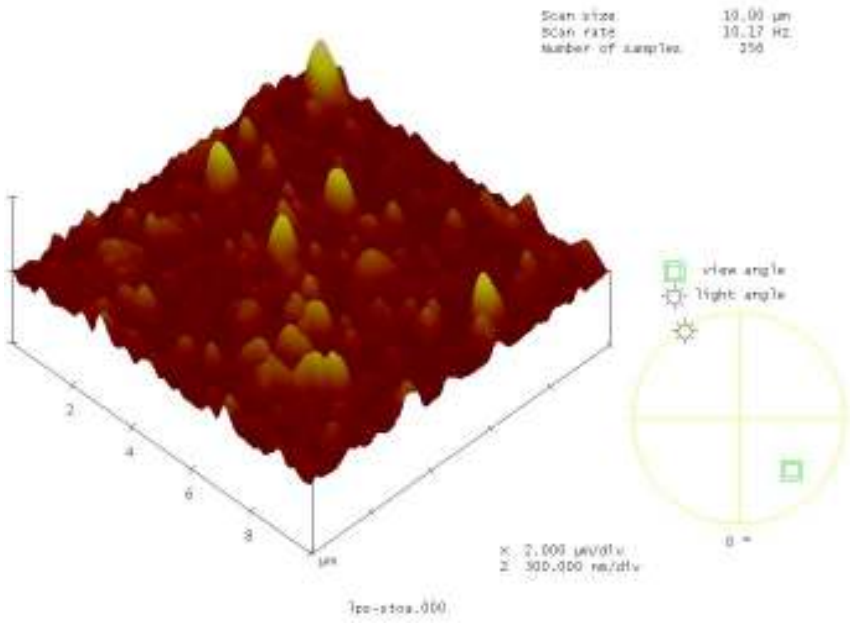

Figure 3.7 b) : 3D AFM image of the multilayer grown on STO substrate

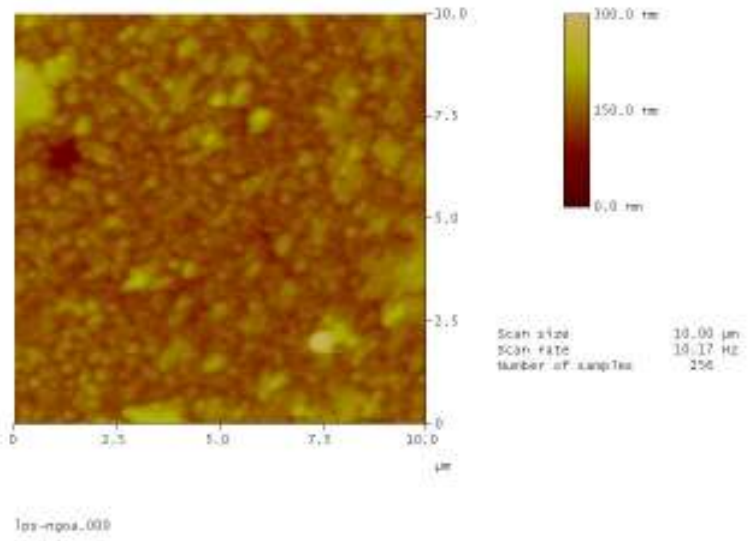

Figure 3.8 a) : 2D AFM image of the multilayer grown on NGO substrate

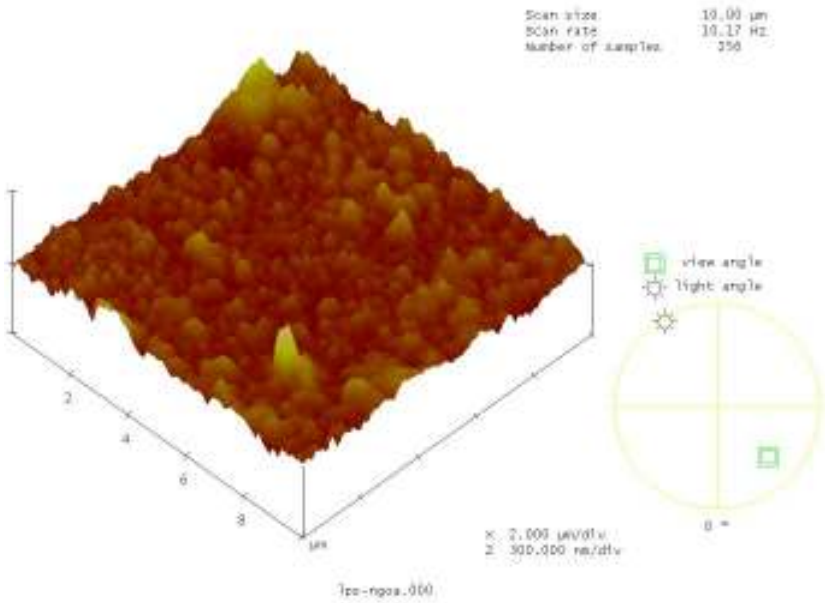

Figure 3.8 b) : 3D AFM image of the multilayer grown on NGO substrate

3.4 Transport studies

The transport measurements, on the multilayer devices grown on different substrates have been carried out using standard d.c. four-probe technique with and without applied magnetic field.

3.4.1 R-T measurements

Figs. 3.9 a) & b) show resistance versus temperature plots of the nine layered multilayer devices grown on LAO substrates in CIP and CPP mode respectively with applied magnetic field of 0T, 5T & 8T. It can be seen from the figures that, in both CIP and CPP modes, multilayer device do not show insulator to metal (I-M) transition up to 300K and resistance increases with increase in temperature. At 300K, the resistance of multilayer device is ~ 0.52 KΩ and 1.1 KΩ in 0T for CIP and CPP modes, respectively. With the application of magnetic field the large change in resistance is observed in both the modes.

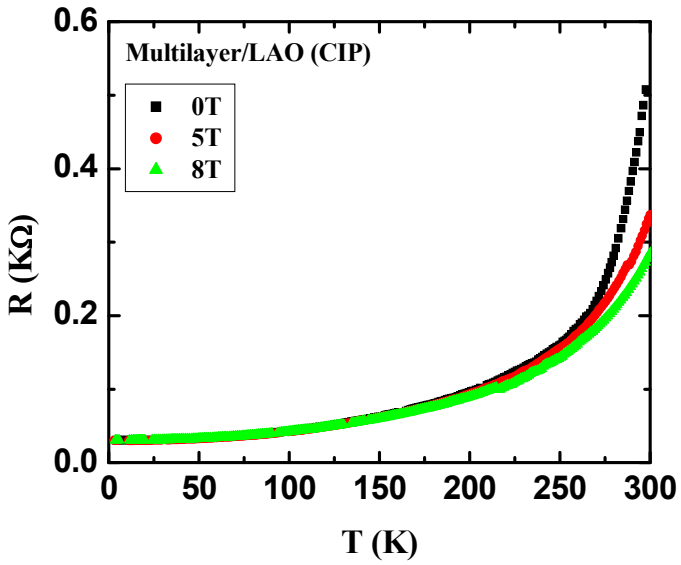

Figure 3.9 a): Resistance vs. temperature plot for multilayer grown on LAO substrate with applied magnetic field of 0T, 5T & 8T (in CIP mode).

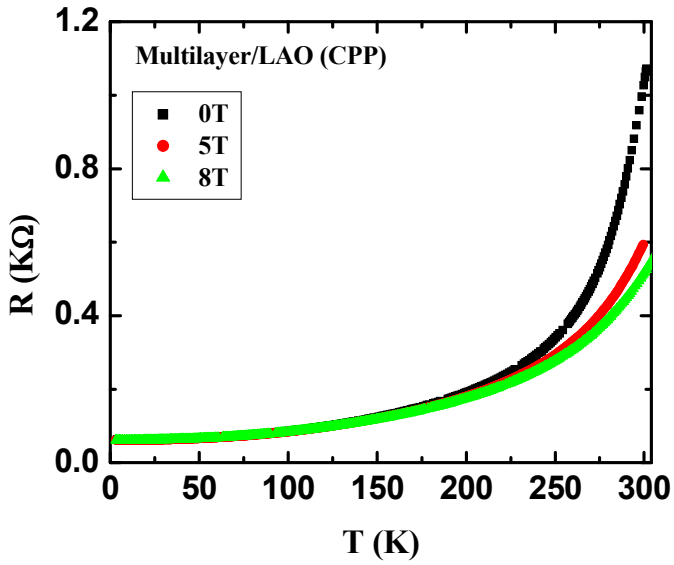

Figure 3.9 b) : Resistance vs. temperature plot for multilayer grown on LAO substrate with applied magnetic field of 0T, 5T & 8T (in CPP mode).

Figure 3.10 shows temperature dependence of resistance for the multilayers on STO and NGO substrates in CPP mode. The multilayer grown on STO do not show any I-M transition up to 300K whereas multilayer on NGO shows signature of I-M transition at 300K. At 300K, the resistance of a multilayer is ~ 0.45 KΩ and ~ 0.70 KΩ on the STO and NGO, respectively. The overall low resistance of multilayer on STO with respect to multilayer on NGO is possibly due to large strain induced by the NGO substrate as compared to STO. With the application of magnetic field the expected large drop in resistance is observed for both the multilayers.

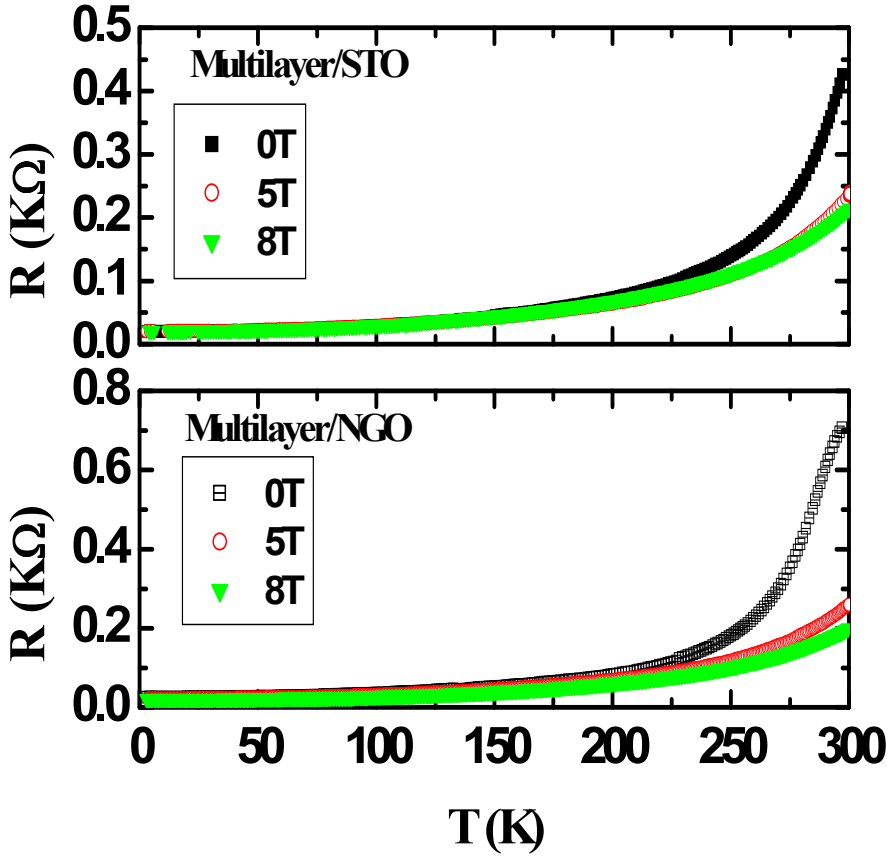

Figure 3.10 : Resistance vs. temperature plot for multilayer grown on STO & NGO substrate with applied magnetic field of 0T, 5T & 8T (in CPP mode).

Figure 3.11 show current-voltage (I-V) characteristics of multilayer device grown on LAO substrate in CPP mode at 90K & 300K. I-V measurements on multilayer device have been carried out, to understand whether the conduction through all the nine layers of device (in CPP mode) is due to the tunneling through insulating LPBMO layer or not. It can be seen from figure that, I-V characteristics exhibit linear (ohmic) behavior for both temperatures which suggest that tunneling mechanism is not responsible for conduction in multilayer device in CPP mode.

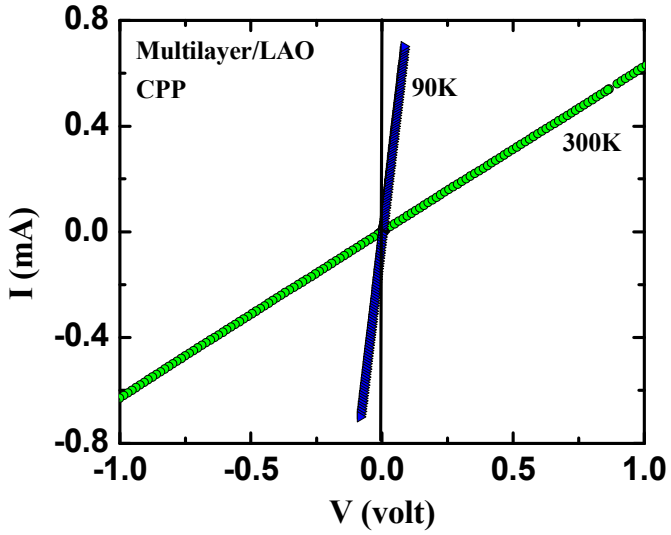

Figure 3.11 : I-V characteristics of multilayer on LAO substrate in CPP mode at 90K & 300K.

3.4.2 TCR studies

To further evaluate the application potential of the manganite multilayer device grown, the temperature dependent resistance sensitivity studies were carried out to determine the parameter known as temperature co-efficient of resistance (TCR) defined by,

$$TCR(\%) = \frac{1}{R}\frac{dR}{dT} \times 100K^{-1}$$

The higher value of TCR and operating temperature is very useful for uncooled or moderately cooled infrared imaging (bolometric) applications.

Fig. 3.12 show TCR% versus temperature plots for multilayer devices on LAO, in CIP and CPP modes. The maximum TCR values observed are ~ 3% and ~ 2.75% at 300K in CIP and CPP mode, respectively. Fig. 3.13 shows TCR% versus temperature plot for multilayer device on STO and NGO substrate in CPP mode. The maximum TCR values observed are ~ 3.15% and ~ 2.77% near 300K for multilayers on STO & NGO, respectively.

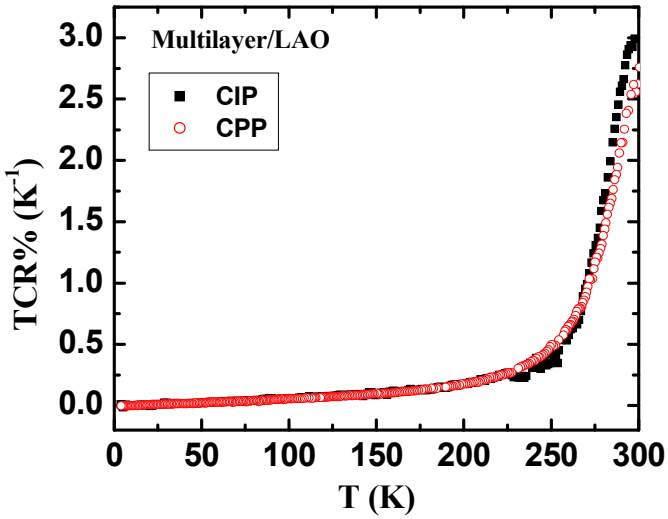

Figure 3.12 : TCR% vs. temperature plot for multilayer grown on LAO substrate in CIP and CPP mode.

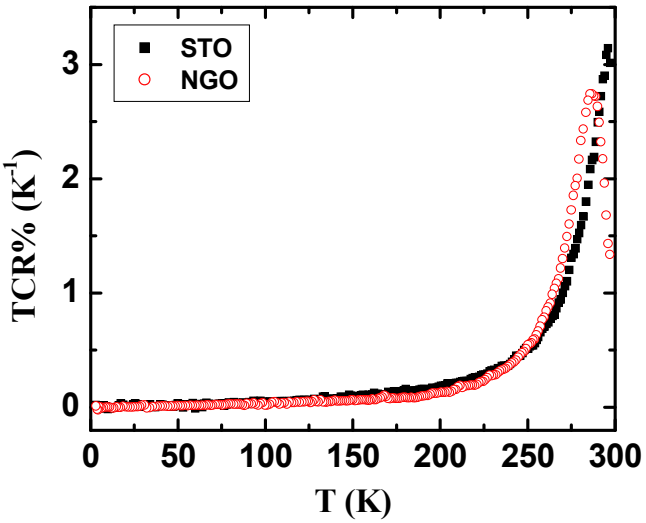

Figure 3.13 : TCR% vs. temperature plot for multilayer grown on STO & NGO substrate in CPP mode.

3.5 Magnetotransport studies

The magnetotransport measurements on the manganite device on LAO, STO and NGO substrates have been carried out up to applied magnetic field of 8T, at various temperatures to study the field sensing properties of device.

3.5.1 Magnetoresistance

In the multilayer device, magnetoresistance (MR%) is calculated as MR % = $(\rho_0 - \rho_H)/\rho_0 \times 100$ %, where ρ_H and ρ_0 are the resistances with and without fields. Fig. 3.14 shows the MR versus H isotherms for the multilayer on LAO at 5K, 100K, 150K and 300K in an applied magnetic field up to 8T in CIP and CPP modes. It can be seen from the figures that, multilayer exhibits large MR ~ 60% and ~ 50% at 300K in CIP and CPP mode, respectively which suggests that there is not much difference in the MR values in both the modes at RT. Moreover, below room temperature (5K, 100K & 150K), the maximum MR value exhibited is ~ 5-6% in the CIP and CPP modes which is in contradiction with the results on multilayer device having non magnetic Al_2O_3 barrier between two manganite electrodes [4].

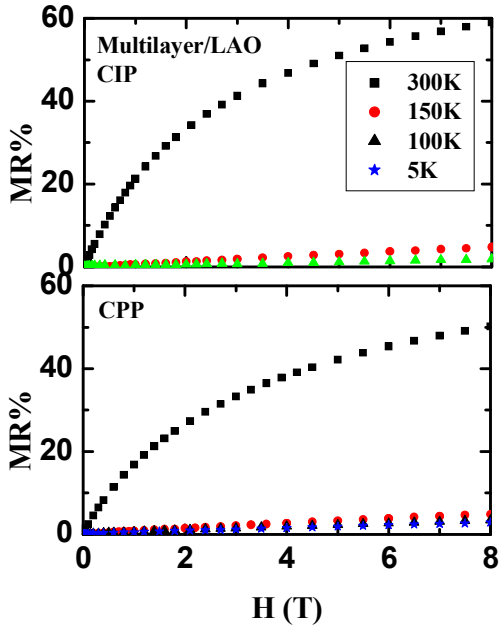

Figure 3.14 : Isotherm MR vs. H plot for multilayer on LAO substrate in CIP & CPP mode at different temperatures.

Figure 3.15 shows the MR versus H isotherms for the multilayers grown on STO and NGO substrates at 5K, 100K, 150K and 300K in CPP mode with applied magnetic field up to 8T. It can be seen from the figure that, large MR ~ 56% and 61% at 300K is exhibited by multilayers on STO and NGO, respectively. It can be also seen that, at 150K the MR values are ~ 5.3% and 7.7% which becomes ~ 1.4% and 2.1% at 5K for the multilayer on STO and NGO, respectively. This shows that, there is no effect of substrate on MR at low temperature. However, the effect of substrate on the MR at RT is due to the non-uniform strain distribution in multilayer on NGO, as evident from AFM studies [fig. 3.8 (a & (b]. Our earlier study on the $La_{0.7}Ba_{0.3}MnO_3$ (LBMO) manganite thin film on LAO substrate supports this view [9]. This result is also confirmed by transport property data which shows lower value of resistivity in the multilayer on STO substrate.

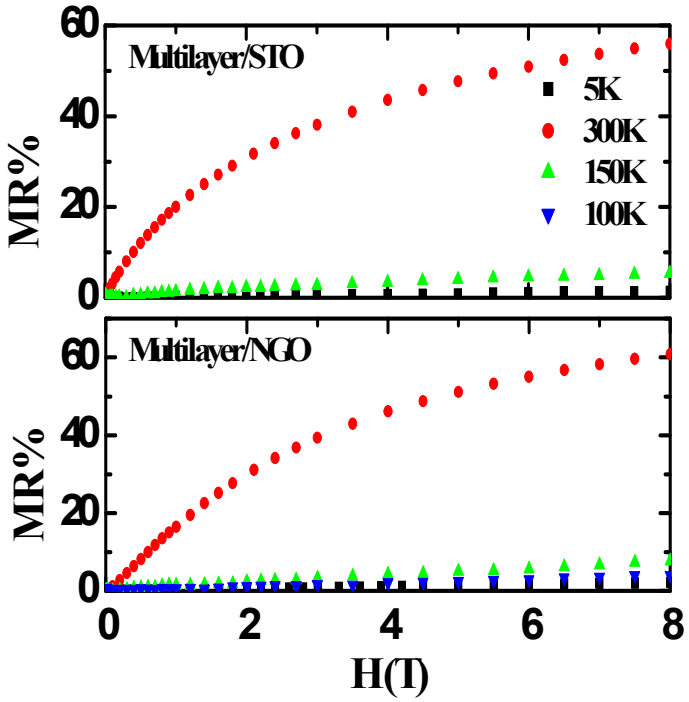

Figure 3.15 : Isotherm MR vs. H plot for multilayer on STO & NGO substrates in CPP mode at different temperatures.

Figure 3.16 shows MR versus temperature plots for the multilayer grown on LAO substrates in CIP & CPP modes under 8T field. There is not much difference observed in

MR value. Similarly, fig. 3.17 shows MR versus temperature plots for multilayers on STO and NGO substrates in CPP mode under 8T field. It can be seen from the figures that, multilayer on NGO exhibits higher MR values as compared to for multilayer on STO substrate.

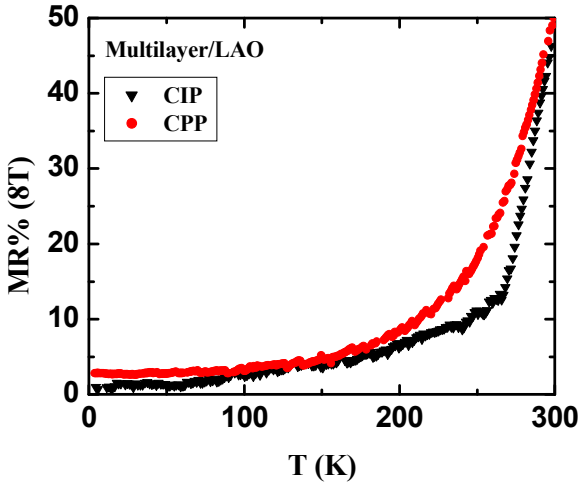

Figure 3.16 : MR vs. temperature plot for multilayer on LAO substrate in CIP & CPP mode under 8T magnetic field.

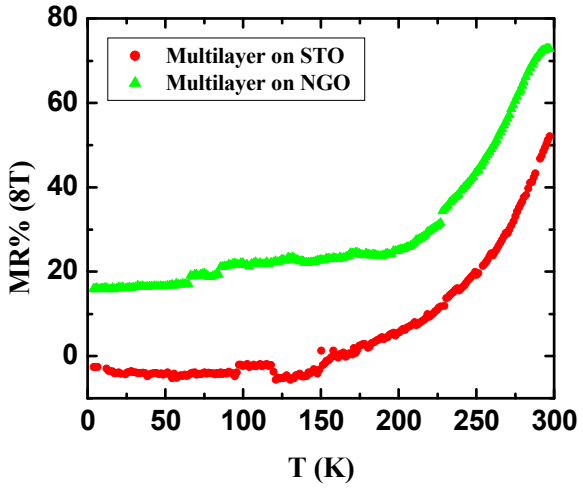

Figure 3.17 : MR vs. temperature plot for multilayer on STO & NGO substrates in CPP mode under 8T magnetic field.

3.5.2 FCR studies

The magnetic field sensing parameter quantified by the parameter known as FCR (field co-efficient of resistance) which is important for field sensing applications has been calculated for the manganite multilayers under study using the relation,

$$FCR(\%) = \frac{1}{R}\frac{dR}{dH} \times 100\, T^{-1}$$

Figure 3.18 shows FCR versus H plots for multilayer on LAO substrates at 300K in CIP and CPP mode. The maximum FCR value observed is ~ -29% at 300K in CIP mode whereas in CPP mode, FCR ~ -24% is observed. Figure 3.19 shows FCR versus H plots for multilayer grown on STO and NGO substrates at 300K in CPP mode. The maximum FCR value observed is ~ -35% at 300K for the multilayer grown on STO which decreases to ~ -18% for multilayer on NGO substrate. This large field sensitivity (-35%) at RT observed in multilayer grown on STO substrate makes it a proper material for the use in field sensing applications.

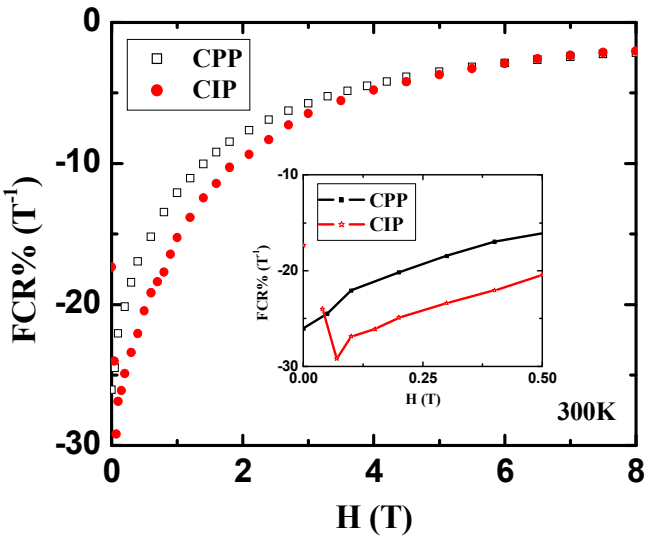

Figure 3.18 : Plot of FCR vs. H for multilayer on LAO substrate at 300K in CIP & CPP modes.

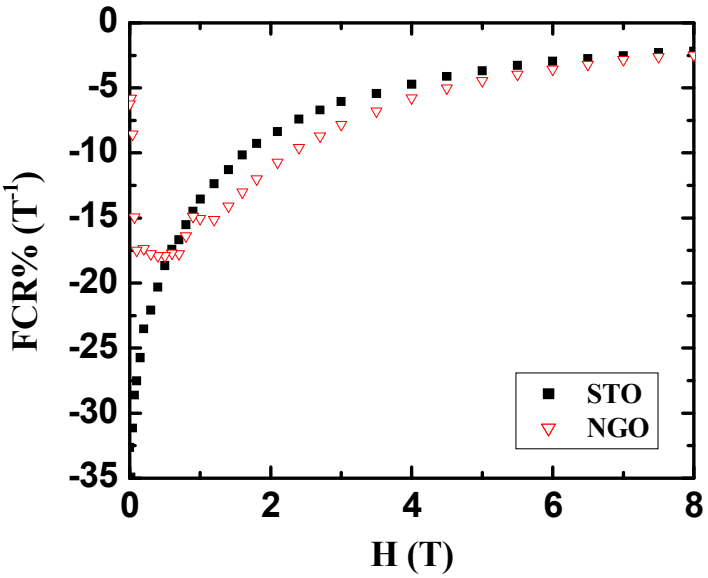

Figure 3.19 : Plot of FCR vs. H for multilayer on STO & NGO substrates at 300K in CPP modes.

3.6 Summary and conclusions

In this chapter, the fabrication of nine layered manganite and the results on the multilayer device of the type LPSMO {5} / LPBMO {4} on various substrates (LAO, STO & NGO) and the results on the studies on their structural, surface morphological, transport and magnetotransport properties have been presented with an aim to explore the possibility of use of these multilayers for temperature and field sensing applications.

Also, the results on the geometry dependent (in CIP & CPP mode) magnetotransport measurements on one multilayer device grown on LAO have been given in this chapter.

The reason for the observation of large MR at RT which leads to improved field sensitivity at high temperature in the LPSMO/LPBMO multilayer can be explained as follows –

At low temperature, observed MR values are quit low in both the modes of transport measurements i.e. CIP and in CPP mode. This can be understood as, in CIP

mode current passess through the upper LPSMO layer which is single crystalline in nature and hence do not possess extrinsic MR at low temperature. Moreover, in ferromagnetic metallic state (FMM) the contribution of intrinsic MR is less. In CPP mode, current passes from top LPSMO layer to bottom LPSMO layer via LPBMO and LPSMO consecutive layers. At low temperature, all the nine layers are in complete ferromagnetic state with no tunneling like conventional TMR. Hence, the MR exhibited is low.

At high temperature (RT), the multilayer under study, exhibits MR ~ 60% and 50%, in CIP and CPP modes, respectively. As current passes through large number of interfaces in CPP mode, it causes spin dependent scattering at the interfaces and moreover at RT, LPBMO is in paramagnetic insulating (PI) state which results in an increase in resistance and reduction in MR as compared to CIP mode. To understand large MR (~60%) in CIP mode, the calculated values of lattice mismatch for LPBMO and LPSMO are ~ -3.14% and -2.93%, respectively. It is reported that, compressive strain leading to tetragonal distortion (like Jahn-Teller distortion) results in the tendency of the e_g electrons to become localized [10]. The multilayer studied possess relatively less lattice compressive strain (~ -2.06%) as compared to LPBMO & LPSMO films, due to its large thickness (~320 nm). The reduction in strain can also be justified from AFM images of top and bottom LPSMO layers of multilayer structure (Figs. 3.5 & 3.6). It can be seen from the figures that, the bottom LPSMO layer possess more island like growth (characteristic of large strain) as compared to top LPSMO layer of the multilayer. Hence, due to the presence of less compressive strain (~2.06%), the e_g electron becomes more itinerant in the multilayer under study leading to large MR at RT. The observation of large MR (~60%) in CIP mode and field and temperature sensitivity (FCR ~ -29%, TCR ~ 3%) at RT in CIP mode can be attributed to the reduction in compressive strain due to the large thickness of multilayer.

We have also carried out substrate dependent magnetotransport studies on multilayer devices grown on STO & NGO substrates. It is observed that, the multilayer grown on STO substrate exhibits higher field and temperature sensitivity as compared to multilayer grown on NGO substrate. In addition, both the multilayers show MR around RT as compared to LPSMO thin film. The underlying cause for this may be as follows – the T_{IM} of LPSMO is ~ 305K while of LPBMO ~ 210K. In the temperature range of 210K-305K, the LPBMO layer is paramagnetic insulator (PMI) while LPSMO is in

ferromagnetic metallic state. Hence, in this temperature range, various possibilities for the conduction between FM-PMI-FM interfaces can be considered such as tunneling of charge carriers through insulating sandwiched LPBMO layer. To confirm the nature of tunneling, the I-V measurements have been carried out at two different temperatures i.e. 90K & 300K (fig. 3.11) which shows linear nature (ohmic) of I-V curve which rules out the possibility of tunneling mechanism for conduction. Also, as the thickness of sandwiched LPBMO layer is sufficiently large (~ 20nm), the conduction due to tunneling process is not possible. Also, the conduction at interfaces between LPSMO and LPBMO may cause spin flip scattering of charge carriers at interfaces thereby resulting in the reduction of net spin polarization and hence large MR exhibited by multilayer. Moreover, the multilayer on NGO possess large MR at RT which may be attributed to the non-uniform strain distribution resulting due to island growth. At temperature lower than 210K, the LPBMO also becomes FM due to which LPSMO-LPBMO (FM-PMI) interface becomes defect free (magnetic-magnetic) and exhibit low MR.

In summary, in the present work, the studies on PLD grown LPSMO {5} / LPBMO {4} multilayer grown on LAO, STO & NGO substrates exhibiting large field and temperature sensitivity at RT have been successfully carried out. In CIP mode, due to the presence of less compressive strain, the field sensitivity is improved which can be attributed to the large thickness of the multilayer under study. Moreover, the lower field sensitivity in the case of multilayer grown on NGO substrate can be attributed to the non-uniform strain distribution emerging due to island grain growth.

References

1) R. Von Helmolt, J. Wecker, B. Holzapfel, L. Schultz and K. Samwer, Phys. Rev. Lett. **71**, 2331 (1993).

2) Ken-ichi Chahara, Toshiyuki Ohno, Masahiro Kasal and Yuzoo Kozono Appl. Phys. Lett. **63**, 1990 (1993).

3) Yu Lu, X.W. Li, G.Q. Gong, Gang Xiao, A. Gupta, P. Lecoeur, J.Z. Sun, Y.Y. Wang and V.P. Dravid Phys. Rev. B **54**, R8357 (1996).

4) J.H. Markna, P.S. Vachhani, R.N. Parmar, P. Misra, B.N. Singh, L.M. Kukreja, D.S. Rana, S.K. Mailk and D.G. Kuberkar Europhys. Lett. **79**, 17005 (2007).

5) J.Z. Sun, L. Krusin-Elbaum, P.R. Duncombe, A. Gupta and R.B. Laibowitz, Appl. Phys. Lett. **70**, 1769 (1997).

6) J.H. Markna, R.N. Parmar, D.S. Rana, Ravi Kumar, P. Misra, L.M. Kukreja, S.K. Malik and D.G. Kuberkar Nucl. Instrum. Methods Phys. Res. B **256**, 693 (2007).

7) D.S. Rana, J.H. Markna, R.N. Parmar, P. Raychaudhuri, J. John, S.K. Malik and D.G. Kuberkar Phys. Rev. B **71**, 212404 (2005).

8) F. Tsui, M.C. Smoak, T.K. Nath and C.B. Eom Appl. Phys. Lett. **76**, 2421 (2000).

9) P.S. Vachhani, P.S. Solanki, J.H. Markna, R.N. Parmar, J.A. Bhalodia and D.G. Kuberkar Indian J. Eng. Mater. Sci. **14**, 163 (2007).

10) J. Klein, J.B. Philipp, G. Carbone, A. Vigliante, L. Alff and R. Gross, Phys. Rev. B **66**, 052414 (2002).

4.1 Synthesis of $La_{0.8-x}Pr_{0.2}Sr_xMnO_3$ /$SrNb_{0.2}Ti_{0.8}O_3$ bi-layered device

Divalent alkali metal doped rare earth manganites have attracted the attention of researchers since the discovery of colossal magnetoresistance (CMR) [1]. The practical applications of CMR effect in manganites demand the exhibition of significant MR% {MR% = $(R_0 - R_H)*100/R_0$} in low applied magnetic fields at or around room temperature (RT). Based on the possibility of observing large MR in artificial device based on tunneling, the first attempt to fabricate the magnetic tunnel junction $La_{0.7}Sr_{0.3}MnO_3$ (LSMO)/ $SrTiO_3$ / $La_{0.7}Sr_{0.3}MnO_3$ (LSMO) resulted in the MR ~ 83% at 5K [2]. Recently, our group has reported a MR ~ 77% in $La_{0.5}Pr_{0.2}Sr_{0.3}MnO_3$ / Al_2O_3 / $La_{0.5}Pr_{0.2}Sr_{0.3}MnO_3$ heterostructure at 200K [3]. H. Tanaka et al reported the electric field dependent modulation in double exchange around room temperature and temperature dependent I-V characteristics in the $La_{0.9}Ba_{0.1}MnO_3$ (LBMO) / SNTO p-n junction [4]. Such a junction exhibits good rectifying properties and asymmetric diode like I-V behavior. The effect of magnetic field on I-V characteristics of $La_{0.32}Pr_{0.35}Ca_{0.33}MnO_3$ (LPCMO) / 0.5 wt% Nb doped STO (SNTO) junction had also been studied by Sun et al [5], showing temperature dependent variation in the band structure at the LPCMO-SNTO interface. However, the most striking feature of p-n junction device was observed in $La_{0.9}Sr_{0.1}MnO_3$ (LSMO) / 0.01 wt% SNTO p-n junction, where a large positive MR nearly 94% around 255K and 26% at 290K has been reported [6]. The appropriate reason for such a large positive MR in manganite based p-n junction is yet to be understood. Various mechanisms have been suggested to explain the observation of large positive MR which improves the field sensitivity of the device [7]. Recently, it is proposed that, the competition between the MR of p-type manganite layer and of p-n junction, results in the positive MR in a bi-layered device [8]. From these discussions it is clear that a general consensus regarding the origin of large positive MR in the p-n junction device is yet to be attained.

In this chapter, the results on the fabrication of $La_{0.6}Pr_{0.2}Sr_{0.2}MnO_3$ (P-type) / $SrNb_{0.2}Ti_{0.8}O_3$ (n-type) bi-layer p-n junction device and the studies on the effect of thickness variation of p-type layer on I-V characteristics of p-n junction with and without applied magnetic field have been reported. The selection of LPSMO manganite was done due to its appreciable field sensitivity and higher transition temperature [9].

Synthesis

Two polycrystalline samples of $La_{0.8-x}Pr_{0.2}Sr_xMnO_3$ (x = 0.2 & 0.3) were synthesized using solid state reaction method. Dried powders of La_2O_3, Pr_6O_{11}, $SrCO_3$ and MnO_2 were mixed in stoichiometric proportions and calcined at 950°C for 24 hours. The samples were then ground, palletized and sintered in a temperature range of 1100°C - 1400°C with several intermediate grindings. These two well characterized targets (25 mm dia.) were used for the deposition of p-type layer on the $SrNb_{0.2}Ti_{0.8}O_3$ (SNTO) substrates to fabricate bi-layered p-n junction device using Pulsed Laser Deposition (PLD) technique. 248 nm KrF excimer laser was used for the fabrication of bi-layered p-n junction device. The parameters used for the deposition are given in the table below

➢ **Deposition parameters**	
Laser	248 nm KrF excimer
Target	$La_{0.8-x}Pr_{0.2}Sr_xMnO_3$ (x = 0.2 & 0.3)
Substrate	$SrNb_{0.2}Ti_{0.8}O_3$ (SNTO)
Laser energy	~ 2 J/cm^2
Repetition rate	10 Hz
Substrate temperature	700 °C
Distance between target & substrate	5.5 cm
Oxygen partial pressure	400 mTorr

The growth rate of p-type layer on SNTO substrate is ~ 0.28 nm / sec. By keeping the deposition time of 6 min and 12 min, the 100 & 200 nm $La_{0.6}Pr_{0.2}Sr_{0.2}MnO_3$ (LPS-II) and $La_{0.5}Pr_{0.2}Sr_{0.3}MnO_3$ (LPS-III) thin films were grown on SNTO substrate. The RMS roughness of the commercially procured SNTO substrate used was 1.065 nm and the substrate dimensions were 7.5 mm X 2.5 mm. Fig. 4.1 shows the schematic diagram of bi-layered p-n junction device grown and current perpendicular to plane (CPP) geometry used for the magneto I-V measurements. In this geometry the current is passed through

both the layers i.e. LPSMO & SNTO causing the current tunneling through barrier formed between p-type LPSMO & n-type SNTO substrate resulting in good rectifying properties of p-n junction device. In the another type of resistance measurement geometry known as current in plane (CIP) geometry, all the four leads are placed on the top surface of device or film.

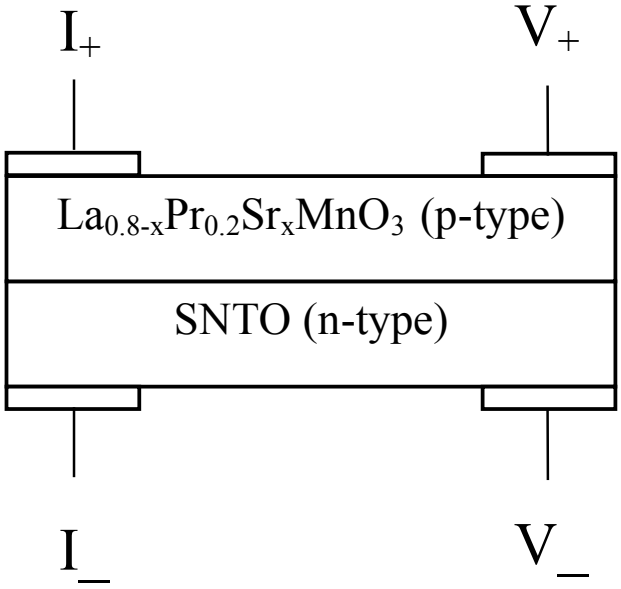

Figure 4.1 : Schematic diagram of bi-layered p-n junction device & CPP geometry for ρ-T measurements.

Structure

Rietveld fitted XRD patterns of $La_{0.8-x}Pr_{0.2}Sr_xMnO_3$ (x = 0.2 & 0.3) bulk target samples are shown in figs. 4.2 (a) & (b).

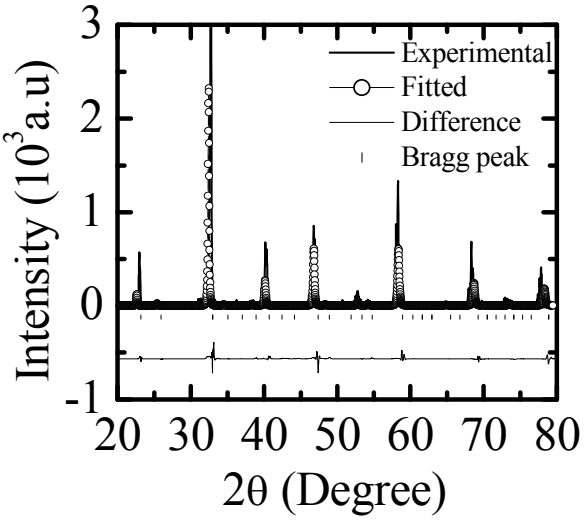

Figure 4.2 (a) : XRD pattern of $La_{0.6}Pr_{0.2}Sr_{0.2}MnO_3$ bulk.

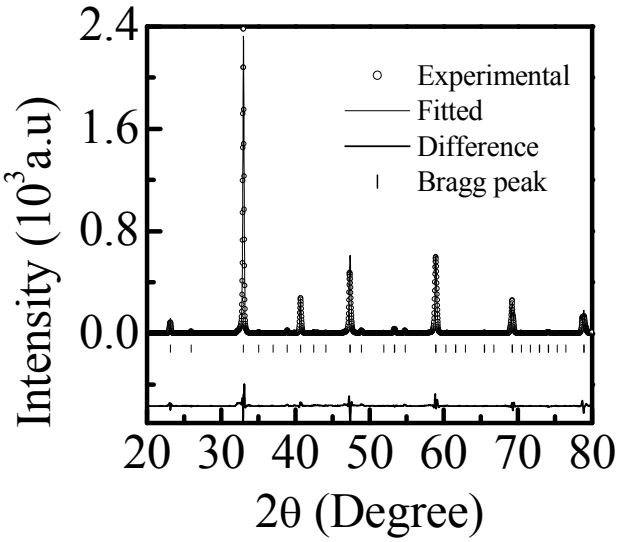

Figure 4.2 (b) : XRD pattern of $La_{0.5}Pr_{0.2}Sr_{0.3}MnO_3$ bulk.

Rietveld analysis of the XRD patterns of $La_{0.8-x}Pr_{0.2}Sr_xMnO_3$ (x = 0.2 & 0.3) samples using FULLPROF computer code [10] reveal that, both the samples are single phasic in nature and crystallize in a distorted orthorhombic structure (space group: *Pnma*, No. 62). The values of cell parameters and cell volume for both samples are listed in Table-1.

Table -1: Cell parameters (a, b & c) and cell volume (V) for $La_{0.8-x}Pr_{0.2}Sr_xMnO_3$ (x = 0.2 & 0.3) sample.

sample	a (Å)	b (Å)	c (Å)	V ($Å^3$)
LPS-II (x = 0.2)	5.519(2)	7.760(2)	5.485(2)	234.90
LPS-III (x = 0.3)	5.560(2)	7.774 (2)	5.511(2)	238.20

Before deposition of the p-type layer on SNTO substrate, 200 nm thin films of LPS-II and LPS-III samples were grown on STO substrate. Fig. 4.3 shows the resistivity vs. temperature plots of LPS-II & LPS-III films showing I-M transition T_{IM} ~ 305K & 347K for both samples, respectively.

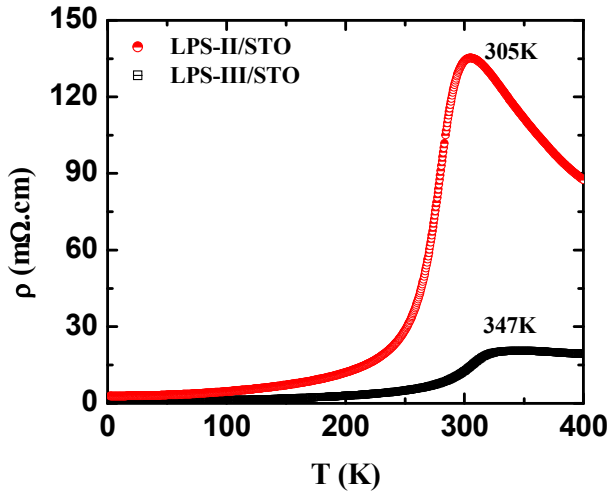

Figure 4.3 : Resistivity vs. temperature plots of $La_{0.8-x}Pr_{0.2}Sr_xMnO_3$ (x = 0.2 & 0.3) 200nm thin films grown on STO substrate.

4.2 Studies on $La_{0.6}Pr_{0.2}Sr_{0.2}MnO_3$ /$SrNb_{0.2}Ti_{0.8}O_3$ bi-layered device

The LPS-II/SNTO bi-layered device has been grown by depositing 100 nm & 200 nm thin LPS-II layers on SNTO substrate acting as n-type layer. The structural, surface morphological, transport, magneto I-V properties were studied using XRD, AFM and ρ-T measurements.

4.2.1 Structural studies

The XRD patterns of 100 & 200 nm LPS-II films deposited on SNTO substrates were indexed using orthorhombic cell parameters of bulk LPS-II compound and are shown in figs. 4.4 (a) & (b), respectively. From the XRD patterns, it can be seen that, there are no any impurity peaks and the growth of the p-type layer is oriented in *(0 K 0)* direction.

Fig. 4.5 shows X-ray ϕ-scan of LPS-II/SNTO bi-layered device which was performed by tilting the specimen in (1 2 2) direction from (0 0 2) direction of specimen crystal plane. Full scan was done by rotating p-n junction about the surface normal from 0° to 360° keeping the value of θ and tilt angle χ (48.19°) constant. It can be seen from figure that, there are four peaks, each separated by 90°, which recognize the cubic symmetry in the deposited LPS-II layer. These four sharp peaks confirm the epitaxial growth of LPS-II layer on SNTO substrate.

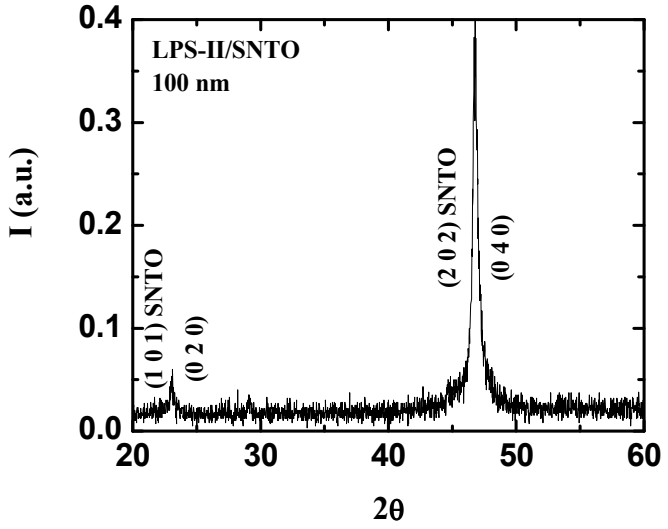

Figure 4.4 a) : XRD pattern of 100 nm LPS-II /SNTO bi-layered device.

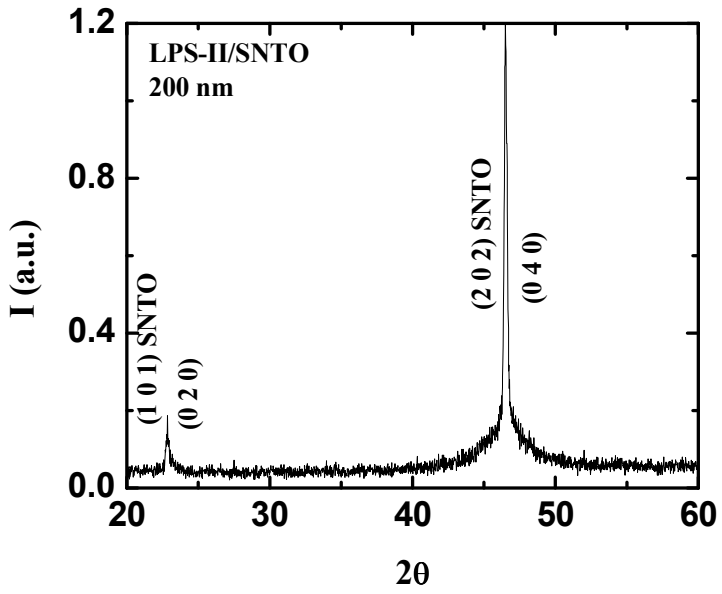

Figure 4.4 b) : XRD pattern of 200 nm LPS-II /SNTO bi-layered device.

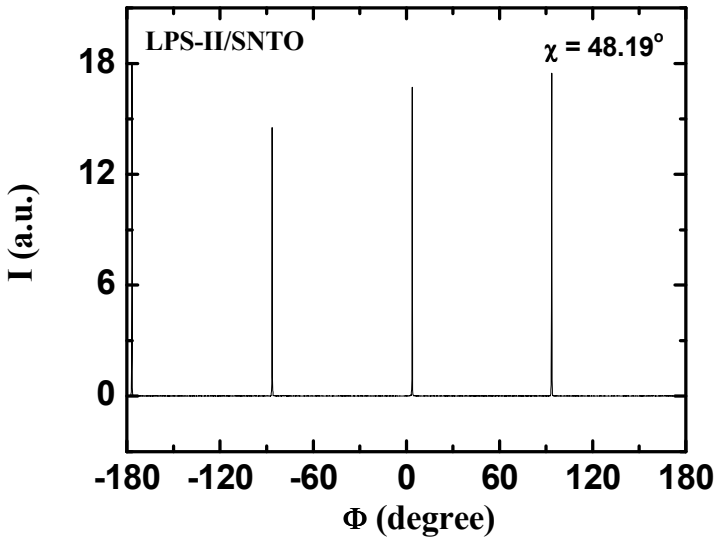

Figure 4.5 : X-ray ϕ scan of (1 2 2) peak of a LPS-II /SNTO bi-layered device.

4.2.2 Surface morphology

Figs. 4.6 & 4.7 shows the 2D & 3D AFM pictures of 100 nm LPS-II/SNTO bi-layered device while figs. 4.8 & 4.9 shows AFM pictures of 200 nm LPS-II/SNTO bi-layered device in 2D & 3D view, respectively.

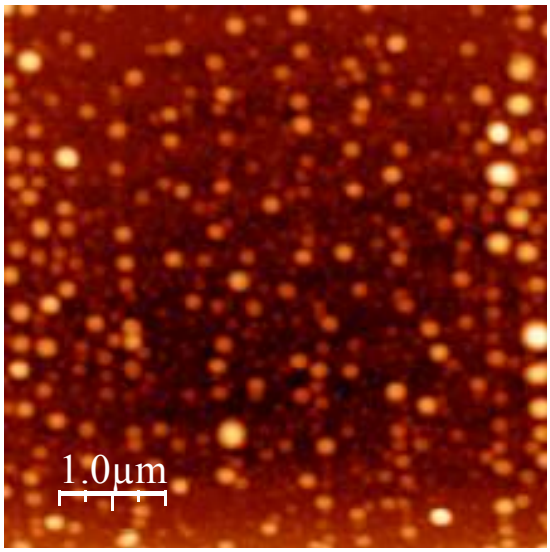

Figure 4.6 : 2D AFM picture of LPS-II/SNTO 100 nm bi-layered device.

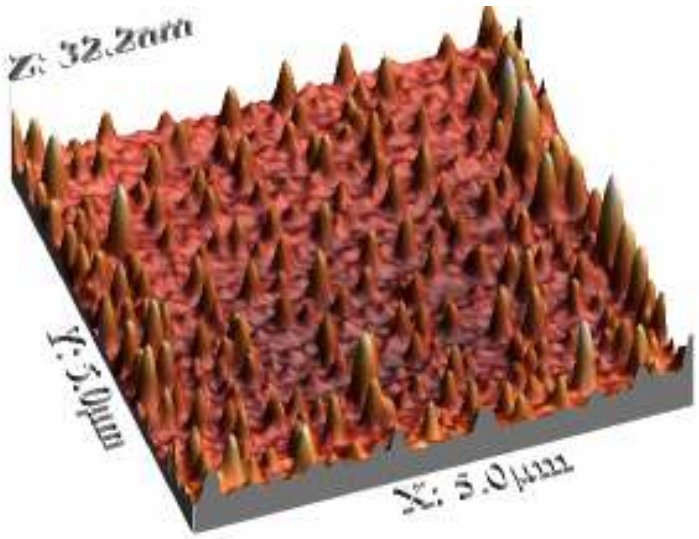

Figure 4.7 : 3D AFM picture of LPS-II/SNTO 100 nm bi-layered device.

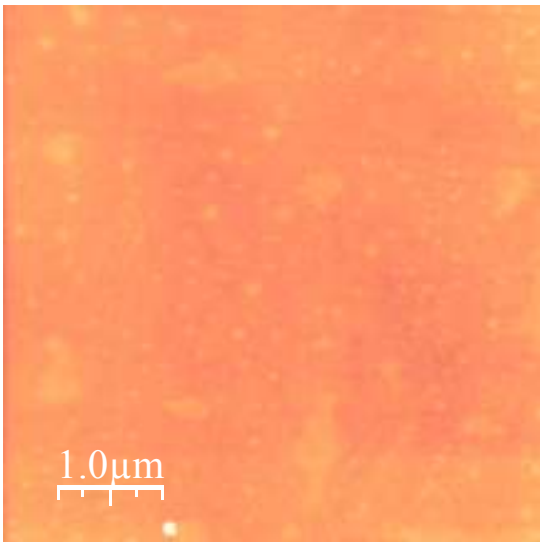

Figure 4.8 : 2D AFM picture of LPS-II/SNTO 200 nm bi-layered device.

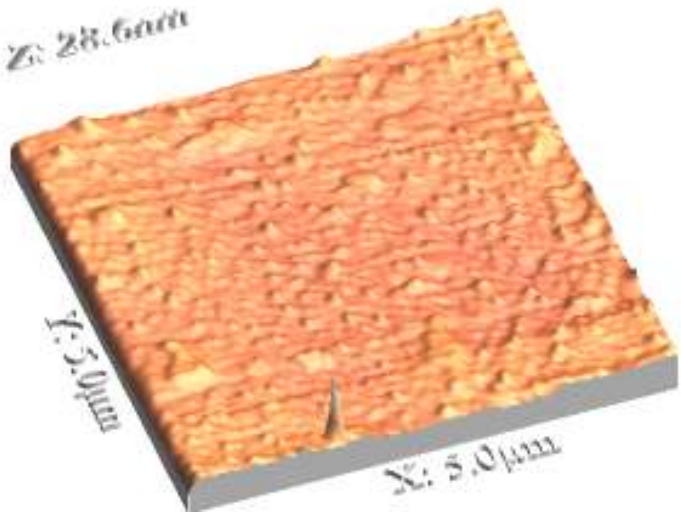

Figure 4.9 : 3D AFM picture of LPS-II /SNTO 200 nm bi-layered device.

It can be seen from the figures that, 100 nm device exhibit island like growth while 200 nm device possess barely smooth surface. The calculated value of grain size from AFM picture is ~ 150 nm for 100 nm LPS-II/SNTO device. The values of RMS surface roughness are ~ 4.02 nm and ~ 1.02 nm for 100 and 200 nm LPS-II/SNTO devices, respectively.

4.2.3 Magnetoresistance

The temperature dependent resistance measurements with and without applied magnetic field were carried out by applying 5 μA current in the CPP four probe geometry. Fig. 4.10 depicts the R-T plots of 100 & 200 nm LPS-II/SNTO device taken at 0T & 8T field. It can be seen that, the 100 nm LPS-II/SNTO device exhibit I-M transition at ~ 115K while 200 nm device exhibits T_{IM} ~ 225K at 0T. With the increase in I-M transition the peak resistance also decreases which may be due to the better interface of 200 nm LPS-II film and SNTO substrate. Since the change in thickness is achieved by changing deposition time, the 200 nm film possesses better interface. Fig. 4.11 shows MR% versus temperature plots of 100 & 200 nm LPS-II/SNTO bi-layered devices with applied field of 8T. Both the bi-layered p-n junctions exhibit negative MR% below RT which becomes positive at and above RT.

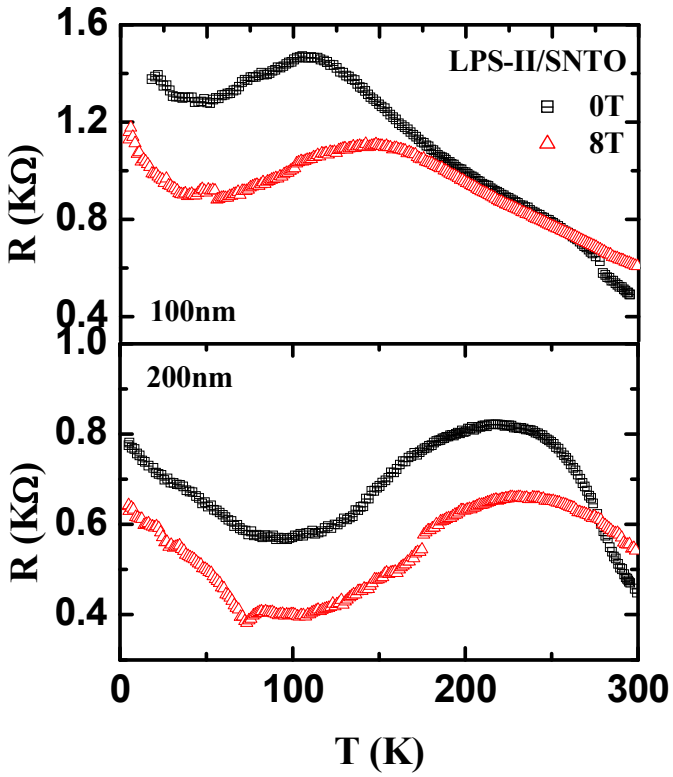

Figure 4.10 : Resistance versus temperature plots of 100 nm & 200 nm LPS-II/SNTO bi-layered device with and without applied magnetic field.

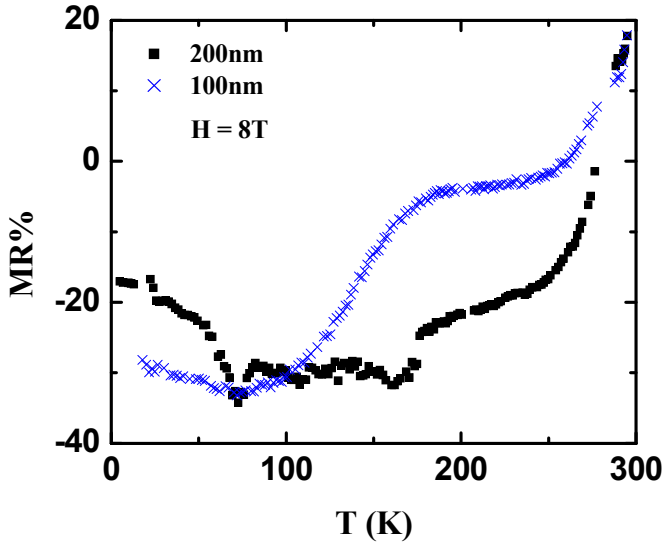

Figure 4.11 : MR% versus temperature plots of 100 nm & 200 nm LPS-II /SNTO bi-layered device at 8T field

4.2.4 Magneto I-V

Field dependent I-V characteristics of the bi-layered manganite devices were studied by applying field parallel to the p-n junction interface and perpendicular to the applied current. To eliminate joule heating effect, the value of applied current was limited to 6 mA. The I-V curves obtained at 5 & 300K for 100 nm LPS-II/SNTO bi-layered junction under 0-8T fields are shown in fig. 4.12. It can be seen that, 100 nm LPS-II/SNTO junction exhibits good rectifying behavior having negligible effect of magnetic field on its rectifying property at 5K. This negligible MR gets converted to a large positive MR at 300K. The value of saturation voltage (V_C) is ~ 140 mV & ~ 110 mV at 5K & 300K, respectively. The variation in the value of V_C with applied field is very small at 5K while at 300K, V_C increases appreciably under 8T field.

Fig. 4.13 shows I-V curves of 200 nm LPS-II/SNTO bi-layered junction under 0-8T fields at 5 & 300K. This junction also exhibits good rectifying behavior and negligible effect of magnetic field on its rectifying property at 5K. The value of V_C is ~ 64 mV & ~ 67 mV under 0T at 5K & 300K, respectively. A variation in the value of

V_C with applied magnetic field is observed similar to 100 nm device. From the comparison

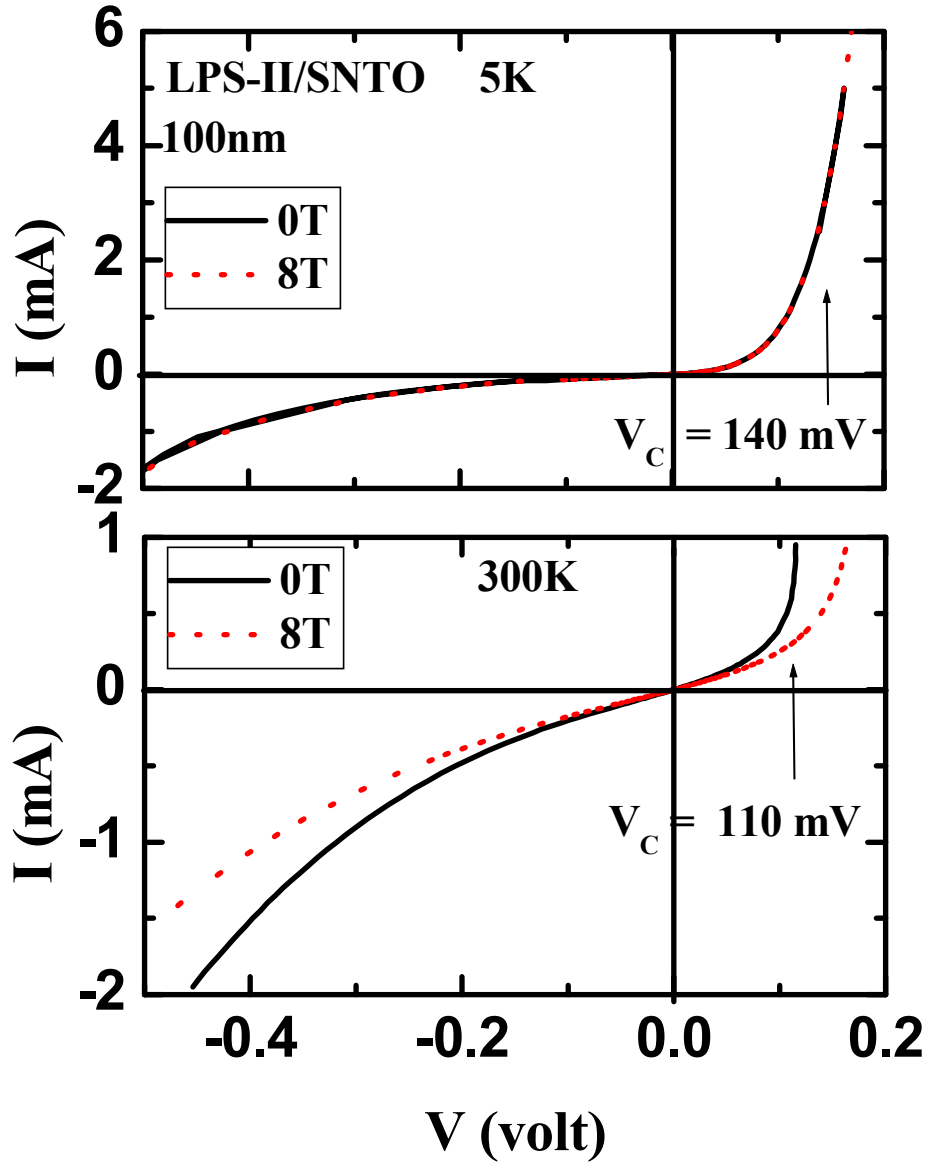

Figure 4.12 : Plots of I-V characteristics with and without applied field at temperature of 5 and 300K for the 100 nm LPS-II /SNTO bi-layered device.

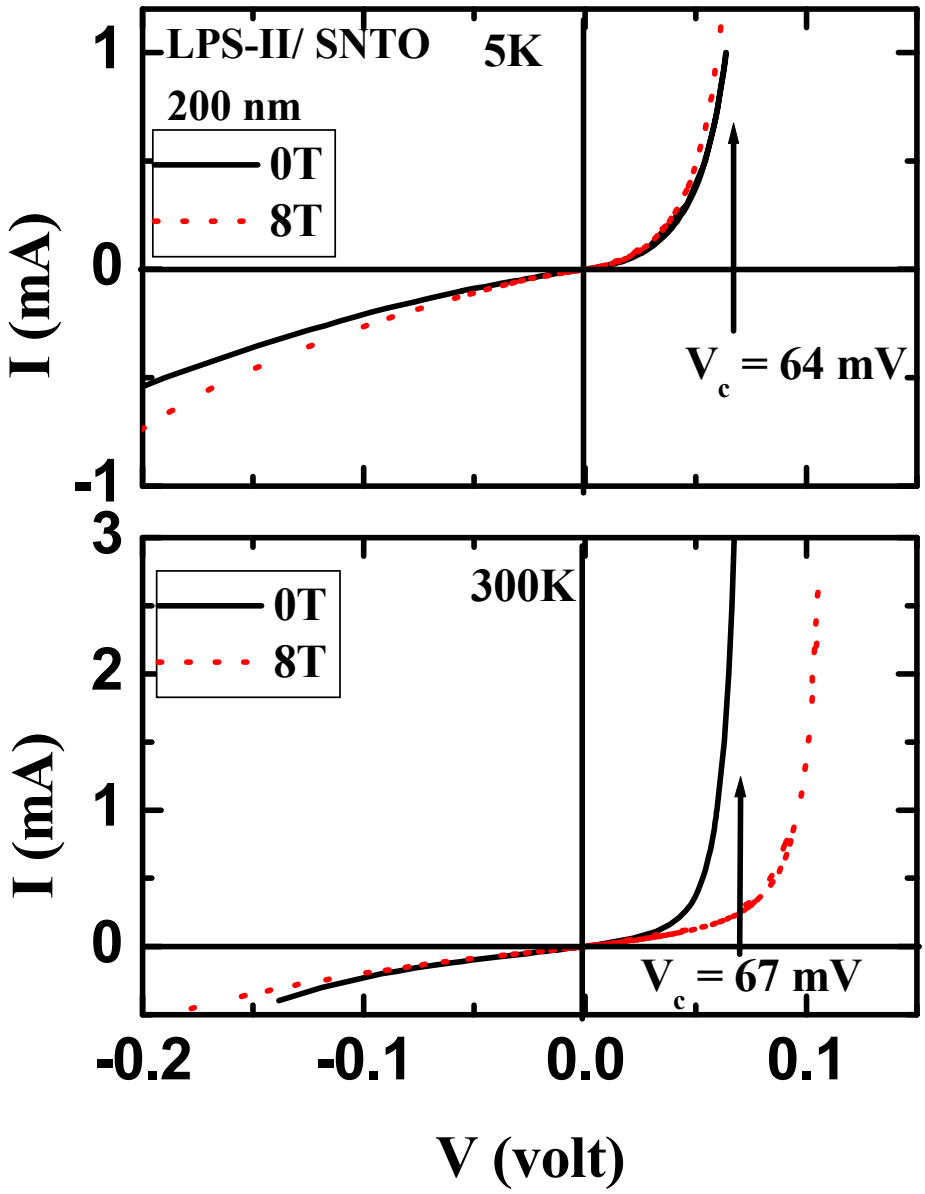

Figure 4.13 : Plots of I-V characteristics with and without applied field at temperature of 5 and 300K for the 200 nm LPS-II /SNTO bi-layered device.

of the I-V behavior of 200 & 100 nm LPS-II/SNTO devices, it can be seen that, the V_C decreases with increasing film thickness (in 100 nm film V_C ~ 140 mV at 5K while in 200 nm film V_C ~ 64 mV at 5K).

The MR ratios of the bi-layered junctions plotted as a function of applied current at two different temperatures, 5 and 300K are shown in figs. 4.14 (a) & (b), respectively. The observed maximum negative MR ~ -3% and -17% at 5K becomes positive ~ 43% and ~ 65% at 300K for 100 & 200 nm bi-layered junctions, respectively. The large MR ~ 50% has been observed at 300K in an applied current of only 0.15 mA for the 200 nm bi-layered junction, however, MR% value saturates at 65% beyond 0.5 mA.

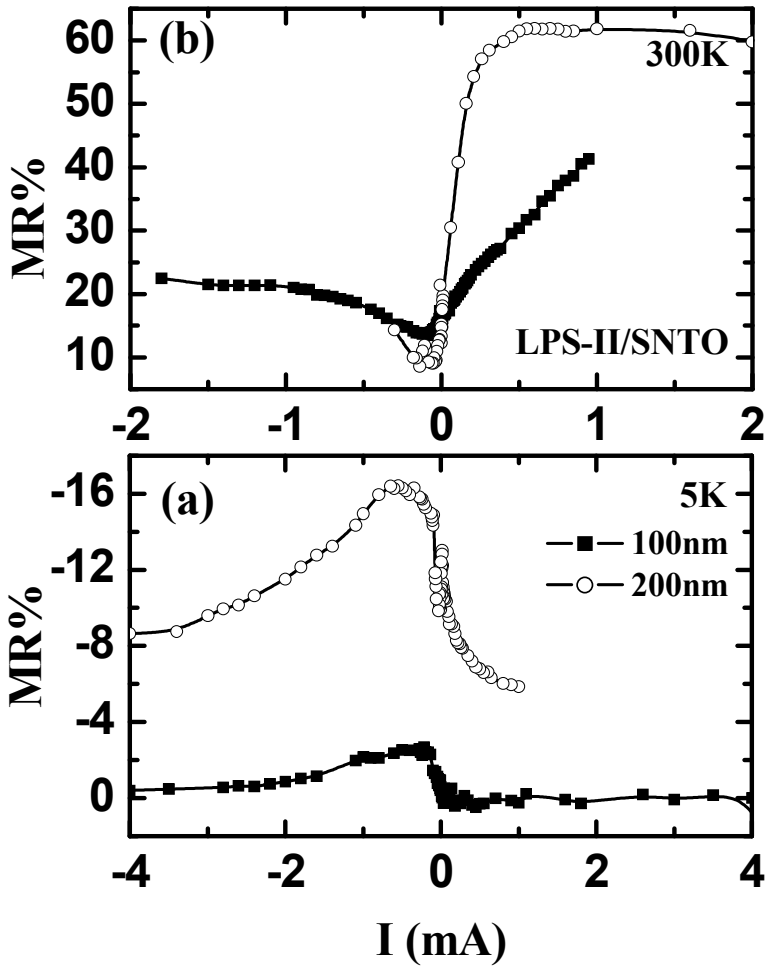

Figure 4.14 : MR% vs I plots of 100 and 200 nm LPS-II /SNTO bi-layered device at temperature of 5 and 300K under applied field of 8T.

4.3 Studies on $La_{0.5}Pr_{0.2}Sr_{0.3}MnO_3$ /$SrNb_{0.2}Ti_{0.8}O_3$ bi-layered device

The LPS-III /SNTO bi-layered device was fabricated by depositing 100 nm & 200 nm thin LPS-III layer on SNTO substrate to study the carrier density dependent magneto I-V properties.

4.3.1 Structural studies (XRD & HR-XRD)

The XRD pattern of LPS-III/SNTO device (fig. 4.15) was indexed using orthorhombic cell parameters of bulk LPS-III compound. From the XRD pattern, it can be seen that, there are no any impurity peaks and the growth of the p-type layer is oriented in *(0 K 0)* direction.

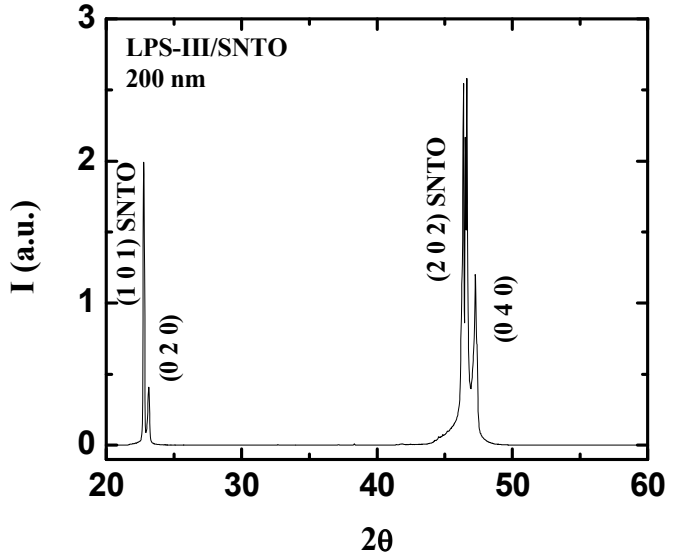

Figure 4.15 : XRD pattern of LPS-III/SNTO bi-layered device.

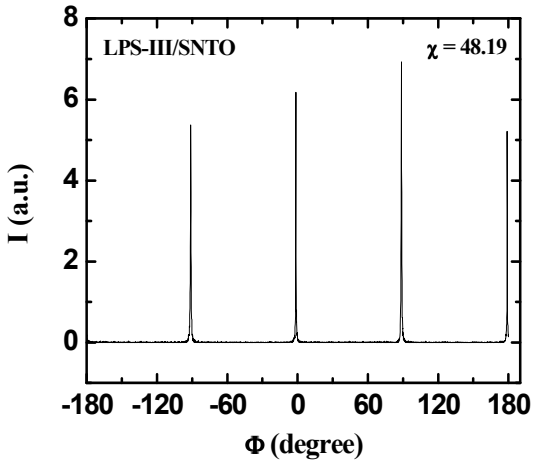

Figure 4.16 : X-Ray ϕ-scan of (1 2 2) peak of LPS-III/SNTO bi-layered device.

Fig. 4.16 shows X-ray ϕ-scan of LPS-III/SNTO bi-layered device which was performed by tilting the specimen crystal plane. The ϕ-scan confirms the epitaxial growth of LPS-III layer on SNTO substrate.

4.3.2 Surface morphology

Figs. 4.17 & 4.18 show AFM pictures of 100 nm LPS-III/SNTO bi-layered device in 2D and 3D view, respectively while figs. 4.19 & 4.20 shows the 2D & 3D AFM micrographs of 200 nm LPS-III/SNTO bi-layered device, respectively. It can be seen from the figures that, both (100 & 200 nm) the devices possess island like growth. The calculated values of grain sizes from AFM pictures are ~ 30 nm & ~ 26 nm and the RMS surface roughness values are ~ 0.82 nm & 0.75 nm for 100 & 200 nm LPS-III/SNTO films, respectively.

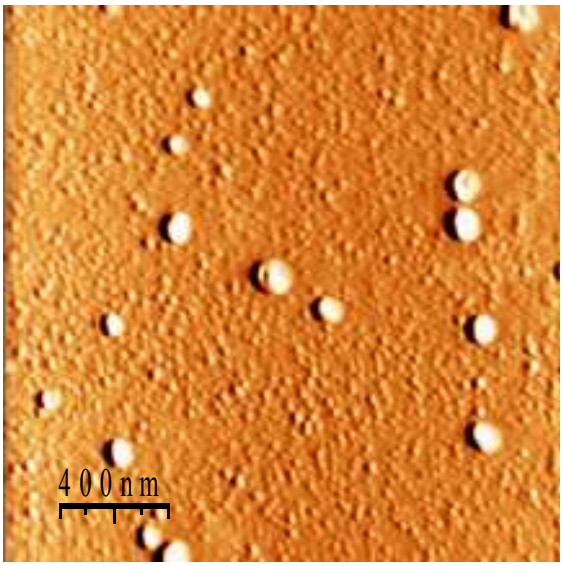

Figure 4.17 : 2D AFM picture of LPS-III /SNTO 100 nm bi-layered device.

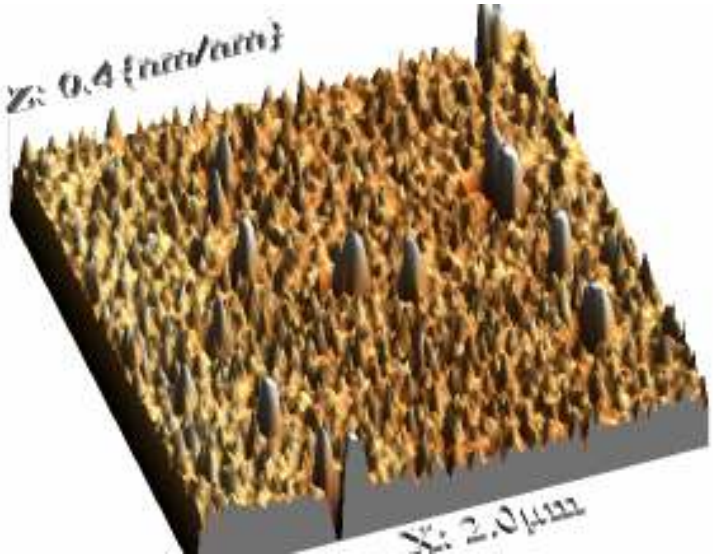

Figure 4.18 : 3D AFM picture of LPS-III /SNTO 100 nm bi-layered device.

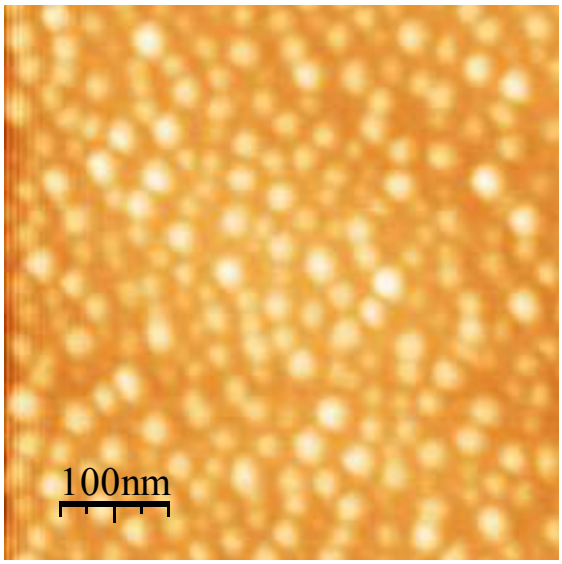

Figure 4.19 : 2D AFM picture of LPS-III /SNTO 200 nm bi-layered device.

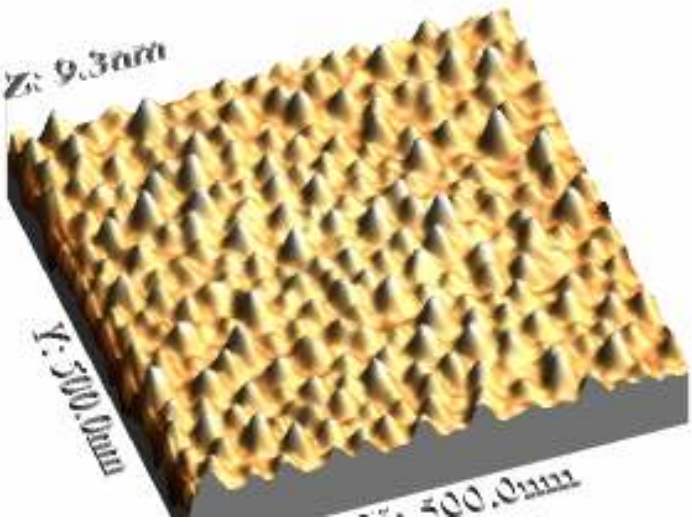

Figure 4.20 : 3D AFM picture of LPS-III /SNTO 200 nm bi-layered device.

4.3.3 Magnetoresistance

The plots of variation of resistance with temperature with and without applied magnetic field for 100 & 200 nm LPS-III/SNTO devices are shown in fig. 4.21. The applied currents were kept 5 μA and 100 μA for 100 nm & 200 nm LPS-III/SNTO devices, respectively. The 200 nm LPS-III SNTO device exhibits I-M transition at ~ 126K while 100 nm device do not show any I-M transition in 0T field. Under 8T field, the 100 nm device exhibit a broad I-M transition around 155K.

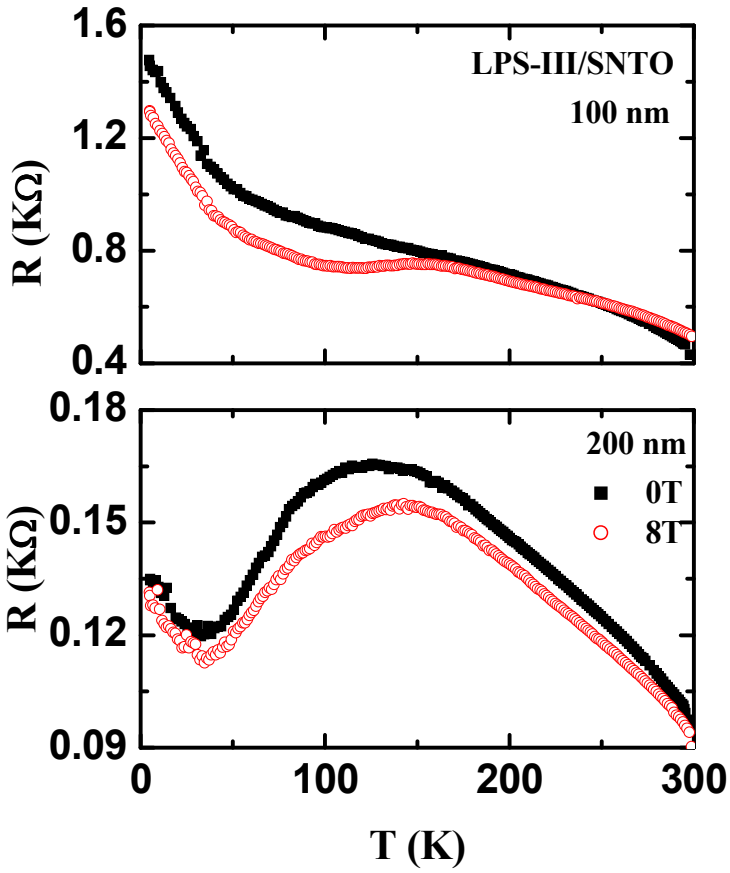

Figure 4.21 : R-T plots of 100 nm & 200 nm LPS-III/SNTO bi-layered device with and without applied magnetic field.

It has been observed that, the passage of 5μA current through 100 nm LPS-III/SNTO device is not sufficient for inducing I-M transition while the passage of 100μA current excites sufficient charge carriers resulting into I-M transition in 200 nm

device. This result supports the electric field dependent modulation of Zener double exchange reported by Tanaka et al [4].

Fig. 4.22 shows MR% versus temperature plots of 100 nm & 200 nm LPS-III/SNTO bi-layered devices in 8T field. In 200 nm device, the sign of MR changes from negative to positive in the temperature range 5-300K while 100 nm device exhibits only negative MR up to 300K.

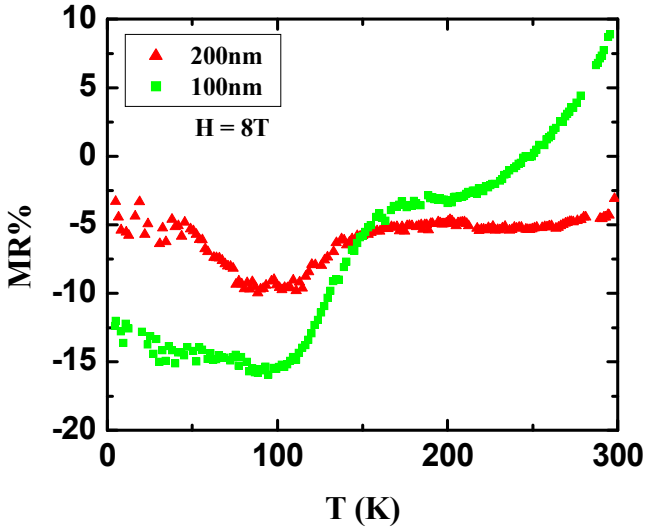

Figure 4.22 : MR% versus temperature plots of 100 nm & 200 nm LPS-III /SNTO bi-layered device at 8T applied field.

4.3.4 I-V and Magneto I-V

In order to understand the effect of temperature on transport properties of p-n junction device, temperature dependent I-V measurements were performed on the 200 nm LPS-III/SNTO device. Fig. 4.23 shows I-V characteristic plots taken at 5K, 100K, 150K, 200K & 250K. It can be seen from the I-V plots that, the device exhibit good rectifying properties at all temperatures. At low temperatures, I-V curve possess less inclination to the current (I) axis, and pushes saturation voltage (V_C) to higher values. Fig. 4.24 depicts the variation of V_C with temperature for LPS-III/SNTO device. It can

be seen from figure that, at low temperature V_C is maximum while with the increase in temperature, V_C decreases.

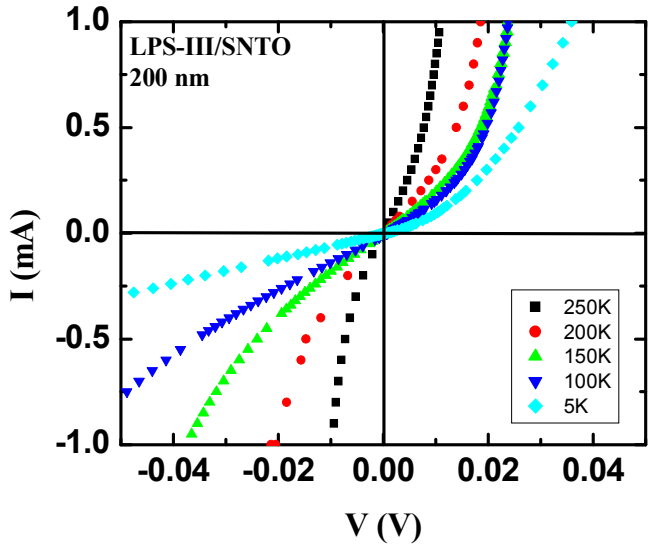

Figure 4.23 : Plots of I-V characteristics at temperature of 5, 100, 150, 200 & 250K for 200 nm LPS-III/SNTO bi-layered device.

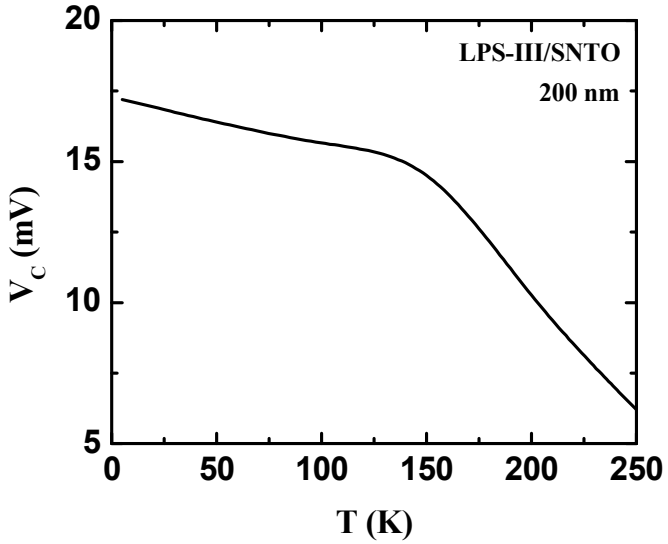

Figure 4.24 : Saturation voltage (V_C) versus temperature plot of 200 nm LPS-III/SNTO bi-layered device.

The magneto I-V curves obtained at 5 and 300K for 100 nm LPS-III/SNTO bi-layered junction under 0-8T field are shown in figs. 4.25 (a) & (b), respectively. It can be seen from the figures that, 100 nm LPS-III/SNTO junction exhibit good rectifying behavior at 5K with V_C ~ 140 mV and negligible effect of magnetic field on its rectifying property while at 300K, the junction possess positive MR ~ 22% and V_C ~ 118 mV.

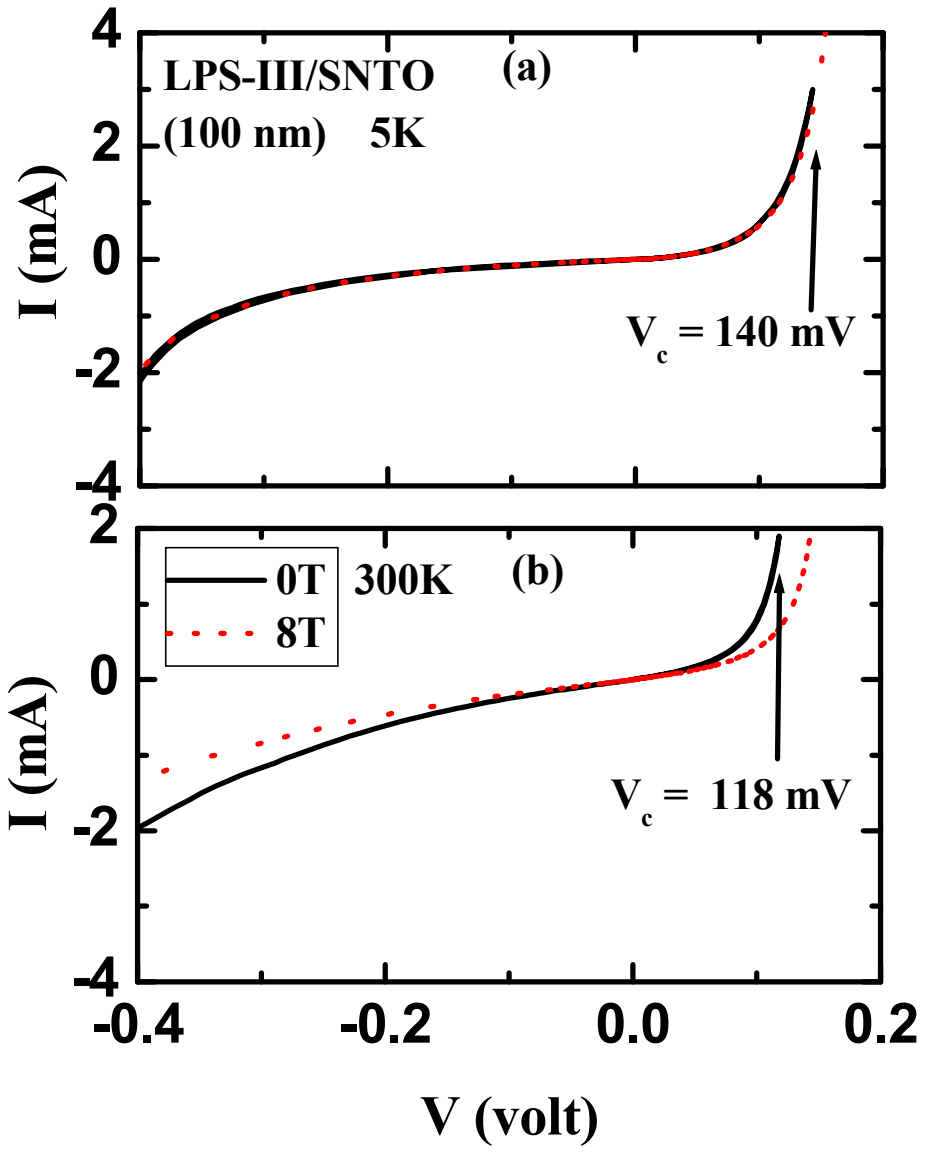

Figure 4.25 : Plots of I-V characteristics with and without applied field at a) 5K & b) 300K for the 100 nm LPS-III/SNTO bi-layered device.

Fig. 4.26 shows I-V curves of 200 nm LPS-III/SNTO junction under 0-8T field at 5 & 300K. The junction exhibits rectifying behavior at 5K with V_C ~ 16 mV. At 300K, the junction possess almost linear behavior.

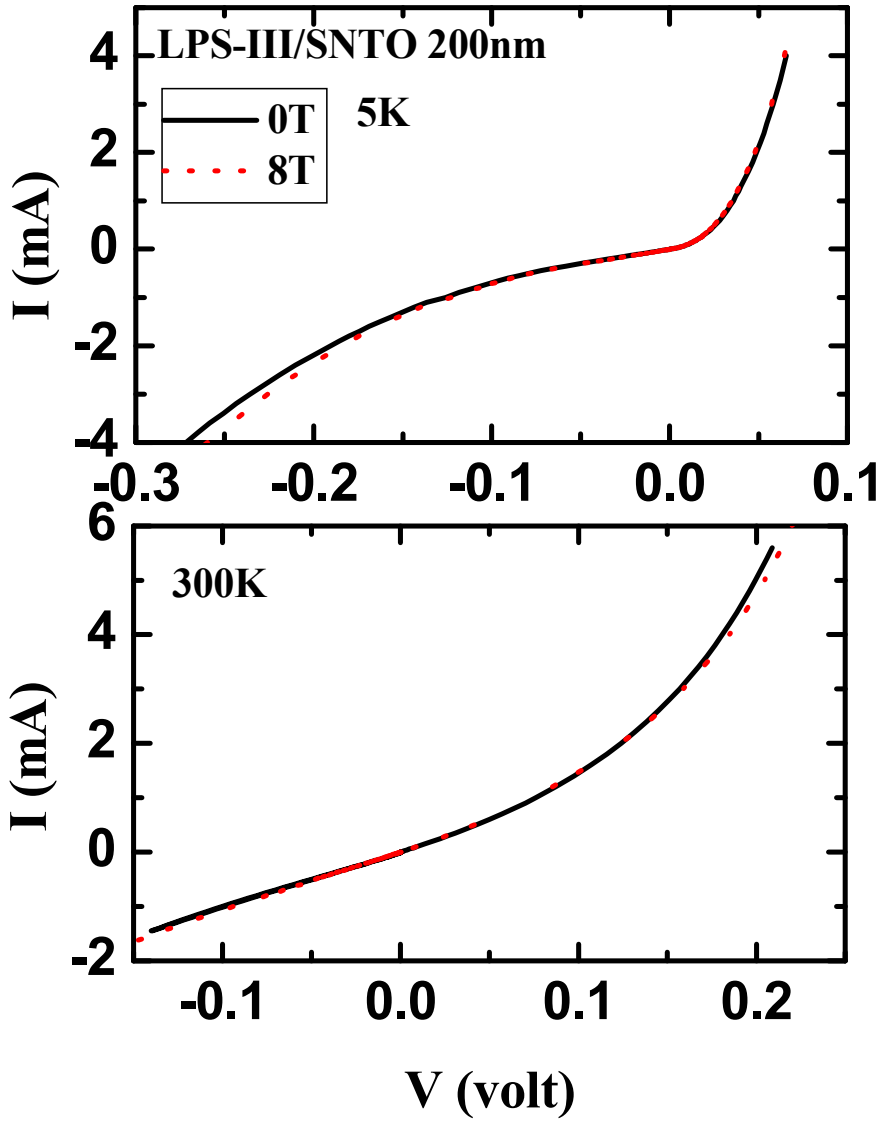

Figure 4.26 : Plots of I-V characteristics with and without applied field at temperature of 5 and 300K for the 200 nm LPS-III /SNTO bi-layered device.

The MR ratios of the 100 nm LPS-II/SNTO and LPS-III/SNTO bi-layered devices plotted as a function of applied current (I) at 5K & 300K are shown in figs. 4.27 (a) & (b), respectively. The maximum MR values observed are ~ 22% and ~ 43% at 300K for 100 nm LPS-III/SNTO and LPS-II/SNTO junctions, respectively.

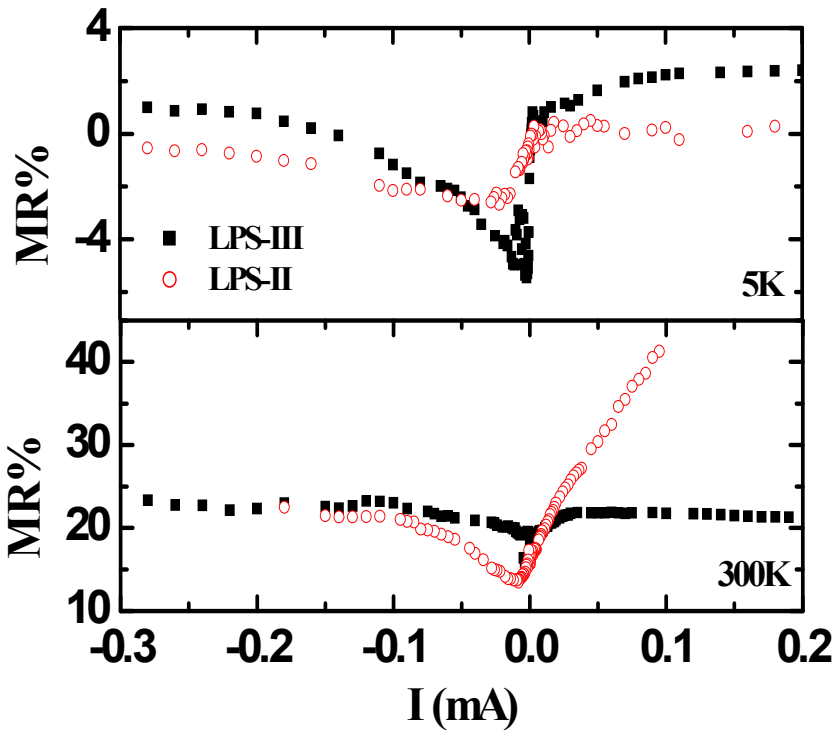

Figure 4.27 : MR% vs I plots of LPS-II/SNTO and LPS-III/SNTO bi-layered device at temperature of 5 and 300K under applied field of 8T.

4.4 Discussion on I-V and magneto I-V studies

The I-V and magneto I-V properties of p-n junctions studied are analyzed using temperature, thickness and carrier density dependent behavior.

- **Temperature dependent magneto I-V properties**

With the increase in temperature the value of V_C decreases and to understand the observed decrease, first let us see at the band diagram of p-n junction (fig. 4.28), which was given by J.R. Sun et al [5].

Depending upon the valence state, Mn ion (either +3 or +4) has three or four electrons in its outermost orbital, among which, three electrons occupy localized t_2g band while remaining one occupy the e_g band. In addition, due to Hund's coupling, conducting e_g band further splits into two sub-bands, $e_g \uparrow$ (e_g spin up) and $e_g \downarrow$ (e_g spin down) sub-bands and Fermi level locates at $e_g \uparrow$ sub-band [11]. A energy barrier could be formed at the LPS-III/SNTO junction after reminder that Fermi energy of n-type SNTO is near conduction band [12]. Now, the energy of the band gap $e_g \uparrow$ - $e_g \downarrow$, is nothing but the energy required to tunnel the conduction electrons, means V_C. Therefore, when the voltage on interface exceeds than V_C, energy barrier overcomes and large increase in current appears. At low temperature, the e_g electron spins are fully aligned. But, with increase in temperature, spin deviates from fully ferromagnetic alignment. This implies less energy for the e_g electron to reverse its direction. Thus, with the increase in temperature, the energy gap between e_g band ($e_g \uparrow$ - $e_g \downarrow$) will decrease and vanishes when $T > T_C$ [13]. In summary of all these discussions, V_C decreases with temperature up to T_C and above T_C it becomes almost constant.

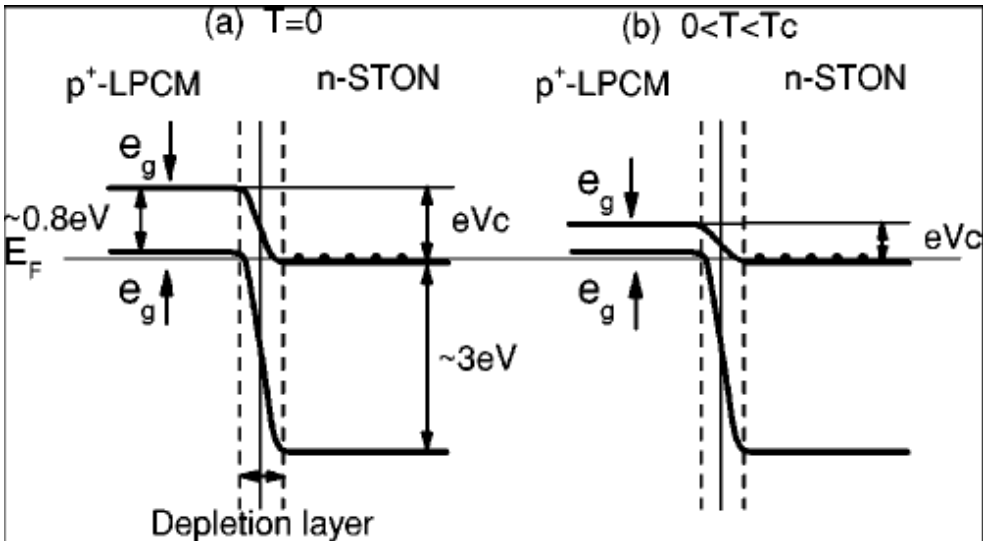

Figure 4.28 : Schematic diagram for the band structure of $La_{0.32}Pr_{0.35}Ca_{0.33}MnO_3$ (LPCM) and SNTO at (a) T = 0 and (b) $0 < T < T_C$ [5].

- **Thickness dependent magneto I-V properties**

In the presently studied bi-layered junctions, the variation in the V_C is quit small, for 100 nm junction, between 140 to 110 mV at 5K & 300K while for the 200 nm junction, $V_C \sim 64$ mV at 5K which slightly changes to 67 mV at 300K. Interestingly, the thickness dependent modification in V_C is appreciable in the LPSMO/SNTO junction such that, V_C decreases from 140 mV to 64 mV at 5K in 100 & 200 nm films, respectively while at 300K, the similar decrease in V_C is observed in both the films. The decrease in V_C with film thickness at 5 & 300K is accompanied by an appreciable increase in MR from 43% to 65% for 100 & 200 nm films at 300K. This can be attributed to the thickness dependent modification in the depletion layer width between p-n junction. As we increase the thickness of p-type layer, the width of depletion layer might decrease resulting in the decrease in V_C for the 200 nm junction. Now, let us understand the cause of reduction in V_C due to increase in thickness. As it is earlier reported by H. Tanaka et al [4] that, the estimated depth of depletion layer in the p-n junction is less than 1 unit cell, the change in thickness of more than 100 nm merely will not affect the depletion layer width. Since the difference in thicknesses of the films is obtained by varying the duration of deposition in the 400 mTorr oxygen partial pressure

at 700 °C, it is possible that the difference in annealing duration may affect the interface between substrate apart from substrate induced strain on the grown film. This possibility improves the interface and thus lowers the overall resistance of the junction and also enhances the semiconducting to metal transition temperature as shown in resistance versus temperature plot (fig. 4.10).

- **Carrier density dependent magneto I-V properties**

To explore the effects of carrier density of p-type layer on magneto I-V properties of bi-layered p-n junction device, we have compared the results of magneto I-V on 100 nm LPS-II/SNTO with 100 nm LPS-III/SNTO bi-layered p-n junctions. It is found that, the V_C decreases from 162 mV to 142 mV at 5K in LPS-II/SNTO & LPS-III/SNTO p-n junctions, respectively, while at 300K, V_C slightly varies from 115 mV to 118 mV in LPS-II/SNTO & LPS-III/SNTO, respectively. Moreover, the observed maximum MR ratios are negligible for both the p-n junctions at 5K while at 300K, MR ~ 46% and ~ 22% has been observed for LPS-II/SNTO and LPS-III/SNTO p-n junctions, respectively. A small carrier density of p-type layer exhibits large MR (~46%) as compared to p-n junction having more carrier density. From figs. 4.10 & 4.21 (R-T graphs), it is seen that, LPS-II/SNTO exhibits I-M transition at 115K while LPS-III/SNTO shows insulating behavior in the 5-300K temperature range. This indicates that, though LPS-III/SNTO has larger carrier density may have less conducting carriers as compared to LPS-II/SNTO. Moreover, the large difference in grain sizes i.e. ~ 150 nm for LPS-II/SNTO and ~ 30 nm for LPS-III/SNTO p-n junction also affects the I-V properties.

Hence, the large MR observed for LPS-II/SNTO may be due to more carriers responsible for conduction and also the large grain size of p-type layer. It can be concluded that, the smaller carrier density results in large MR. Further detailed investigations on interface (using cross-sectional TEM) are required for indepth explanation of the effect of carrier density of p-type layer on magneto I-V properties of p-n junctions.

4.5 Summary and Conclusions

In this chapter, the bi-layered p-n junction devices of the form LPSMO/SNTO have been fabricated using PLD technique. The XRD pattern of the grown p-n junction devices, reveal that, all of them possess single phase structure with no impurity peaks and the growth of the p-type layer is oriented in *(0 K 0)* direction. Four peaks, each separated by 90°, are observed in the ϕ scan of the p-n junction which confirms that the deposited LPSMO layer on SNTO substrate has cubic symmetry and is grown epitaxially on the substrate. It is seen from the AFM micrographs that, 200 nm LPS-II/SNTO junction have barely smooth surface suggesting layer by layer growth mode while all other junction possess island like growth. In addition, LPS-II/SNTO junctions have RMS surface roughness in the range of 1-4 nm and average grain size ~ 150 nm which is much larger as compared to LPS-III/SNTO junction (RMS surface roughness < 1 nm, average grain size < 30 nm).

Field dependent R-T measurements show I-M transition in the LPS-II/SNTO junctions in an applied current of 5 μA. While the passage of 100 μA current results in I-M transition in LPS-III/SNTO junction. From MR vs. T plots, it has been observed that, all p-n junctions exhibit negative MR at low temperature which becomes positive at higher temperature. In LPS-II/SNTO p-n junction MR changes its sign near 300K while at 150K, the MR sign changes in LPS-III/SNTO device. The maximum MR is observed ~ 65% under 8T field at 300K for the 200 nm LPS-II/SNTO junction. However, in the same junction, an appreciable MR ~ 50% has been observed at 300K in an applied current of only 0.15 mA.

Studies on the I-V and magneto I-V measurements on the manganite p-n junction devices show that, all of them exhibit good rectifying property and under application of magnetic field device exhibits negligible MR at low temperature while high positive MR is observed at higher temperature. The 200 nm p-n junctions posses better LPSMO-SNTO interface which results in large MR. It also exhibit higher I-M transition temperature and lower resistance due to good interface which may result due to difference in the annealing duration. The temperature dependent I-V measurements on junction reveal that saturation voltage observed in p-n junctions is temperature dependent in which V_C decreasing with increase in temperature and after transition temperature it remains almost constant.

REFERENCES

1. E. Dagotto, T. Hotta, A. Moreo,

Physics Report **344**, 1-153 (2001).

2. Yu Lu, X.W. Li, G.Q. Gong, Gang Xiao, A. Gupta, P. Lecoeur, J.Z. Sun, Y.Y. Wang and V.P. Dravid,

Phys. Rev. B **54**, R8357 (1996).

3. J.H. Markna, P.S. Vachhani, R.N. Parmar, D.G. Kuberkar, P. Misra, B.N. Singh, L.M. Kukreja, D.S. Rana and S.K. Malik,

Euro. Phys. Lett. **79**, 17005 (2007).

4. Hidekazu Tanaka, Jun Zhang and Tomoji Kawai,

Phys. Rev. Lett. **88**, 027204 (2002).

5. J.R. Sun, C.M. Xiong, T.Y. Zhao, S.Y. Zhang, Y.F. Chen and B.G. Shen,

Appl. Phys. Lett. **84**, 1528 (2004).

6. H.B. Lu, S.Y. Dai, Z.H. Chen, Y.L. Zhou, B.L. Cheng, K.J. Jin, L.F. Liu, G.Z. Yang and X.L. Ma,

Appl. Phys. Lett. **86**, 032502 (2005).

7. Kui-juan Jin, Hui-bin Lu, Qing-li Zhou, Kun Zhao, Bo-lin Cheng, Zheng-hao Chen, Yue-liang Zhou and Guo-Zhen Yang,

Phys. Rev. B **71**, 184428 (2005).

8. D.J. Wang, Y.W. Xie, C.M. Xiong, B.G. Shen and J.R. Sun,

Euro. Phys. Lett. **73** (3) 401 (2006).

9. J.H. Markna, R.N. Parmar, D.S. Rana, Ravi Kumar, P. Misra, L.M. Kukreja, D.G. Kuberkar and S.K. Malik,

NIM B **256**, 693 (2007).

10. J. Rodriguez_Carvajel, FULLPROF version 3.0 Laboratorie Leon Brillioun, CEA-CNRS, (1995).

11. C. Mitra, P. Raychaudhuri, K. Dorr, K.-H. Muller, L. Schultz, P.M. Oppencer and S. Wirth,

Phys. Rev. Lett. **90**, 017202 (2003).

12. M. Cardona,

Phys. Rev. **140**, 651 (1965).

13. J.Y.T. Wei, N.-C. Yeh and R.P. Vasquez,

Phys. Rev. Lett. **79**, 5150 (1997).

The electronic transport and magnetotransport properties of $La_{0.5}Pr_{0.2}Ba_{0.3}MnO_3$ (LPBMO) Polycrystalline bulk and thin films synthesized, using Pulsed Laser Deposition (PLD) technique, have been well studied [1-3]. In this chapter, attempt has been made to study in detail, the effect of 200 MeV Ag^{+15} Swift Heavy Ion (SHI) irradiation on transport and magnetotransport properties of LPBMO thin films grown using low cost Chemical Solution Deposition (CSD) technique. The commonly used techniques used for the deposition of high quality epitaxial manganite thin films are, Pulsed Laser Deposition (PLD), RF sputtering, Metallorganic Chemical Vapour Deposition (MOCVD), Molecular Beam Epitaxy (MBE), Chemical Solution Deposition (CSD) technique etc. [4-7]. Amongst all these techniques, Chemical Solution Deposition (CSD), has number of advantages over the other conventional deposition techniques. It is cost-effective, compositional compatible, yields stochiometrically predefined compounds and provides the variety of alternative precursors to choose, contains wide range of concentration, viscosity and pH, easier to set up and handle etc. [8, 9]. In the second part of this chapter, the results on the studies on effect of substitution of Lutetium (Lu) (Rare earth ion with smaller ionic radius) at La-site in the $La_{0.7}Sr_{0.3}MnO_3$ (LSMO) manganite system have been discussed. The main aim behind doping of Lu-ion at La-site in LSMO system is to study the effect of large disorder (σ^2 = 0.0036 $Å^2$) and size variance on the structural and magnetotransport properties of the system. Our earlier studies on the effect of size disorder on the structural transport and magnetotransport of various La-based manganites have shown interesting results [10, 11].

It is an established fact that, SHI irradiation results in the formation of defect states in the thin films which in turn modifies various properties. In the present work, we have used 200 MeV Ag^{+15} ions having larger mass and known to create columnar defects. Ag^{+15} ions on passing through the material, losses energy mainly in two ways i) inelastic collision of highly charged energetic ions with the atomic electron of the matter, termed electronic energy loss ($S_e = dE_e/dX$), and ii) elastic scattering from the nuclei of atom of the matter, called nuclear energy loss ($S_n = dE_n/dX$) electrons. The calculated electronic and nuclear energy losses for 200 MeV Ag-ions passing through LPBMO films are S_e ~ 21 KeV/nm and S_n ~ 60.3 eV/nm and projected range of Ag^{+15} ions was found to be ~ few μm using SRIM-2003 (The stopping and range of ion in

matter) [12]. Here, projected range of Ag ions is very high as compared to thickness of film (150 nm), which ensures that the Ag ions pass through the film and rests on the substrate. The passage of Ag ions through thin film results in the modification in microstructure resulting in lattice strain having similar effects as external hydrostatic pressure. It is reported that, the external pressure modifies both, the bond length and bond angle of Mn-O-Mn, which in turn results in change of itinerant e_g electron bandwidth and hence in the modifications of the magnetotransport properties of manganites [13]. In the similar fashion, SHI modifies strain in lattice, resulting in the modifications in transport and magnetotransport properties of manganite thin films. Our main aim behind studying the effect of SHI irradiation on manganite thin films synthesized by CSD route is to improve the temperature coefficient of resistance (TCR), magnetoresistance (MR) & to increase the operating temperature at which manganite thin film can be used as temperature and magnetic sensor. With this background of the earlier studies and our earlier group studies on the effect of SHI irradiation on various properties of PLD grown LPBMO thin films, in this chapter, I have studied the effect of varying 200 MeV Ag^{+15} ion dose on the transport & magnetotransport of CSD grown LPBMO films and compared the results with those reported earlier.

- **Irradiation studies on $La_{0.5}Pr_{0.2}Ba_{0.3}MnO_3$ thin films**

5.1 Synthesis, structure and surface morphological studies

In the first part of chapter, results on effect of 200 MeV Ag ion irradiation on the structural and surface morphological studies of LPBMO thin films grown using CSD technique have been discussed in detail.

5.1.1 Synthesis

To grow LPBMO thin films a low cost CSD technique has been used by following the procedure mentioned below –

The stoichiometric amounts of constituent metal acetates (La-, Pr-, Ba- & Mn-acetates) were dissolved in the mixture of acetic acid and distilled water. This mixture was heated and stirred continuously till a clear solution was obtained which was used for

deposition of films on single crystal $LaAlO_3$ (LAO) *(1 0 0)* substrates using automatic spin coater unit. The parameters of the Spin-coating unit were set at 6000 rpm for 25 s. Films were heated on heating mental at 120 °C for 20 min with possibly lowest heating and cooling rate. Further, the films were heated at 350 °C for 30 min in the furnace. To obtain the thickness of ~ 150 nm the same process was repeated for four times. At the end, deposited films were then annealed in oxygen atmosphere at 1000 °C for 24 hrs.

- **Thin film Deposition parameters**

Target	$La_{0.5}Pr_{0.2}Ba_{0.3}MnO_3$
Substrate	Single crystalline $LaAlO_3$ *(1 0 0)*
Spin coating parameter	6000 rpm for 25 Secs.
Annealing temperature	1000 °C
Annealing time	24 hours
Heating and cooling rate	2°C / min

The LPBMO thin films were irradiated with 200 MeV Ag^{+15} ions with different ion doses ranging from 5 X 10^{10} to 1 X10^{12} using a 15 UD Tandem Accelerator at IUAC, New Delhi. The structure and phase purity of the films were studied using X-ray diffraction (XRD) and the Atomic Force Microscopy (AFM) was used to obtain the information about surface morphology. The resistivity of the films was measured as a function of temperature in the range of 5 – 300 K with applied magnetic field of 0T, 5T and 8T using magnetotransport facilities (Oxford Instruments) available at UGC-DAE CSR, Indore.

5.1.2 Structure

Figure 5.1 (a-d) shows a XRD patterns of 150 nm pristine & irradiated LPBMO thin films grown on single crystal $LaAlO_3$ (LAO) *(h 0 0)* substrates. The patterns reveal that, all the films are *(0 0 l)* oriented on LAO substrate. The values of lattice parameters, calculated from the XRD patterns, vary slightly between 3.904(2) Å to 3.910(2) Å with the change in ion dose from 5 X 10^{10} to 1 X 10^{12} ions/cm^2. Furthermore,

the full width at half maximum (FWHM) of (0 0 1) and (0 0 2) peaks in the LPBMO XRD pattern decreases with increasing ion dose except for the ion dose of 5 X 10^{11} ions/cm^2.

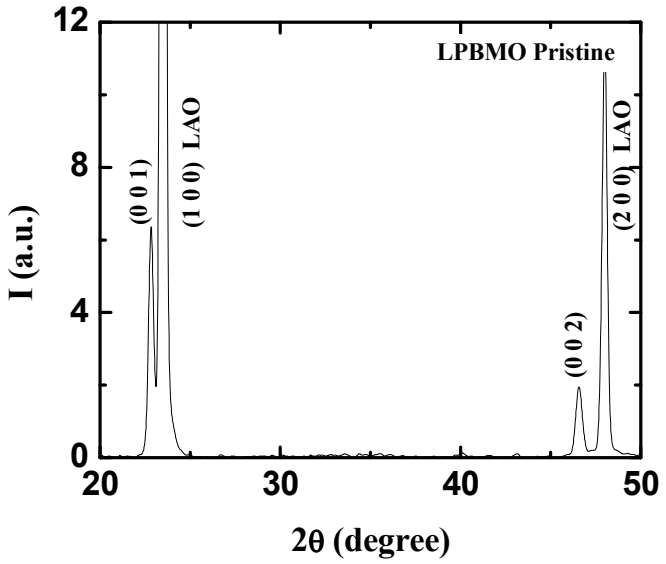

Figure 5.1 a) : XRD pattern of pristine LPBMO thin film.

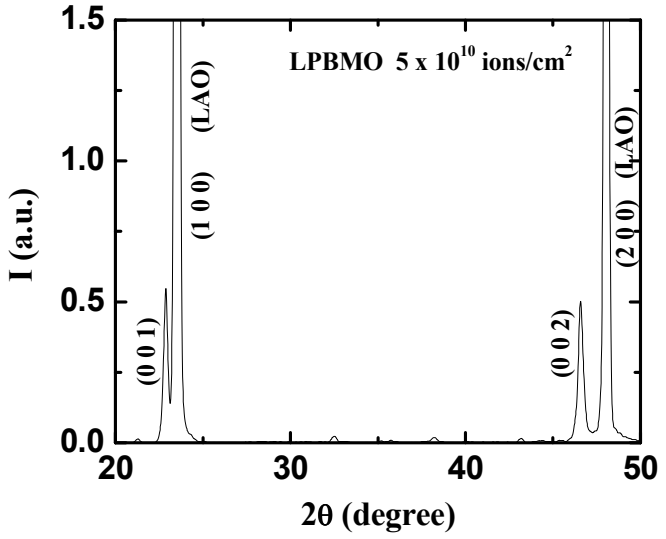

Figure 5.1 b) : XRD pattern of LPBMO thin film irradiated with ion dose of 5 X 10^{10} ions/cm^2.

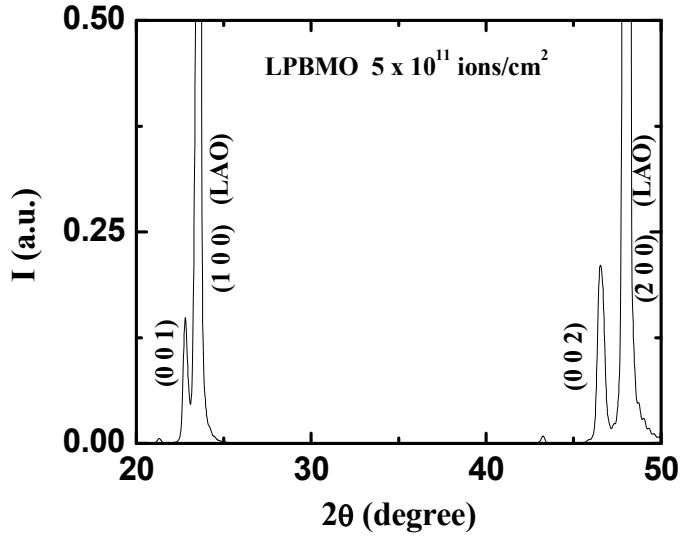

Figure 5.1 c) : XRD pattern of LPBMO thin film irradiated with ion dose of 5 X 10^{11} ions/cm^2.

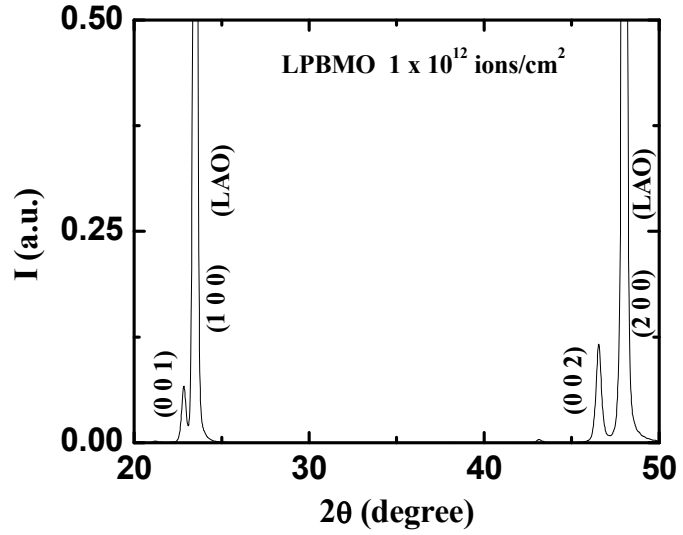

Figure 5.1 d) : XRD pattern of LPBMO thin film irradiated with ion dose of 5 X 10^{12} ions/cm^2.

5.1.3 Surface Morphology

The surface morphology of all the $La_{0.5}Pr_{0.2}Ba_{0.3}MnO_3$ thin films was probed and studied using Atomic Forced Microscopy (AFM). The AFM images obtained are shown in Figs. 5.2 (a-d).

The Fig. 5.2(a) shows the 2D and 3D AFM images and line profile graph of pristine LPBMO film. From the line profile, along the illustrated path, the calculated value of grain size is ~ 200 nm. Figs. 5.2 (b), (c) and (d) shows the 2D AFM images of the LPBMO films irradiated with different ion doses (b) 5 X 10^{10} (c) 5 X 10^{11} (d) 1 X 10^{12} ions/cm^2, respectively. It can be clearly seen from fig. 5.2 (b) that, the film irradiated with 5 X 10^{11} ions/cm^2 exhibit oriented grain structure while the film subjected to higher ion dose (1 X 10^{12} ions/cm^2) shows segregated defect structure of grains [fig. 5.2 (d)].

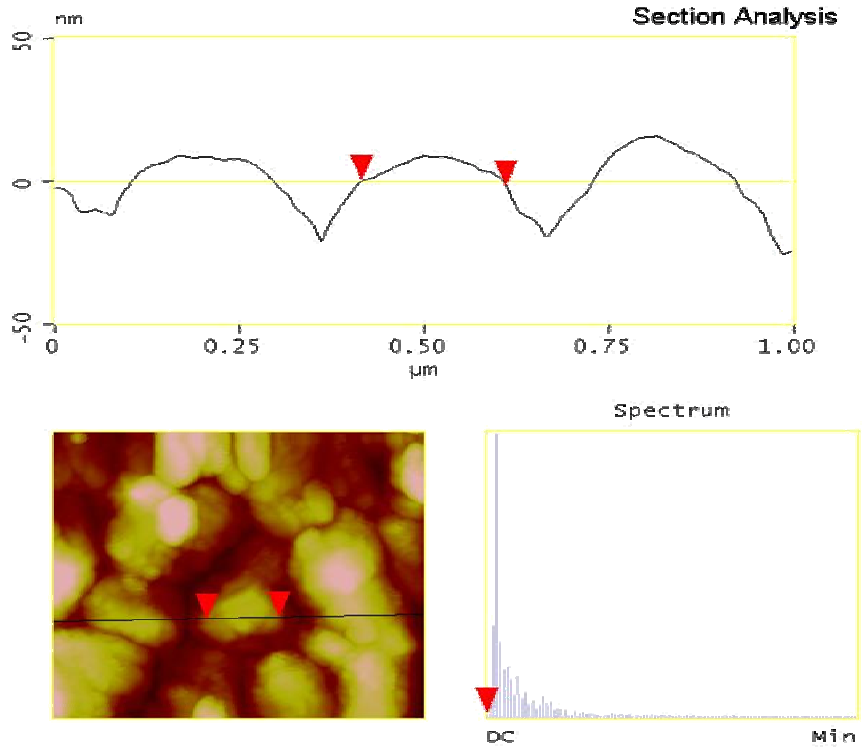

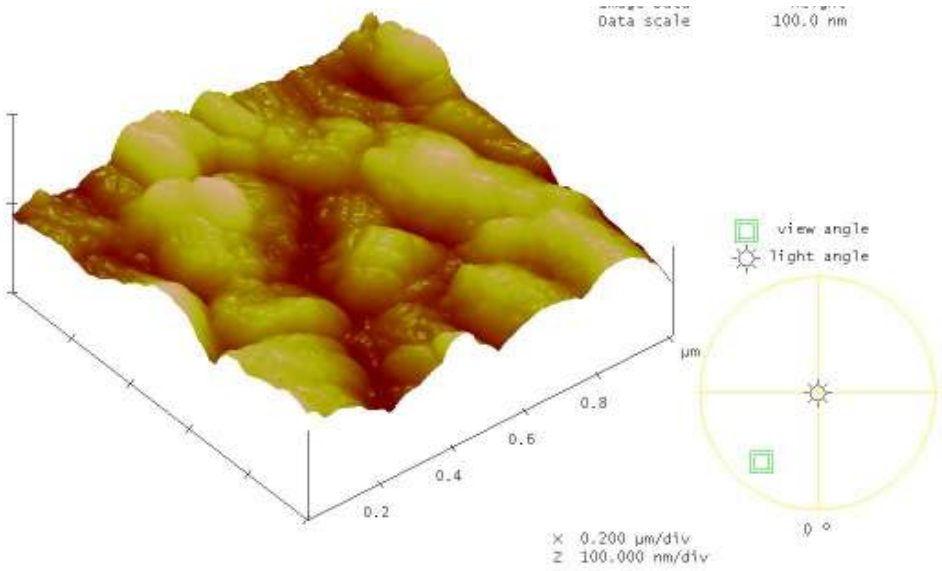

Figure 5.2 (a) : 2D and 3D AFM images along with line profile of pristine LPBMO thin film.

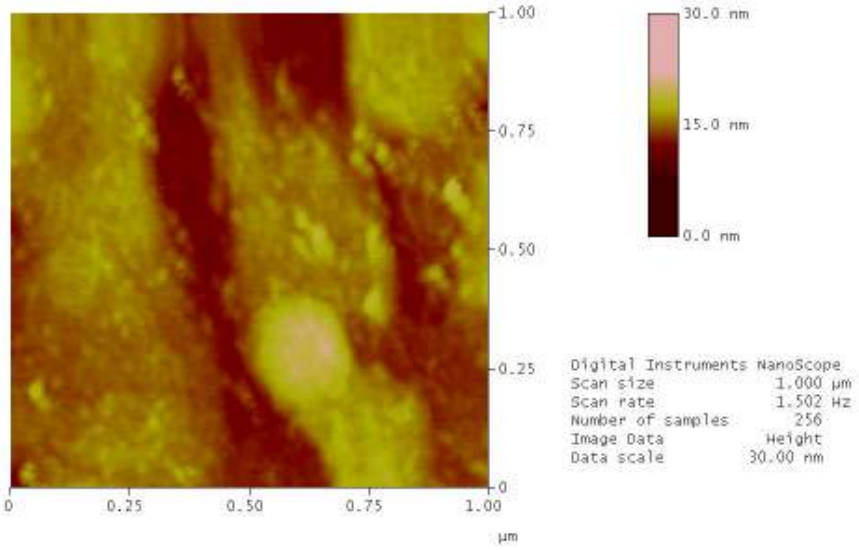

Figure 5.2 (b): 2D AFM image of LPBMO thin film irradiated with ion dose of 5 X 10^{10} ions/cm^2.

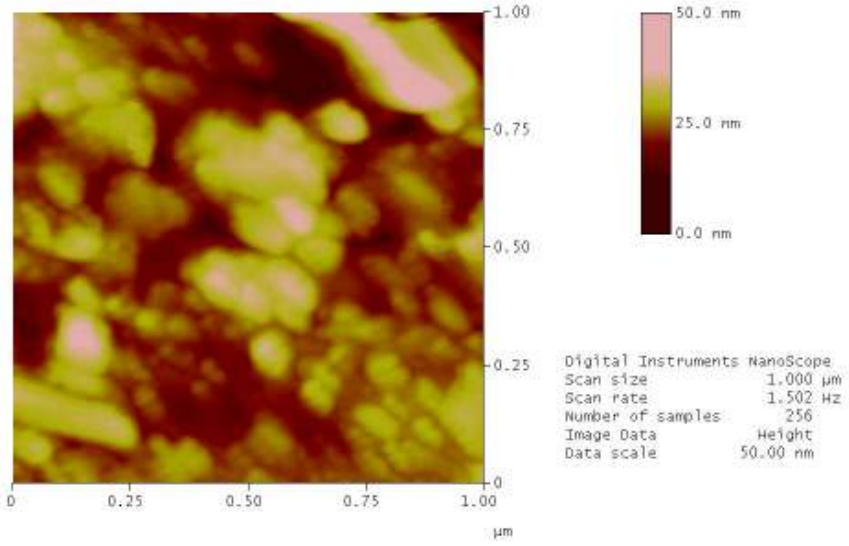

Figure 5.2(c): 2D AFM image of LPBMO thin film irradiated with ion dose of 5 X 10^{11} ions/cm^2.

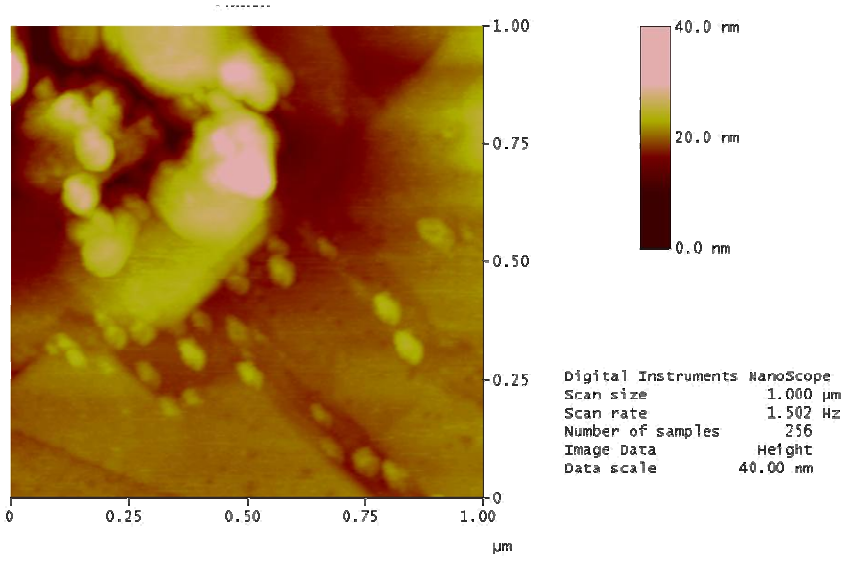

Figure 5.2(d): 2D AFM image of LPBMO thin film irradiated with ion dose of 1 X 10^{12} ions/cm^2.

5. 2 Transport and magnetotransport studies

The transport and magnetotransport measurements, on the LPBMO thin films irradiated with different ion doses, have been carried out using standard d.c. four-probe technique with and without applied magnetic field.

5. 2.1 Resistivity

Figs. 5.3 (a-d) shows the ρ-T plots of the LPBMO thin films (pristine and irradiated) in the temperature range of 5K-300K in 0T, 5T & 8T applied fields.

It can be seen from figs. 5.3 (a-d) that, the pristine and irradiated films show I-M transition at 0T field while under 8T, the transition could not be observed up to RT. Also, there is no effect of magnetic field on the ρ-T behaviour up to 100K in pristine and irradiated films while above 100K, the magnetic field modifies the ρ-T behaviour of pristine & irradiated films in a similar manner. In addition, the peak resistivity of films remains almost same with the increase in field up to 5 X 10^{11} ions/cm^2. Fig. 5.4 depicts the ρ-T plots of pristine & irradiated LPBMO films at 0T showing the suppression in T_P with increasing ion dose except for 5 X 10^{11} ions/cm^2 (Table 5.1). The peak resistivity ρ_p becomes maximum in the film irradiated with 1 X 10^{12} ions/cm^2 dose which can be understood in terms of creation of defects in the film microstructure.

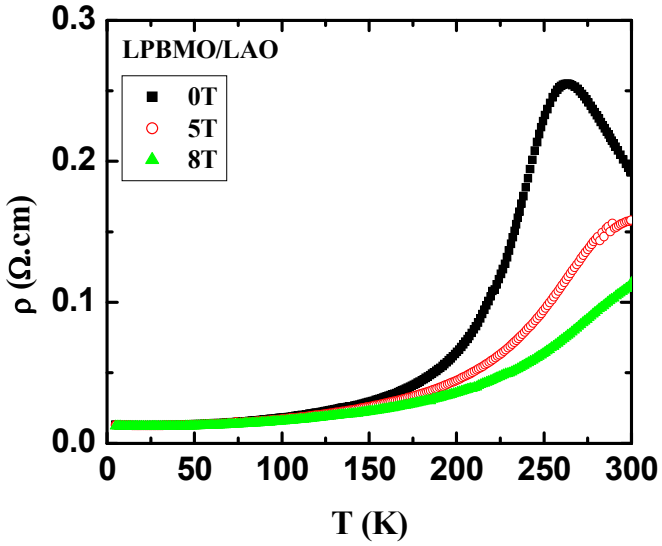

Figure 5.3 (a): Resistivity versus temperature plots for the pristine LPBMO thin film.

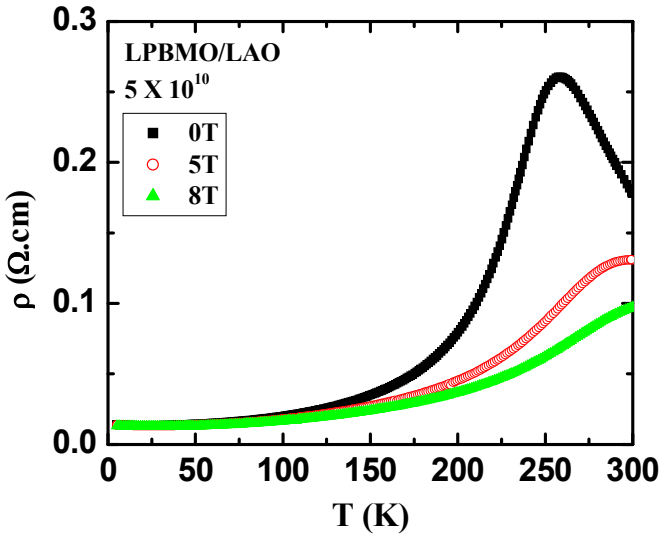

Figure 5.3 (b): Resistivity versus temperature plots for LPBMO thin film irradiated with ion dose of 5 X 10^{10} ions/cm^2.

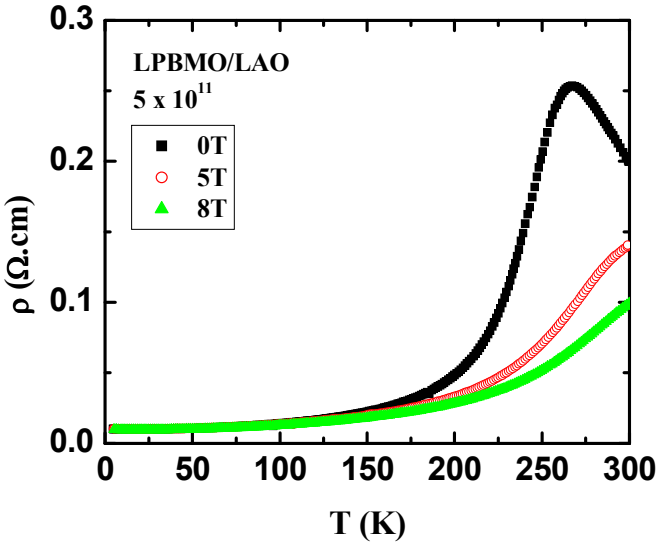

Figure 5.3 (c): Resistivity versus temperature plots for LPBMO thin film irradiated with ion dose of 5 X 10^{11} ions/cm^2.

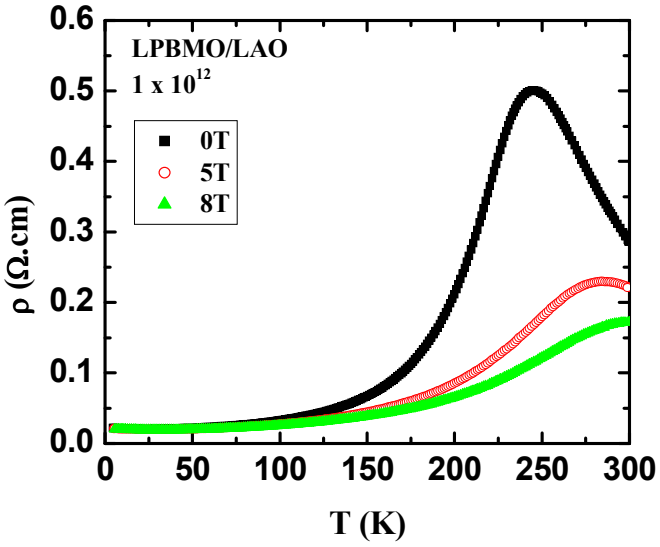

Figure 5.3 (d): Resistivity versus temperature plots for LPBMO thin film irradiated with ion dose of 1 X 10^{12} ions/cm^2.

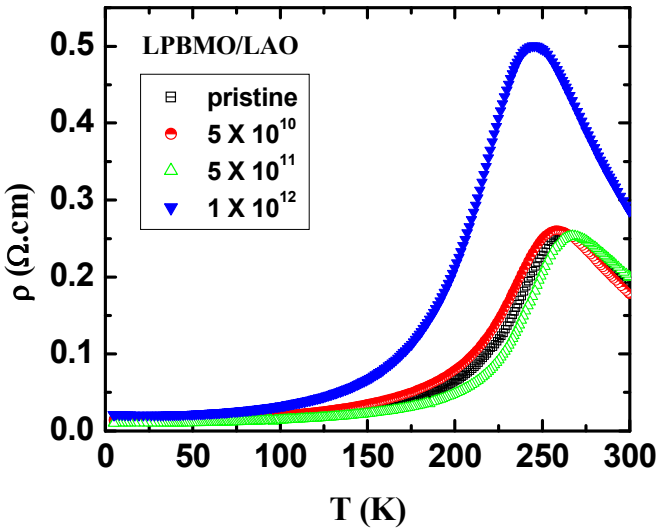

Figure 5.4: Resistivity versus temperature plots for the pristine & films irradiated at 5 X 10^{10} , 5 X 10^{11} , 1 X 10^{12} ions/cm^2 ion dose

Table-5.1: I-M transition temperature (T_p), Peak resistivity (ρ_p) and maximum MR% of pristine and irradiated LPBMO thin films

Irradiation Dose (ions/cm^2)	**T_p (K)**	**ρ_p (Ω.cm)**	**MR_{max}%**
0	263	0.255	72
5 x 10^{10}	259	0.261	75
5 x 10^{11}	267	0.254	76
1 x 10^{12}	246	0.501	78

5.2.2 Magnetoresistance

The magnetoresistance measurements on all the LPBMO films studied, were carried out under various fields up to 8T in the temperature range of 5-300K. Figs. 5.5 (a-d) shows the MR vs H isotherms for pristine and irradiated LPBMO films at various temperatures.

It can be seen from the plots that, the film irradiated with ion dose ~ 1 X 10^{12} ions/cm^2 exhibit maximum MR ~ 78% at 240K while the other irradiated films show a slight variation in MR% values. The MR% ~ 47 at 300K is observed in the pristine LPBMO thin film while MR% ~ 46, 53 and 39 at 300K is exhibited by LPBMO films irradiated with 5 X 10^{10}, 5 X 10^{11} and 1 X 10^{12} ions/cm^2, respectively. Moreover, at low temperature (5K), the maximum MR value exhibited is ~ 3-7% for all the films studied. The observed low MR at low temperature in all the films suggests towards good single crystalline nature of LPBMO films.

Fig. 5.6 & 5.7 shows MR versus temperature plots in an applied field of 8T & 1.2T, respectively. It is interesting to observe that, under 8T, below T_P, increase in ion dose results in an increase in MR while for the ion dose of 5 X 10^{11} ions/cm^2 MR% is lower as compared to other doses. Furthermore, above T_P, increase in the ion dose results in the decrease in MR%, while for the film irradiated with 5 X 10^{11} ions/cm^2, MR% increases as compared to pristine film.

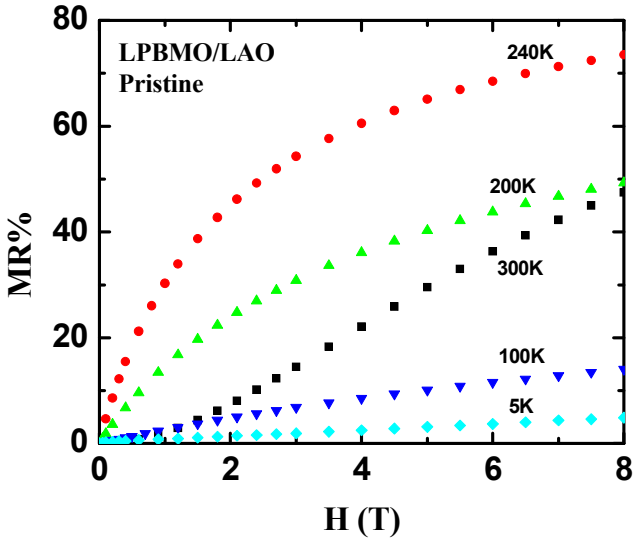

Figure 5.5 (a): MR% as a function of applied magnetic field H for pristine LPBMO thin film sample.

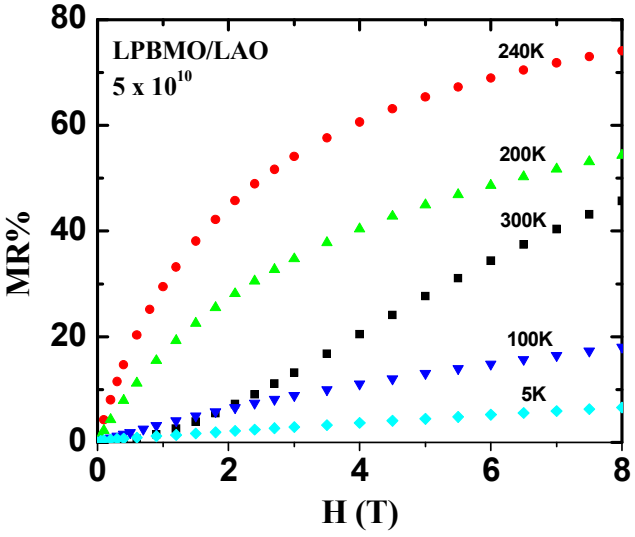

Figure 5.5 (b): MR% as a function of applied magnetic field H for LPBMO thin film sample irradiated with ion dose of 5 X 10^{10} ions/cm^2.

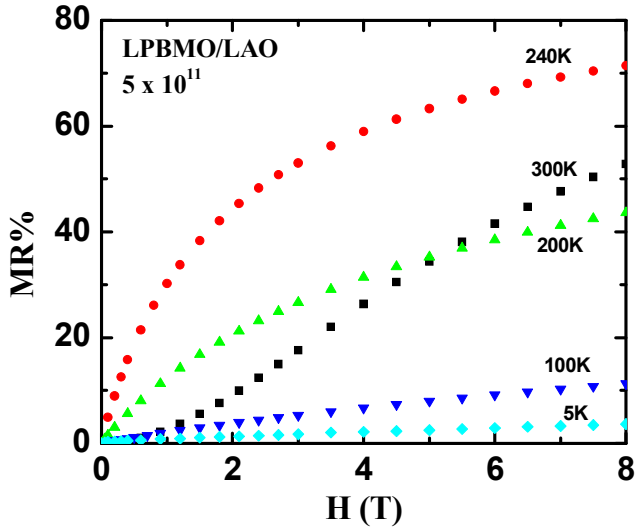

Figure 5.5 (c): MR% as a function of applied magnetic field H for LPBMO thin film sample irradiated with ion dose of 5 X 10^{11} ions/cm^2.

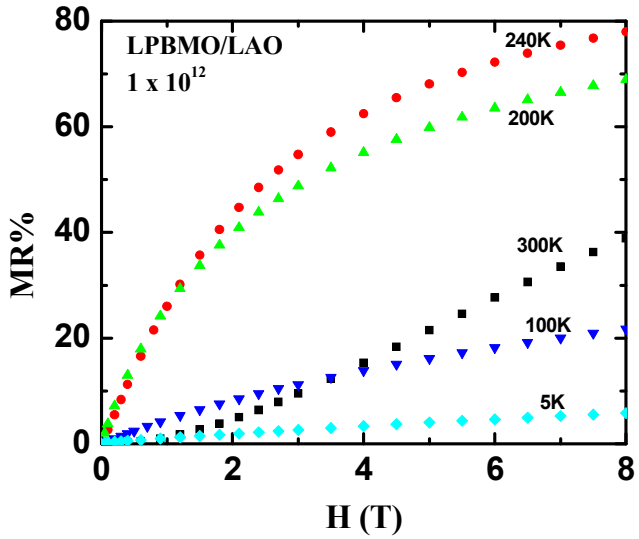

Figure 5.5 (d): MR% as a function of applied magnetic field H for LPBMO thin film sample irradiated with ion dose of 1 X 10^{12} ions/cm^2.

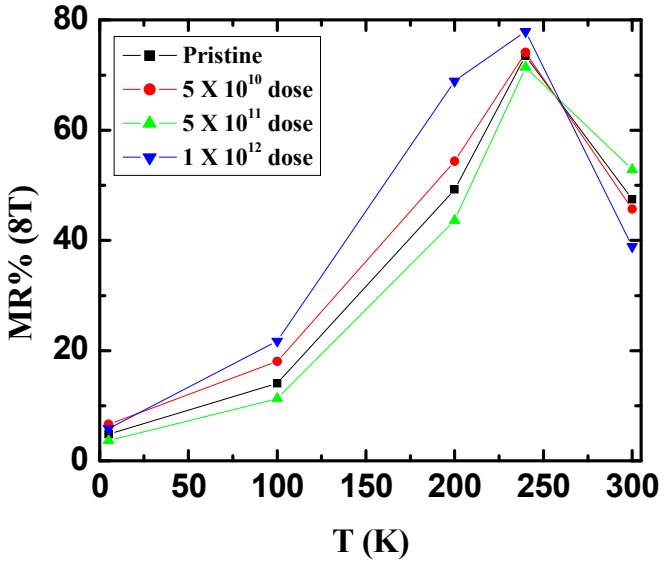

Figure 5.6: MR% as a function of temperature in 8T applied field for pristine & irradiated LPBMO films.

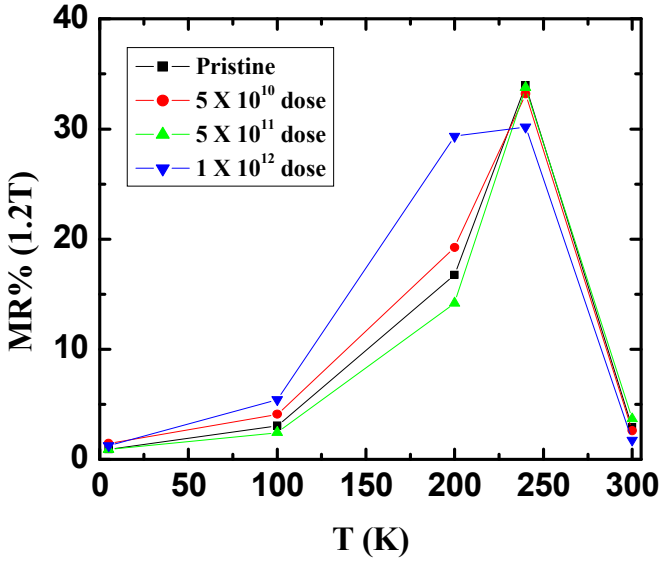

Figure 5.7: MR% as a function of temperature in 1.2T applied field for pristine & irradiated LPBMO films.

5.2.1 TCR and FCR

Figure 5.8 shows TCR% versus temperature plots for the pristine and irradiated LPBMO films.

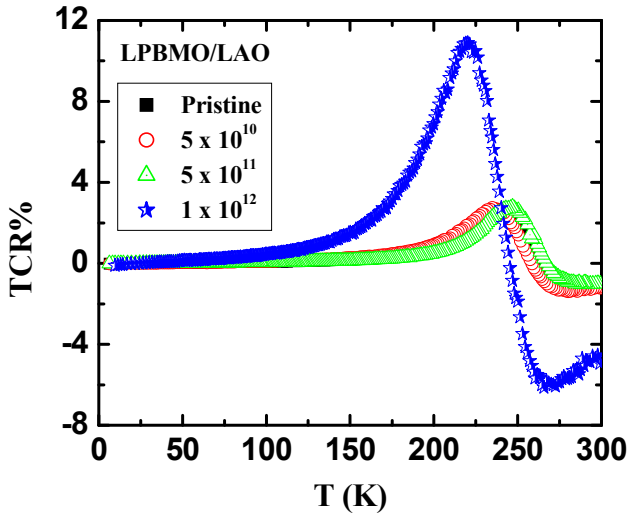

Figure 5.8 : TCR% as a function of temperature for LPBMO thin films.

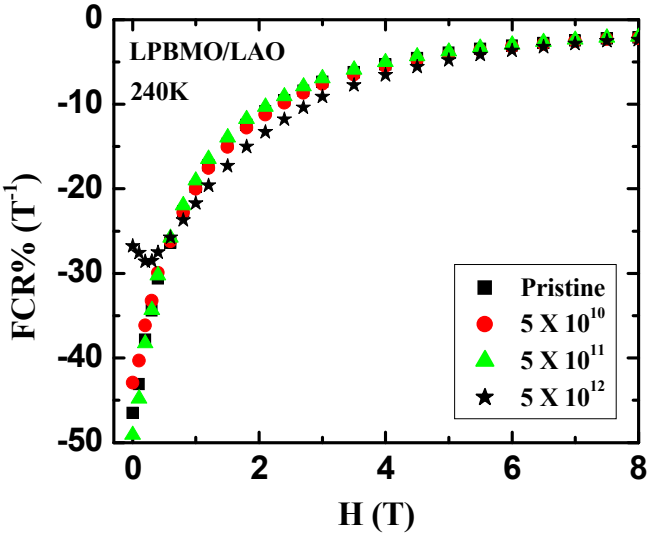

Figure 5.9 : Plots of FCR% vs. H for LPBMO thin films at 240K.

It can be seen from the figure that, the maximum TCR value ~ 3% is exhibited at 241 K for pristine LPBMO film which becomes ~11% at 220 K on irradiating the LPBMO film with a dose ~ 1 X 10^{12} ions/cm^2, TCR ~ 2-3% remains unchanged for other irradiation doses.

Figure 5.9 shows FCR% versus applied field plots for the pristine and irradiated LPBMO films at 240K. It can be seen from the figure that, the maximum FCR value observed is ~ -46% for pristine LPBMO film which becomes ~ -29% on irradiating the LPBMO film with dose ~ 1 X 10^{12} ions/cm^2, whereas for other irradiation doses, FCR varies slightly. The large decrease in FCR% on irradiation with 1 X 10^{12} ions/cm^2, may be due to the creation of irradiation induced defects in the thin film structure.

Discussions

As a result of the above mentioned studies on the effect of SHI irradiation on the properties of CSD grown LPBMO films, the two notable observations are as follows,

The first one is the observation of the enhancement in the T_P for the film irradiated with particular ion dose of 5 x 10^{11} ions/cm^2 and the other is, increase in TCR value in the film irradiated with higher ion dose ~ 1 X 10^{12} ions/cm^2. To understand the cause for the first observation, let us consider the possible reasons for it, which are 1) irradiation induced strain release at the interface [3] 2) pressure developed in lattice due to irradiation which enhances Mn-O-Mn transfer integral resulting in increase in T_P values [14] and 3) defects created in the microstructure due to irradiation resulting in the decrease in crystallinity of thin film [15, 16].

Markna et al had shown that, the local release of strain at the interface affects the transport properties effectively in the manganite films having ultra low thicknesses [3]. In the present case, the film thickness ~ 150 nm suggest that, the strain release effect due to irradiation do not play an important role in modifying T_P behavior. The other two factors, namely the pressure in the lattice developed due to irradiation and the defects created in the microstructure as a result of SHI irradiation are found to affect the T_P behavior in a contradictory manner. One can consider that, pressure developed in the lattice due to ion irradiation, affects the properties of film in the same way, as external or

internal pressure created either hydraulically or chemically, respectively. Fig. 5.10 shows the schematic diagram of effect of pressure and defects created on the T_P of the film. It can be seen that, up to certain irradiation dose, T_P increases after which, reduction in T_P with increasing ion dose is observed (similar to the effect of hydraulic or chemical pressure). Defects created in the microstructure of film, due to irradiation, decreases crystallinity of film and increases non crystalline volume fraction. With increase in ion dose number of defects increases resulting in a linear decrease in T_P. From the above discussion & fig. 5.10, it can be inferred that, for a particular ion dose region the effect of pressure on transport properties of film dominates over the effect of defects created.

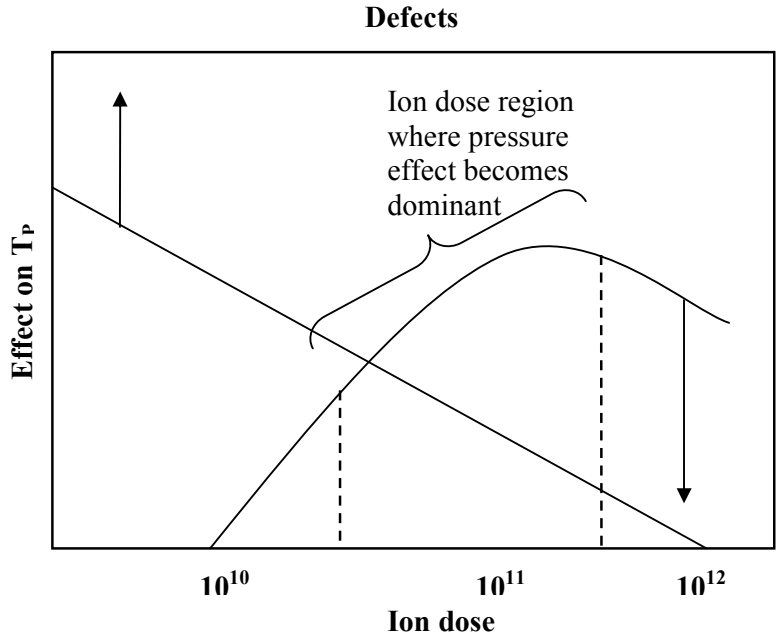

Figure 5.10 : Schematic diagram shows the effect of pressure and defects on manganite thin films

Moreover, the similar effect has been reported for the oxygen and Ag-ions [15, 16]. In the present studies, the observation of ion induced effect on the increase in T_P for particular ion fluence, in the CSD grown LPBMO films, clearly shows that, the effect is irrespective of ion used and the technique of the film synthesis. There is a scope for the further investigations to identify the role and fraction of contribution of affecting parameters on the transport properties of manganite thin films. It will also be helpful in

understanding of ion irradiation induced modifications (improvement in T_P value) in transport properties of manganite thin films.

Ag^{+15} ion irradiation on manganite thin film is known to create defects in the film as well as release of strain at the interface between film and substrate. But, the effect of strain release at interface becomes dominant over the effect of ion-induced defects only when film is uniformly strained (ultrathin film). In the film having large thickness, due to release of strain the effect of defects starts to dominate. The defects are known to provide scattering centers in film which enhances the resistivity and sharpness of transition. As mentioned earlier, the thicknesses of LPBMO films studied were ~ 150 nm and hence the effect of release of strain at the interface can be ignored. But, ion induced defects may be considered as a reason for increase in resistivity and reduction in T_P (Table 5.1). Thus, reduction in the T_P value and an appreciable increase in resistivity and the TCR value of the film is observed for ~ 1 X 10^{12} ions/cm^2 ion fluence. Actually, the SHI with higher fluence (1 X 10^{12} ions/cm^2) apply pressure onto the structure which enhance the structural distortion in the unit cell around their path resulting in the distortion in the ferromagnetic lattice. This distortion behaves as scattering centers in the path of charge carriers which increase resistivity of film as well as TCR but decrease its I-M transition. Thus, it can be said that the ion dose > 1 X 10^{12} ions/cm^2 is responsible for the increase in TCR of the manganite films.

5. 3 Summary and Conclusions

In this part of chapter, the results on the studies on effect of 200 MeV Ag ions irradiation on the LPBMO thin films grown using CSD technique on single crystal LAO *(1 0 0)* substrate have been discussed. XRD pattern shows the epitaxial growth of film in *(0 0 l)* direction on LAO *(1 0 0)* substrate.

AFM studies reveal that, LPBMO thin film exhibits island like growth in pristine film while the irradiation with SHI causes defects in the lattice structure. However, in the case of irradiation dose of 5 X 10^{11} ions/cm^2, oriented grain growth has been clearly observed.

The transport measurements suggest that, pristine LPBMO film shows T_P ~ 263K with ρ_P ~ 0.255 Ω.cm. It is seen that, after irradiation T_P decreases while the ρ_P

increases, except for the irradiation dose 5 X 10^{11} ions/cm^2. In the LPBMO film irradiated with ion dose 5 X 10^{11} ions/cm^2, T_P increases (~ 267K) whereas ρ_P slightly decreases to 0.254 Ω.cm. This has been explained on the basis of the ion induced pressure effect dominating over the effect due to defects created. From the MR measurements, it has been observed that, maximum MR% value increases with increase in irradiation dose while in the metallic region, MR increases with increase in irradiation dose.

The large increase in temperature sensitivity has been observed for an ion dose ~ 1 X 10^{12} ions/cm^2. The maximum TCR value is ~ 3% at 241 K for pristine film which becomes ~11% at 220 K after irradiating LPBMO film with dose 1 X 10^{12} ions/cm^2.

In the pristine LPBMO film, maximum FCR ~ -46% is observed which do not vary much with irradiation dose but for 1 X 10^{12} ions/cm^2, it decrease up to ~ -29% due to irradiation induced defects in the film.

- **$La_{0.66}Lu_{0.04}Sr_{0.3}MnO_3$ bulk and thin films**

5.4 Synthesis, structure and surface morphology studies

In second part of chapter, the results on the studies on substrate dependent modifications in structural, surface morphological, transport and magnetotransport properties of $La_{0.66}Lu_{0.04}Sr_{0.3}MnO_3$ thin films grown using PLD technique have been discussed in detail.

5.4.1 Synthesis

Polycrystalline sample of $La_{0.66}Lu_{0.04}Sr_{0.3}MnO_3$ (LLSM) was synthesized using solid state reaction method. Dried powders of La_2O_3, Lu_2O_3, $SrCO_3$ and MnO_2 were mixed in stoichiometric proportions and calcined at 950°C for 24 hours. The sample was then ground, palletized and sintered in a temperature range of 1100°C - 1400°C with several intermediate grindings. The well characterized sample target (10 mm dia.) was used for the deposition of LLSM films on the single crystalline (l 0 0) oriented $LaAlO_3$ (LAO) and $NdGaO_3$ (NGO) substrates. Third harmonic (355 nm) of a Q-switched Nd-YAG laser was used for the deposition of LLSM thin film on different substrates using PLD technique. The parameters used for the deposition are given in the table below

Table 5.2 : Thin film deposition parameters

Laser used	Nd - YAG
Targets	LLSM Polycrystalline bulk
Substrates	$LaAlO_3$ & $NdGaO_3$ Single crystalline (1 0 0)
Laser energy	~ 2 J/cm^2
Substrate temperature	650 – 700 °C
Substrate to target distance	5.2 cm
Oxygen partial pressure	400 mTorr
Approximated thickness	150 nm

Both LLSM films were annealed in oxygen atmosphere at 1000°C for 24 hours. One more LLSM film was grown on LAO and, all the surface morphological and magnetotransport measurements were carried out on that film without annealing it (hereafter called as "as deposited").

5.4.2 Structure

Figure 5.11 shows the Rietveld fitted XRD pattern of polycrystalline bulk LLSM sample. Rietveld analysis of XRD data reveal that, the LLSM sample is single phasic in nature crystallizing in a distorted orthorhombic structure. The lattice parameters determined from rietveld fitting are; a = 5.458(2) Å, b = 7.755(2) Å and c = 5.507(2) Å.

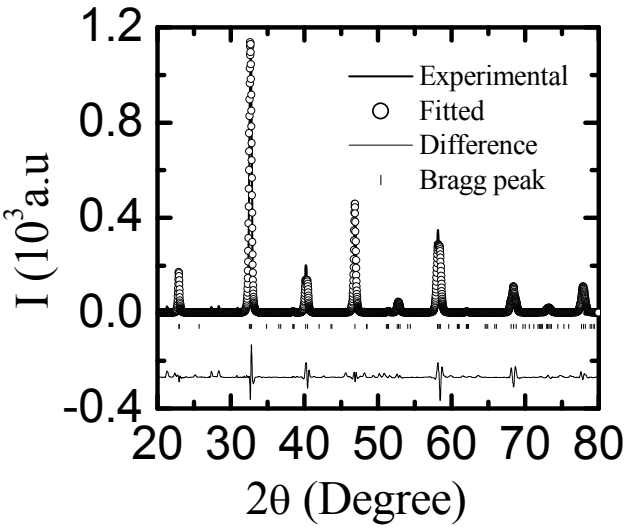

Figure 5.11 : XRD pattern of LLSM polycrystalline bulk sample.

Figs. 5.12 a), b) & c) shows XRD patterns of LLSM film as deposited on LAO, annealed on LAO & on NGO substrates, respectively. All the three XRD patterns were indexed using orthorhombic cell parameters of bulk LLSM sample. From the XRD pattern, it can be seen that, there are no any impurity peaks and the growth of the LLSM film is oriented in *(0 0 l)* direction.

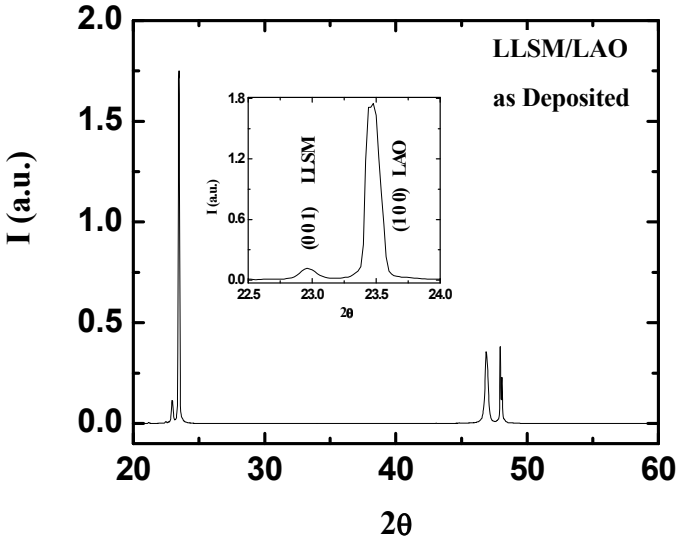

Figure 5.12 a) : XRD pattern of as deposited LLSM thin film on LAO substrate.

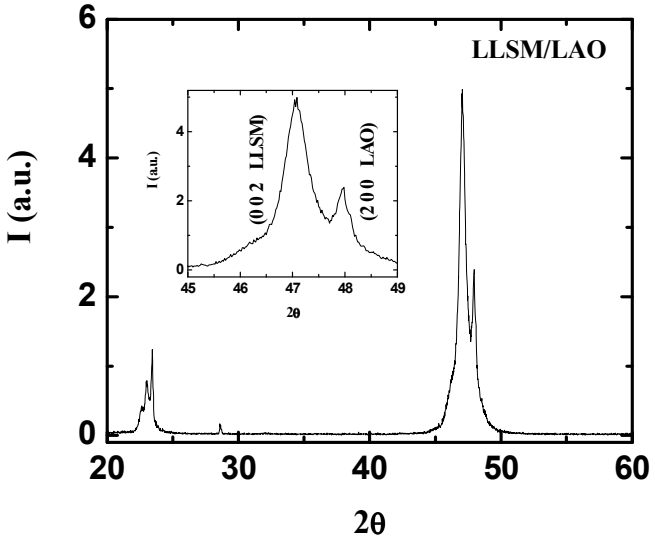

Figure 5.12 b) : XRD pattern of annealed LLSM thin film on LAO substrate.

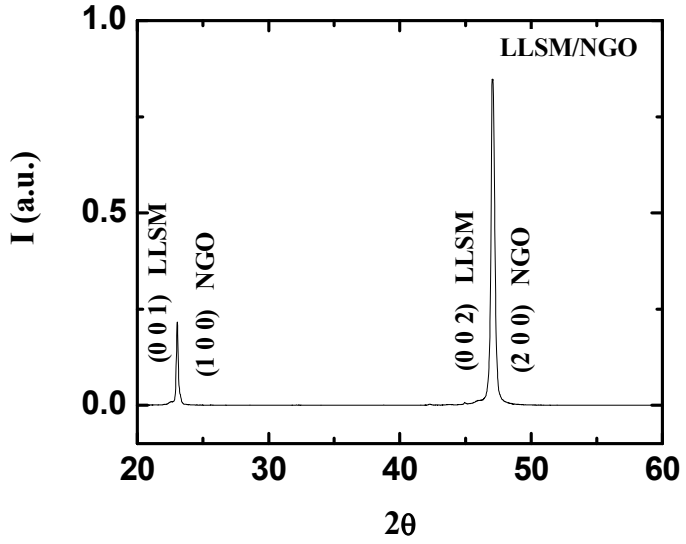

Figure 5.12 c) : XRD pattern of LLSM thin film on NGO substrate.

5.4.3 Surface Morphology

The surface morphology of LLSM films grown on different substrates was probed using the AFM measurements. Fig. 5.13 a) shows the 2D AFM image of as deposited LLSM film on LAO substrate while fig. 5.13 b) shows 3D image of the same. Figs. 5.14 a) & fig. 5.15 a) shows the 2D AFM images of oxygen annealed LLSM films grown on LAO and NGO substrates, respectively while figs. 5.14 b) & fig 5.15 b) depicts 3D images of the same films grown on LAO & NGO substrates, respectively. The average grain sizes calculated using software were ~ 93 and ~ 70 nm for the as deposited and annealed LLSM films on LAO substrates, respectively. The LLSM film grown on NGO substrate possesses ~ 66 nm average grain size. It can be seen that, all LLSM films display island growth in the grain structure and LLSM film grown on LAO substrates exhibit slightly larger grain size as compared to LLSM film on NGO substrate.

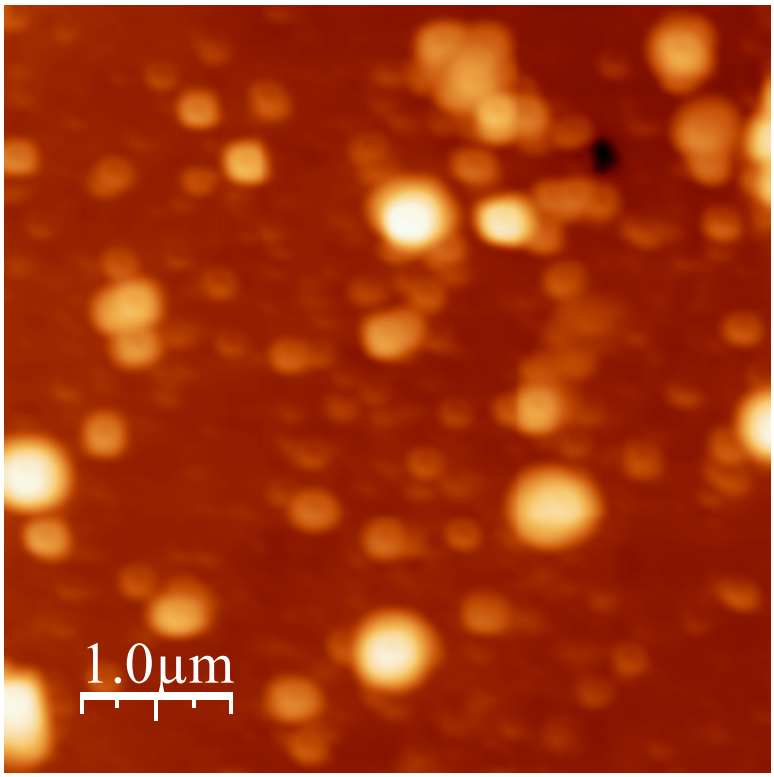

Figure 5.13 a) : 2D AFM image of as deposited LLSM film on LAO substrate.

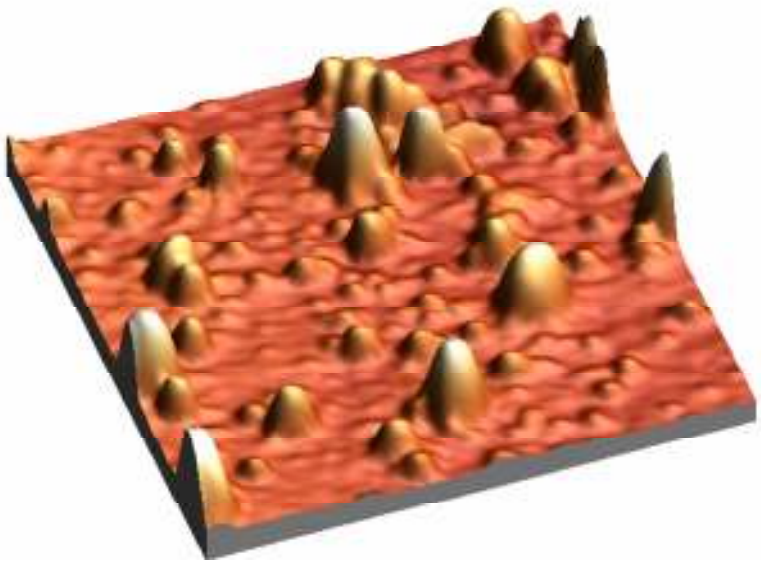

Figure 5.13 b) : 3D AFM image of as deposited LLSM film on LAO substrate.

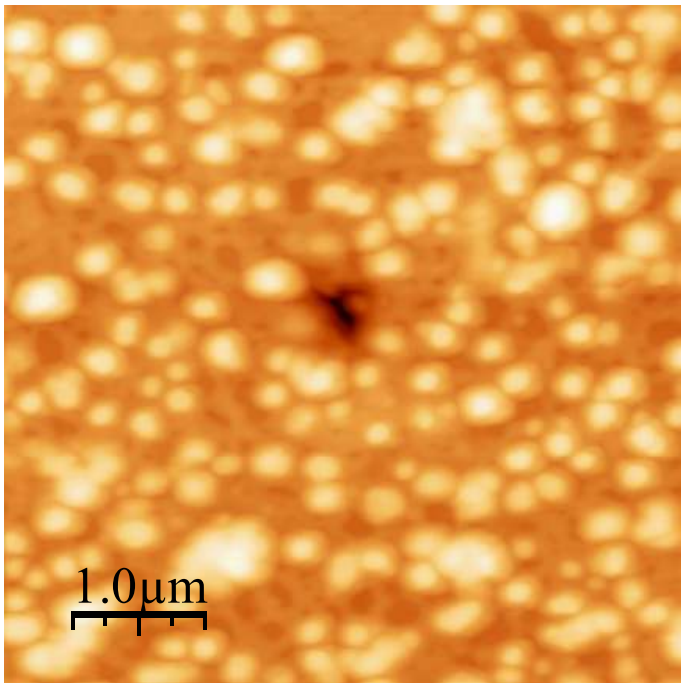

Figure 5.14 a) : 2D AFM image of annealed LLSM film on LAO substrate.

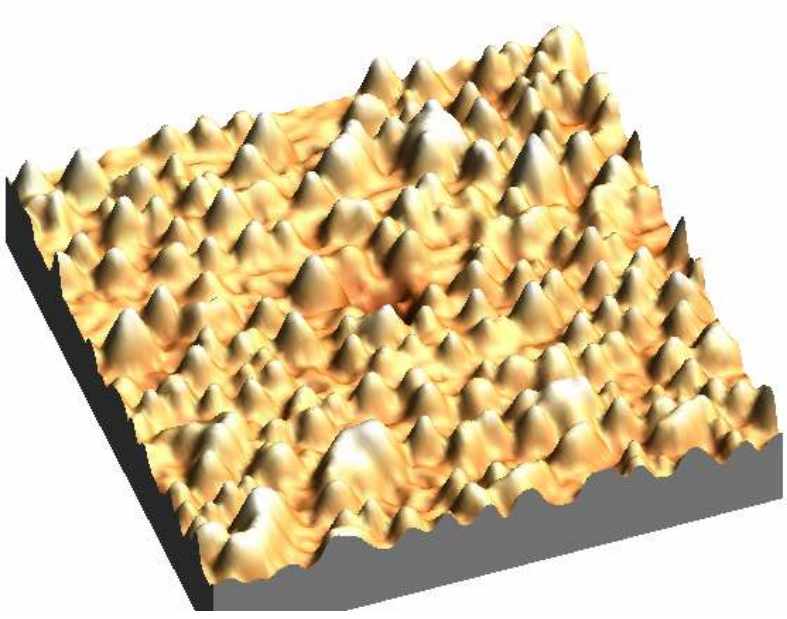

Figure 5.14 b) : 3D AFM image of annealed LLSM film on LAO substrate

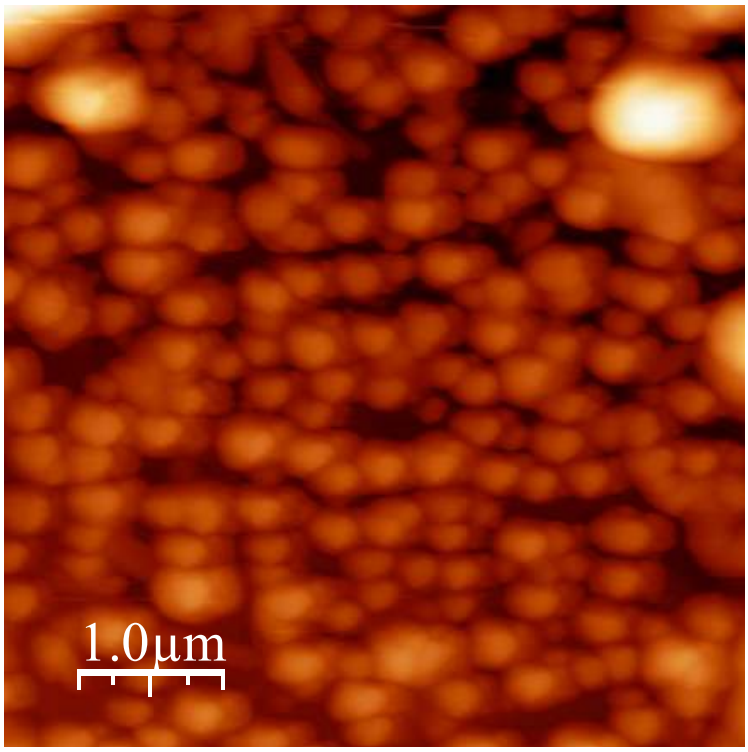

Figure 5.15 a) : 2D AFM image of annealed LLSM film on NGO substrate.

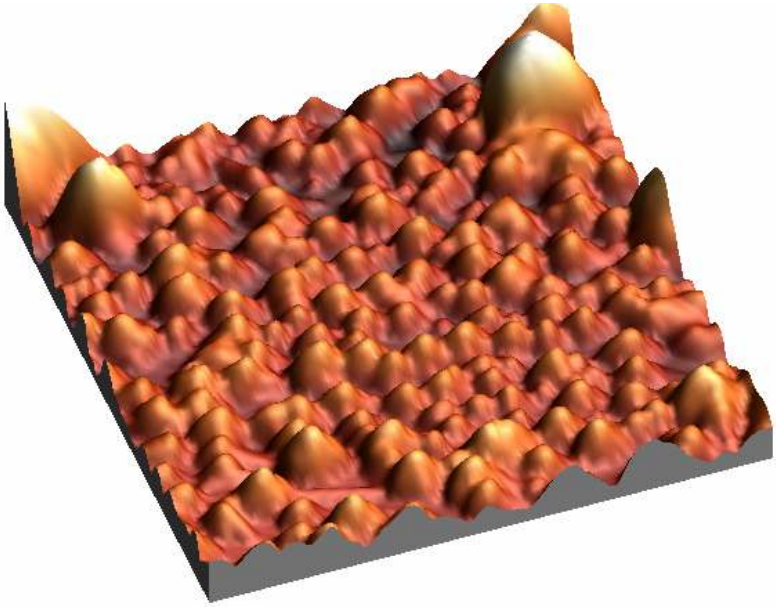

Figure 5.15 b) : 3D AFM image of annealed LLSM film on NGO substrate.

5.5 Transport and magnetotransport studies

The transport and magnetotransport measurements on all LLSM films were carried out using standard d.c. four probe method in the temperature range from 5-300K and magnetic fields up to 8T.

5.5.1 Resistivity

Fig. 5.16 shows the resistance versus temperature plot of bulk LLSM sample. It can be seen that, bulk LLSM sample exhibits I-M transition at ~ 310K.

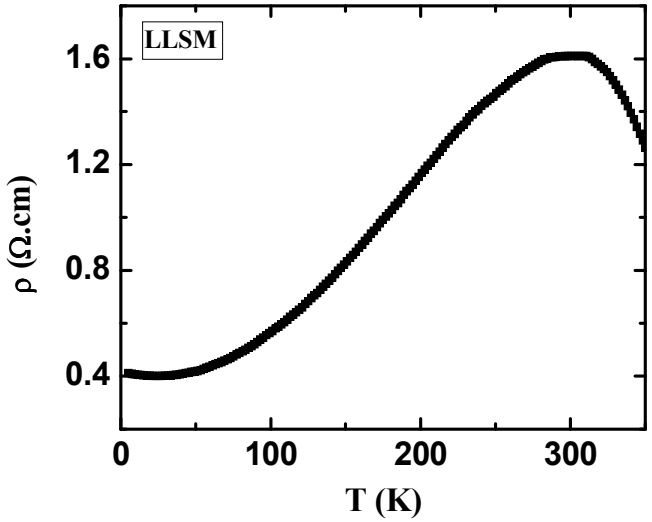

Figure 5.16 : Resistivity versus temperature plot of bulk LLSM sample.

Fig. 5.17 shows the resistance vs. temperature plots of the as deposited LLSM film grown on LAO substrate under different fields. It can be seen from figure that, the resistance of film increases with lowering temperature with and without applied field. The resistance of as deposited film reaches to ~ 2.18 MΩ at 128K with no sign of I-M transition and an exponential increase in the resistance with decrease in temperature. Below 128K, the value of resistance becomes not measurable with the experimental facility available.

The temperature dependence of resistance of LLSM films grown on LAO and NGO is shown in fig. 5.18. It can be seen from figure that, in both case, resistance increases with increase in temperature up to 300K. At 300K, the resistance ~ 0.56 and ~ 0.61KΩ is observed in 0T for LLSM films on LAO & NGO substrates, respectively.

With the application of magnetic field slight drop in resistance is observed for both the films.

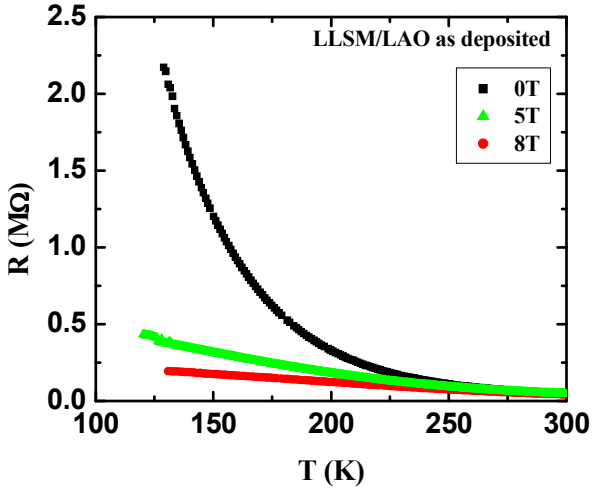

Figure 5.17 : Resistivity versus temperature plot of as deposited LLSM film on LAO substrate.

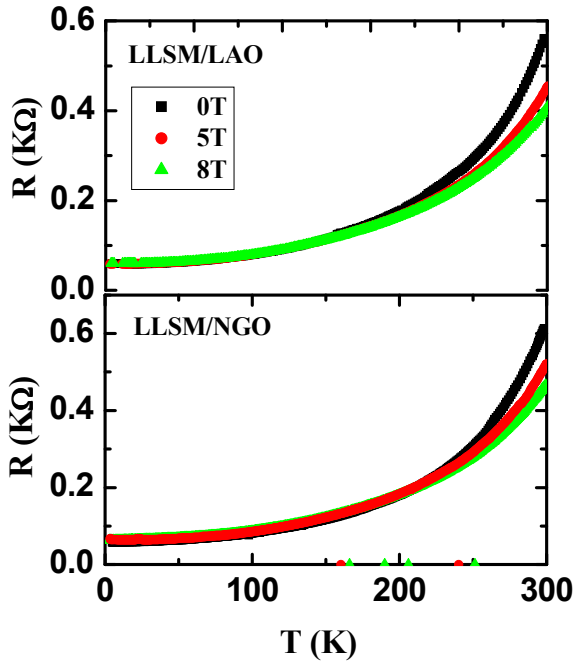

Figure 5.18: Resistivity versus temperature plots of LLSM film on LAO and NGO substrates with applied magnetic fields of 0T, 5T and 8T.

5.5.2 Magnetoresistance (MR)

Fig. 5.19 shows the MR versus H isotherms for the as deposited LLSM film on LAO substrate at 100, 150 & 300K in applied magnetic field up to 8T. It can be seen from the figure that, as deposited LLSM film exhibits large MR ~ -96% and ~-86% at 100K and 150K, respectively. Moreover, such a large MR% in the temperature range of 100-150K becomes ~ -12% at 300K. Fig. 5.20 shows the MR versus H isotherms for the LLSM films on LAO and NGO substrates at 5K, 100K, 150K & 300K with applied fields up to 8T. It can be seen that, near RT the MR% ~-28% and -31% is exhibited by LLSM films on LAO and NGO substrates, respectively while below RT, both LLSM films exhibit MR less than -5%. At 5K, both films exhibit positive MR ~2% and ~9% for the films on LAO & NGO, respectively while at higher temperature, LLSM films exhibit negative MR which converts into positive at low temperature. Such an distinct feature observed in LLSM films at low temperature can be understood in terms of quantum interference effect originating from the disordered-enhanced coulomb interactions which has been discussed in brief in the section 5.3.

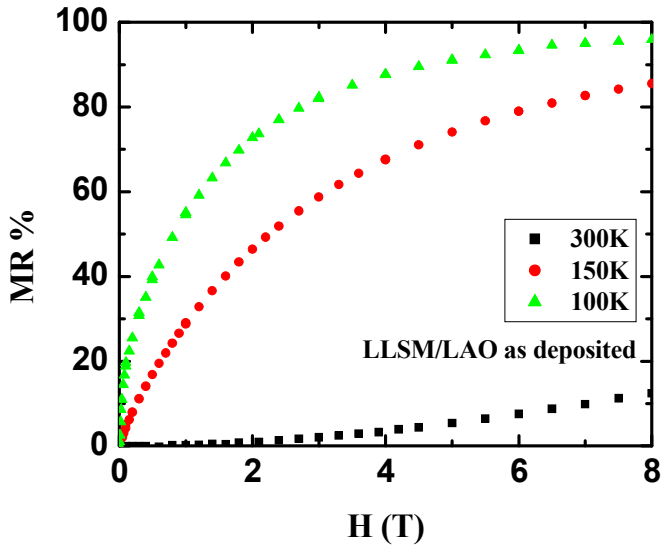

Figure 5.19 : MR vs. H isotherms for as deposited LLSM film on LAO substrate at different temperatures.

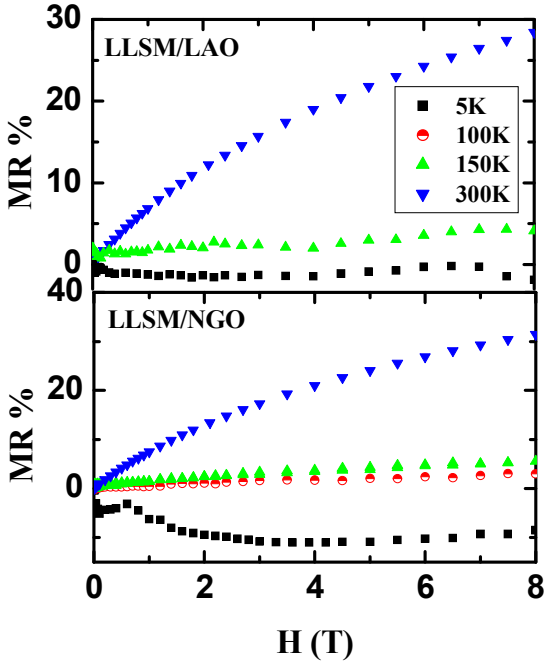

Figure 5.20 : MR vs. H isotherms of LLSM film on LAO and NGO substrates at different temperatures.

5.5.3 TCR and FCR

To explore the application potential of grown LLSM thin films, the temperature sensitivity parameter (TCR) was calculated from resistivity data. Fig. 5.21 show TCR% versus temperature plots for LLSM films on LAO and NGO substrates. The maximum TCR values observed were ~ 1.69% and ~ 1.67% at 300K for LLSM films grown on LAO and NGO substrates, respectively. It can be seen that, both films does not show much difference in its temperature dependent TCR values in complete temperature range studied.

The magnetic field sensing parameter (FCR) has been calculated and plotted as a function of applied field. Fig. 5.22 shows FCR versus H plots for LLSM film on LAO and NGO substrates at 300K. The maximum FCR values observed were ~ -14% and ~ -11% at 300K for the LLSM films on LAO and NGO substrates, respectively. The

LLSM film on LAO exhibit slightly better field sensitivity as compared to film on NGO substrate.

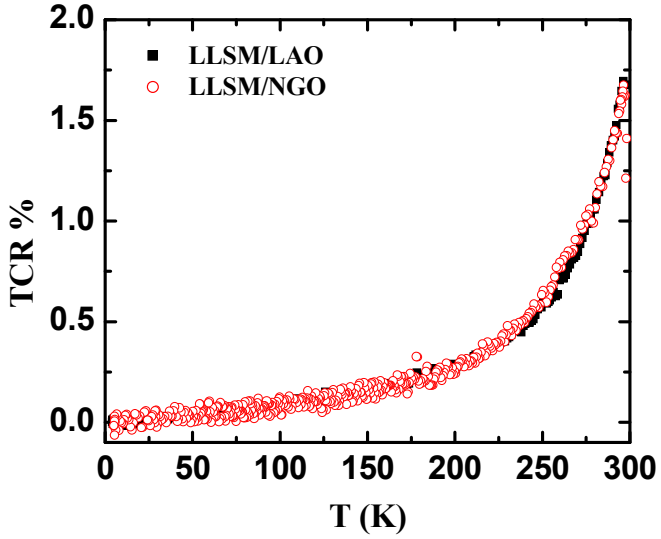

Figure 5.21 : TCR% vs. temperature plots for LLSM film on LAO and NGO substrates.

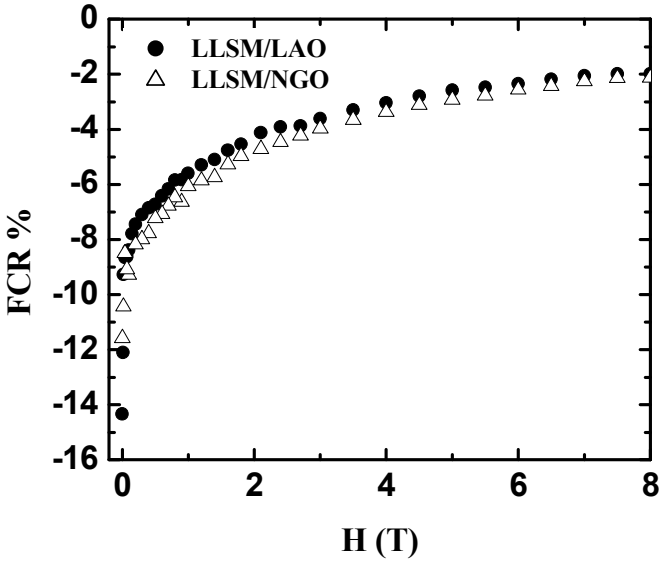

Figure 5.22: FCR% vs. H plots for LLSM film on LAO and NGO substrates at 300K.

5. 6 Summary and Conclusions

In summary, the LLSM films grown on LAO & NGO substrates using PLD are found to exhibit I-M transition ~ 310K. XRD studies shows that film growth was along c-axis orientation, indicating epitaxial growth of LLSM films on LAO and NGO substrates. From the AFM micrographs, it can be observed that, both the films possess island like grain growth in microstructure. However, the average grain size remains almost same in the films on both the substrates (~ 70 nm for LAO & ~ 66 nm for NGO substrate).

As deposited LLSM film on LAO substrate exhibit insulating behavior up to 300K, which on annealing at 1000 °C for 24 hrs exhibit ferromagnetic metallic state. The reason for this may be, as deposited film possess large chemical disorder due to Lu-doping as well as oxygen deficiency which is removed on annealing of films in oxygen atmosphere [17].

An interesting result of the temperature dependent change in the sign of MR observed in LLSM films (on LAO & NGO) can be understood as below –

There are two possible effects of Lu-doping at La-site in LLSM manganites i) the disorder and ii) Phase separation. The Lutetium having smaller ionic radius compared to Lanthanum creates structural disorder in the lattice as well introduces large size disorder at A-site (σ^2 = 0.0036 Å^2) which may result in phase separation. Both the LLSM films grown possess single crystalline nature and hence should exhibit only intrinsic MR near I-M transition temperature and not the extrinsic MR which mainly arises due to grain boundaries. Thus, ideally film should exhibit negative MR near its I-M transition temperature due to suppression of local moment fluctuations due to magnetic field. However, in the present studies, it is seen that, films exhibit positive MR at low temperature. It may be due to Quantum Interference Effect (QIE) arises due to disorder [18]. The competing negative and positive MR results in net MR in LLSM films. Now, at higher temperature, since the contribution of negative MR is more pronounced, the positive MR will be negligible while at low temperature, the negative MR becomes negligible due to the alignment of all local spin moments. Hence, positive MR (resulting due to QIE effect) starts dominating over negative MR.

It is also thought that, the phase separation may be a possible reason for the observed positive MR in LLSM films studied [19]. Further, detailed investigations on these films are needed to clarify these issues.

REFERENCES

1. D.S. Rana, J.H. Markna, R.N. Parmar, P. Raychaudhuri, J. John, S.K. Malik and D.G. Kuberkar, Phys. Rev. B **71**, 212404 (2005).
2. K.R. Mavani, D.S. Rana, J.H. Markna, R.N. Parmar, D.C. Kundaliya, P. Misra, L.M. Kukreja, S.K. Malik and D.G. Kuberkar, J. Appl. Phys. **98**, 086111 (2005).
3. J.H. Markna, R.N. Parmar, D.S. Rana, Ravi Kumar, S.K. Malik and D.G. Kuberkar, Appl. Phys. Lett. **88**, 152503 (2006).
4. S. Jin, T. H. Tiefel, M. McCromack, R. A. Fastnacht, R. Ramesh, and L. H. Chen, Science **264**, 413 (1994).
5. S. Pignard, K. Yu. Zhang, Y. Leprince, Wang K. Han, H. Vincent, J. P. Senateur, Thin Solid Films **391**, 21-27 (2001).
6. Y. Q. Li, J. Zhang, S. Pombrik, S. DiMascio, W. Stevens, Y. F. Yan and N. P. Ong, J. Mater. Res. **10(9)**, 2166 (1995).
7. G. J. Synder , R. Hiskes, S. DiCarolis, M. R. Beasley and T. H. Geballe, Phys. Rev. B **53**, 14434 (1996).
8. U. Hasenkox, C. Mitze and Rainer Waser, J. Am. Ceram. Soc. **80(10)**, 2709 (1997).
9. K. Tanaka, S. Okamura and T. Shiosaki, Jpn. J. Appl. Phys. **40**, 6821 (2001).
10. D.S. Rana, C.M. Thaker, K.R. Mavani, Darshan C. Kundaliya, S.K. Malik and D.G. Kuberkar, J. Appl. Phys. **95**, 4934 (2004).
11. D.S. Rana, M.B. Stone, S.K. Malik, P. Schiffer and D.G. Kuberkar, J. Appl. Phys. **97**, 10H710 (2005).
12. J.F. Ziegler, J.P. Biersack, Program SRIM, 2003, http://www.srim.org.
13. P.G. Radaelli, G. Iannone, M. Marezio, H.Y. Hwang, S.-W. Cheong, J.D. Jorgensen and D.N. Argyriou, Phys. Rev. B **56**, 8265 (1997).
14. H.Y. Hwang, S.-W. Cheong, P.G. Radaelli, M. Marezio and B. Batlogg, Phys. Rev. Lett. **75**, 914 (1995).

15. Ravi Bathe, S.K. Date, S.R. Shinde, L.V. Saraf, S.B. Ogale, S.I. Patil, Ravi Kumar, S.K. Arora and G.K. Mehta, J. Appl. Phys. **83**, 7174 (1998).

16. S.K. Arora, Ravi Kumar, Rajendra Singh, D. Kanjilal, G.K. Mehta, Ravi Bathe, S.I. Patil and S.B. Ogale, J. Appl. Phys. **86**, 4452 (1999).

17. R. Von Helmolt, J. Wecker, B. Holzapfel, L. Schults and K. Samwer, Phys. Rev. Lett. **71**, 2331 (1993).

18. P. Chen, D.Y. Xing and Y.W. Du, Phys. Rev. B **64**, 104402 (2001).

19. N.H. Hong, J. Sakai, J.G. Nouden, F. Gervais and M. Gervais, Phys. Rev. B **67**, 134412 (2004).